Title

Biomaterials for Cell Engineering and Regenerative Medicine

Author

Downing, Timothy

Publication Date

2013

Biomaterials for Cell Engineering and Regenerative Medicine

by

Timothy Lamont Downing

A dissertation submitted in partial satisfaction of the

requirements for the degree of

Joint Doctor of Philosophy
with the University of California, San Francisco

in

Bioengineering

in the

Graduate Division

of the

University of California, Berkeley

Committee in charge:

Professor Song Li, Chair
Professor David V. Schaffer
Professor Tejal A. Desai
Professor Mu-Ming Poo

Fall 2013

Abstract

Biomaterials for Cell Engineering and Regenerative Medicine

by

Timothy Lamont Downing

Joint Doctor of Philosophy
with the University of California, San Francisco

in Bioengineering

University of California, Berkeley

Professor Song Li, Chair

The promise of regenerative medicine relies on the ability to tightly control cell behavior. Given the broad influence of epigenetics in cell behavior and phenotype determination, it is critical to better understand how interactions with the physiological microenvironment and/or implanted materials affect cell's epigenetic state and, thus, identity. In this dissertation we demonstrate, for the first time, that biophysical cues (e.g., matrix topography and stiffness) can significantly improve the efficiency of cell reprogramming, the process of reverting somatic cells back to pluripotency, by inducing key epigenetic changes in adult fibroblasts. To help elucidate the role of biophysical factors in cell reprogramming we have utilized induced pluripotent stem cell (iPSC) technology in conjunction with various bioengineered substrates. These substrates include poly(dimethyl siloxane) (PDMS) microgrooves, aligned nanofibrous membranes, and polyacrylamide hydrogels. Our data largely suggest that cytoskeletal proteins play an important role in the process of cell reprogramming and that manipulation of the biophysical microenvironment can induce dramatic changes in histone acetylation and methylation patterns. These epigenetic changes significantly improve iPSC generation efficiency and replace the effects of potent small molecule epigenetic modifiers valproic acid (VPA) and tranylcypromine (TCP). Furthermore, we identify specific mediators of this epigenetic mechanomodulation, while distinguishing the role of cell shape in the observed histone modifications. This novel biophysical regulation of epigenetics has important implications in cell biology and in the optimization of materials for broad biological application. Finally, this dissertation work describes how drug-eluting microfibrous patches and nanofibrous scaffolds, in conjunction with iPSC-derived stem cells, can be utilized to combine the effects of biophysical guidance cues, therapeutic drug delivery, and cell engineering for the study and repair of spinal cord injury after both traumatic insult and neural tube defect.

Dedication

This work is dedicated to my parents,
Jerry and Katherine Downing,
whose unconditional love and belief in me
is the reason for my accomplishments.

And to my siblings,
Jerry LaCorey, Kristy Joi, and Ryan Vincent,
who set great examples for me to follow.

“For the LORD shall be thy confidence…” – Proverbs 3:26

Acknowledgments

I would, first and foremost, like to thank Jesus Christ, my LORD and savior. Without whom none of this would be possible. The making of this dissertation required the help and support of many people. I would like to thank my family for all of their encouragement, love and support throughout this process. All of my accomplishments are the result of all that they have done for me. I would also like to thank my PhD advisor, Dr. Song Li, who always encouraged me to dream big and gave me great direction and the freedom to explore my intellectual curiosity. I would also like to thank the past and present members of the Song Li Laboratory. All of their inputs helped shape the work of this dissertation. I would like to give a special "thank you" to my colleagues that I have co-authored the work of this dissertation with. Specifically, Drs. Aijun Wang, Yvette Nout, Zhi-Qiang Yan, Payam Saadai, Jose Encinas, Katrine Lofberg, Timothee Houssin, Shyam Patel, Michael S. Beattie, Jacqueline C. Bresnahan, Diana L. Farmer, and David Schaffer. And also Jennifer Soto, Constant Morez, Ashley Fritz, Falei Yuan, Julia Chu, and Andy L. Lee. I also had the opportunity to work with and mentor some incredible undergraduate researchers. These individuals include Elaine Su, Jason Zhong, Zoya Zulfiqar and Thu Tran. This dissertation would not be possible without the outstanding works of all these individuals. I would also like to thank other colleagues that have helped to make my graduate school experience rich and productive. In particular, I would like to thank Drs. Shinya Yamanaka and Masato Nakagawa, at the Center for iPS Cell Research and Application (CiRA) of Kyoto University in Japan, who embraced me into their research institute and laboratory and introduced me to iPS cell technology. Next, I would like to thank the committees that convened to guide my research throughout my PhD career. These committees are 1) my qualifying exam committee (led by Drs. David Schaffer, Mu-ming Poo, Tejal Desai, and Michael S. Beattie) and 2) my dissertation committee (led by Drs. Song Li, David Schaffer, Tejal Desai and Mu-ming Poo). Their guidance and encouragement has made all the difference in my confidence as a scientist. I would also like to thank all of the funding sources that have helped support me during my tenure at the University of California, Berkeley. These funding agencies include the National GEM Consortium, Ford Diversity Foundation, University of California-Berkeley, National Science Foundation East Asia and Pacific Summer Institutes, National Heart Lung and Blood Institute, and the Siebel Scholars Foundation. In addition, the work of this dissertation was funded in part by grants from the Telemedicine & Advanced Technology Research Center (TATRC) (W81XWH0920049 and W81XWH-11-1-0791; to S.L.), in part by grants from the California Institute of Regenerative Medicine (RB3-05232) and the National Institute of Health (EB012240) (also to S.L.), M.S.B., J.C.B., and Y.N, were supported by NIH grants NS031193 and NS038079. The generosity of these organizations was a tremendous asset throughout this process. Finally, there are a number of close friends that have helped make my time in graduate school more enjoyable and also gave me the motivation to strive on to greater things. I would like to mention some of these special individuals by name: Shaun Ossei-Owusu, Krystal Strong, Tierra Bills, Kimberley Kay Hoang, Jennifer Wade, Akwasi Apori, Celeste Chavis Tia Madkins, Lul Tesfai, Jeff Henry, Ray Schmidt, Kyle Kurpinski, Anuj Patel, Ivan Grubisic, Laura Rose Croft, Monica Kapil, Lukasz Bugaj, and Alex Hughes. Your friendships and the memories we share are so greatly appreciated and will never be forgotten.

Table of Contents

Chapter 1: Introduction

Chapter 2: Biomaterials for Regulation of Epigenetic State and Cell Reprogramming

Chapter 3: Drug-Eluting Biomaterials for Spinal Cord Regeneration

Chapter 4: Biomaterials for *In Utero* Repair of Spina Bifida

Chapter 5: Conclusion

References

List of Figures

Chapter 1

Chapter 2

Chapter 3

Chapter 4

Chapter 5

List of Tables

Chapter 2

Chapter 1: Introduction

1.1 Dissertation Introduction

The promise of regenerative medicine relies on our ability to tightly direct cell state. Given this, researchers have employed numerous methods to improve the control of cell behavior both *in vivo* and *in vitro*. These methods include genetic manipulation, biochemical stimulation and presentation, and biophysical regulation. In general, the ultimate focus of these methods is to promote (or prevent) a specific “transition” in cell state (i.e., phenotype and function). While each of these methods represent a significant advance in cell engineering techniques for regenerative medicine, still each of these methods faces its own limitations. In addition, as cells are cultured ex vivo or targeted within their native niche, various chemical and biophysical factors will inevitably be present within the cell’s microenvironment and, thus, have a major influence on cell behavior.

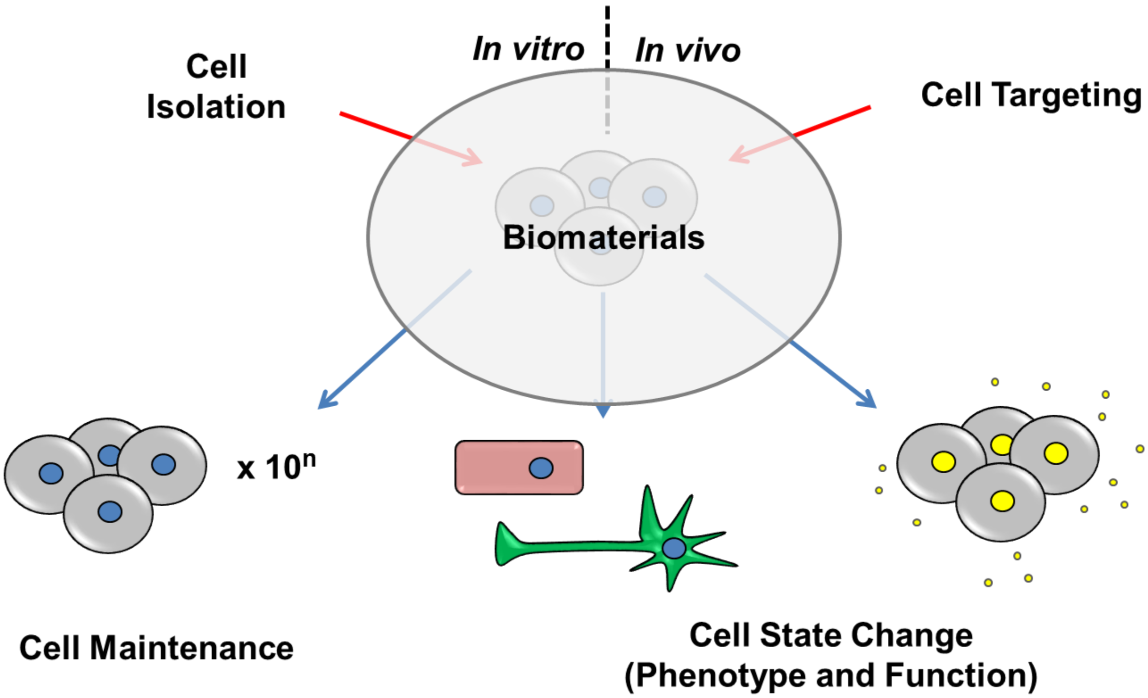

Figure 1.1. Illustration of the influence of biomaterials on cell transitions. This illustration aims to summarize the role that biomaterials have in cell regulations for regenerative medicine

Therefore, in order to gain better control over the cell state, it is important to gain a fundamental understanding of how these environmental cues influence the cell’s intracellular machinery. Even more, it remains of critical importance to better understand how these genetic, chemical, and biophysical cues integrate to impact cell state transitions.

In an effort to provide insight and clarity to this aspect of cell engineering and regenerative medicine, this dissertation explores novel mechanisms of how chemical and biophysical inputs regulate cell behavior. This work has important implications in cell reprogramming and in the optimization of materials for broad biological applications.

1.2 Dissertation Outline

In **Chapter 2**, we explore how biomaterials influence cell fate decisions as it relates to cell reprogramming. In addition, this chapter outlines the epigenetic changes that occur within adult fibroblasts in response to various biophysical inputs and how these epigenetic changes contribute to enhancement in cell reprogramming efficiencies. Even more, these biophysically-induced epigenetic changes replace the effects of potent small molecule epigenetic modifiers. This information is critical to the medical field as it presents new ways to maximize the potential of stem cell technologies, mitigate pathophysiological response in injured and diseased states, and greatly improve the design of next-generation biomaterials.

In **Chapter 3**, we demonstrate how biomaterials in combination with therapeutic agents can help improve spinal cord regeneration after hemisection injury. Importantly, we distinguish the therapeutic outcomes observed from the subdural implantation of patches loaded with low and high doses of small molecule rolipram and trehalose-mediated thermostabilized enzyme chondroitinase ABC (chABC). Patches loaded with lower concentrations yielded significant improvements in functional and anatomical recovery. In all, this work demonstrates the therapeutic utility of drug-eluting microfibrous patches in the study and repair of SCI.

In **Chapter 4**, nanofibrous scaffolds and iPSC-derived stem cells were utilized to combine the potentials of biophysical guidance cues and engineered stem cells for the study and repair of spinal cord injury after neural tube defect, myelomenigocele (MMC) or open spina bifida. In this report we use a sheep model of MMC to demonstrate that biodegradable nanofibrous scaffolds are surgically feasible for repair of open spina bifida. This chapter shows that nanofibrous scaffolds are non-inflammatory in an *in vivo* spinal injury model. We also report, for the first time, the successful engraftment of human stem cells in a fetal model of MMC and describe the derivation of NCSCs from iPSCs and propose a technique for their surgical transplantation in human prenatal MMC repair.

.

Chapter 2: Biomaterials for Regulation of Epigenetic State and Cell Reprogramming

2.1 Introduction

2.1.1 Cell Reprogramming to Pluripotency

Cell reprogramming represents a major advancement in cell biology and has wide applications in regenerative medicine, disease modeling, and drug screening. Induced pluripotent stem cells (iPSCs) can be produced from somatic cells via the forced expression of four or less transcription factors (e.g., Oct4 [O], Sox2 [S], Klf4 [K] or Nanog, and c-Myc [M] or Lin28)[1–4]. Recently, the overexpression of epithelial-cadherin (E-cad) was shown to replace the need for Oct4 –the most critical factor of the OSKM cocktail –during cell reprogramming[5]. In addition, the elimination of E-cad in somatic cells prevents nuclear reprogramming to pluripotency all together[6]. These results corroborate the importance of the reported mesenchymal-to-epithelial transition (MET) that occurs during the reprogramming process[7].

2.1.2 Epigenetic Regulation and Cell State

Since the first report on iPSC generation, researchers have employed numerous methods to improve reprogramming efficiency. Chemical compounds, in particular, have shown great promise in enhancing the efficiency of iPSC formation and/or eliminating the need for some oncogenic transcription factors such as c-Myc and Klf4[8–12]. For example, valproic acid (VPA), a histone deacetylase (HDAC) inhibitor, was reported to increase the percentage of Oct4+ cells generated during reprogramming[11]. Tranylcypromine hydrochloride (TCP), an inhibitor of lysine-specific demethylase, was also shown to significantly improve reprogramming efficiency[9]. Researchers have more recently demonstrated the ability of VPA to promote transcription factor-free reprogramming through the overexpression of microRNAs (miRNAs), specifically the miR302/367 cluster, in mouse fibroblasts[13]. Interestingly, this miRNA-mediated reprogramming was shown to be dependent on VPA-induced degradation of HDAC2, suggesting that HDAC proteins act as inhibitors of cell reprogramming. These studies, along with many others[14–16], highlight the critical role of histone modifications and epigenetic state in cell reprogramming.

2.1.3 Cell-Adhesive Substrates for Regulation of Cell State

Although extensive studies have been performed on the roles of transcription factors, miRNAs, and chemical compounds in cell reprogramming, the role of biophysical cues in this process has yet to be revealed. Biophysical factors (i.e., the topographical and mechanical properties of cell-adhesive materials) have been shown to regulate a variety of cellular functions such as migration, proliferation, and differentiation[17–29]. Importantly, these functions have closely-related influences in a broad range of complex biological processes such as wound healing, tissue remodeling, and tumor growth. There is also growing evidence that biophysical signals can be transmitted through the cytoskeleton, and into the nucleus and chromatin[30,31].

2.1.4 Role of Mechanobiology in Pluripotent Stem Cell Maintenance

In addition, while some studies have demonstrated that substrate properties can help regulate adult stem cell self-renewal[32,33], an increasing number of laboratories have investigated the role of mechanotransduction in the maintenance of embryonic stem cells (ESCs)[6,20,34–36]. These studies highlight the importance of biomechanics in the regulation of pluripotency. For example, an intact actin-myosin network is critical for the stable propagation of human ESCs. Nonmuscle myosin IIA (NNMIIA), specifically, was found to play a critical role in ESC maintenance as its inhibition, via shRNA knockdown or treatment with blebbistatin, downregulates the expression of E-cad, a transmembrane “mechanosensor,” leading to a deregulation of the pluripotency circuitry. Still, however, it is not known whether or how the biophysical properties of cell-adhesive materials influence adult cell reprogramming, a reverse process of cell differentiation. In addition, whether mechanotransduction can induce critical epigenetic modifications in somatic cells, which might facilitate the reprogramming process, also remains unclear.

To elucidate the role of biophysical factors in cell reprogramming, we have utilized reprogramming technology in conjunction with various bioengineered substrates. Our data show that the biophysical microenvironment, in the form of micro- and nano-scale topography on cell-adhesive substrates, can induce dramatic changes in histone acetylation and methylation patterns, which are dependent on cell morphological changes and actin-myosin tension. These epigenetic changes can replace the effects of potent small molecule epigenetic modifiers and significantly improve iPSC generation efficiency. Furthermore, we identify specific mediators of this epigenetic mechanomodulation. Our findings represent a significant advancement in the understanding of mechanotransduction by revealing a novel relationship between the biophysical microenvironment, epigenetic mechanomodulation, and cell reprogramming.

2.2 Materials and Methods

2.2.1 Fabrication and Preparation of Cell Adhesive Substrates

Microgroove, nanofiber, micropatterned, 2D polyacrylamide substrate fabrication.

Bioengineered substrates were fabricated as previously described[23,37–39]. Briefly, PDMS membranes were fabricated using well established soft lithography procedures. Poly-L-Lactic Acid (PLLA) or poly(L-lactide-co-caprolactone) nanofibers were fabricated using electrospinning technology where random fibers were ejected onto a grounded collector. Aligned fibers were produced by collector modifications or mechanical stretch. Micropatterned islands on PDMS substrates were fabricated using oxygen plasma treatment through the windows of a PDMS membrane mask that produced hydrophilic areas of different shapes and sizes. All substrates were coated with 2% gelatin for 1 hour to promote cell attachment. 2D polyacrylamide (PA) hydrogel substrates of various rigidities were fabricated using variable monomer (acrylamide) to cross-linker (N,N'-methylenebisacrylamide) ratios. Expected rigidity values based on these ratios are well characterized in the literature. These values were also confirmed in our laboratory via atomic force microscopy. PA gel rigidity ranged from 0.6 to 40 kPa. To enhance cell attachment, the surface of PA gels were functionalized with type-I collagen as described elsewhere. Collagen coated glass slides were used as controls.

2.2.2 Fibroblast Isolation, Culture, and Reprogramming

Fibroblast isolation, culture, and reprogramming.

Ear tissues from adult C57BL/6 mice were minced and then partially digested in a solution of 3 mg/ml collagenase type IV (Invitrogen) and 0.25% trypsin-EDTA (GIBCO) for 30 minutes under constant agitation at 37°C. Partially digested tissues were plated and fibroblasts were allowed to migrate out (passage 0). Isolated fibroblasts were expanded in MEF medium (DMEM [Hyclone] +10%FBS [Hyclone] and 1% penicillin/streptomycin [GIBCO]) and used exclusively at passage 2 for all experiments. Fibroblasts from Oct4-GFP reporter mice (008214; The Jackson Laboratory) were also isolated as described above. Normal neonatal human dermal fibroblasts (NHDF) were purchased from Lonza (CC-2509) and expanded in FGM™-2 BulletKit™ (CC-3132) for 1-2 passages. After transduction, mouse fibroblasts were seeded onto PDMS membranes with flat and microgroove topographies or nanofibers of aligned and random orientation. After seeding, transduced fibroblasts were maintained in MEF medium for forty-eight hours. For the next 10 to 12 days, cells were fed with mouse mESC medium (DMEM + 15% mouse ESC maintenance FBS [STEMCELL Technologies], 100 units/ml ESGRO® mouse Leukemia Inhibitory Factor (mLIF) [Millipore], 0.1 mM β-Mercaptoethanol [Sigma], and 1x MEM Non-Essental Amino Acid [GIBCO]). Reprogrammed NHDF were cultured in mTeSR™1 complete medium from STEMCELL Technologies. Human iPSCs were reprogrammed for

1 month after the infection with OSKM before colonies were expanded and/or analyzed. Culture medium was replenished every 1 to 2 days during reprogramming. VPA (0.5 mM) (Sigma) and TCP (5 µM) (Sigma) were used for biochemical modulation of epigenetics. Cells were exposed to TGF-β1 (2 ng/ml) for 5 days for activation of the TGF-β pathway. A-83-01 (0.5 µM) (Millipore) was used for all 14 days during the reprogramming. Blebbistatin (10 µM) (or DMSO) was administered for 3 days.

Lentiviral production and cell transduction.

Lentiviral vectors were used to transduce mouse fibroblasts for ectopic expression of three (OSK) or four (OSKM) of the key reprogramming genes or microRNAs (miR302/367cluster). STEMCCA-loxP and STEMCCA-loxP-RedLight plasmids were a generous gift from Dr. Gustavo Mostoslavsky at Boston University. Lentivirus was produced using common, well-established calcium phosphate transfection methods. Viral particles were collected and concentrated using Lenti-X Concentrator (Clontech) according to the manufacturer's protocol. Stable virus was aliquoted and stored at -80°C. For viral transduction, fibroblasts were seeded and allowed to attach overnight. Cells were then incubated with virus for 24 hours. After incubation, transduced cells were reseeded onto either PDMS or nanofiber surfaces.

2.2.3 Pluripotent Stem Cell Characterization and Colony Quantification

Immunostaining, imaging and quantifications, teratoma formation, in vitro differentiation.

For immunostaining, cells were fixed with 4% PFA, permeabilized with 0.5% Triton-100 (Sigma), and blocked with 1% BSA (Sigma). For actin-cytoskeleton staining, samples were incubated with fluorescein isothiocyanate-conjugated phalloidin (Invitrogen) for 2 hours. Primary antibodies were incubated overnight at 4°C, followed by 1-hour incubation with Alexa 488 and/or Alexa 546 -labeled secondary antibodies (Molecular Probes). Nuclei were stained with 4,6-diamino-2-phenylindole (DAPI) (Invitrogen).

For counting iPSC colonies, entire wells were imaged using an ImageXpress® Micro System (Molecular Devices). Colonies were determined positive for Nanog protein expression based on positive (mESCs) and negative (uninfected/non-reprogrammed mouse fibroblasts) thresholds. Confocal and epifluorescence images were collected using a Zeiss LSM710 microscope and Zeiss Axio Observer.A1, respectively. DAPI images were used to determine nuclear shape index. For quantification of AcH3, H3k4me2, and H3k4me3 fluorescence intensity, 40x epifluorescence images were used. DAPI staining was used as a mask and fluorescence intensity was averaged over the entire nucleus. All image analyses were performed using a Matlab script or ImageJ software.

Teratoma formation was performed by injecting 1 x 106 cells into the abdominal cavity of SCID/NOD mice. After 1 month mice were sacrificed, the formed teratomas were explanted and fixed using paraffin-embedding and sectioned using a microtome. H&E staining was performed for histological analysis.

Embryoid body (EB) formation for in vitro differentiation was performed using the hanging-drop method. Mouse iPSCs were cultured in mESC maintenance media without LIF. EBs were plated onto gelatin coated surfaces and allowed to spontaneously differentiate. After 2 weeks of differentiation, samples were fixed and immunostained. Human iPSCs were overgrown in a feeder-free system using mTeSR™1 complete medium to initiate spontaneous differentiation.

2.2.4 Biochemical Analysis of Epigenetic State and Gene Expression

ChIP-qPCR and qRT-PCR.

ChIP-qPCR was performed by using a high-throughput ChIP kit (EZ-Magna ChIPTM HT96; Millipore), according to the manufacturer's instructions. Sonicated chromatin prepared from 100,000 mouse fibroblasts was subjected to ChIP by using 3 µg of normal rabbit IgG (CS200581; Millipore) or specific antibodies for AcH3 (06-599; Millipore), H3k4me2 (05-1338; Millipore) or H3k4me3 (07-473, Millipore). Substantial fold enrichment was observed for each experimental condition (Figure 2.1). ChIP-qPCR data were analyzed by normalizing DNA concentration to percent input using a relative standard curve method. Primers for ChIP-qPCR are included as supplemental information (Table 2.1). Quantitative RT-PCR (qRT-PCR) was performed using a customized StellARayTM Gene Expression System (Lonza) to probe for multiple genes at once. RNA was isolated using a NucleoSpin® RNA II kit from Clontech and converted to cDNA using RT2 First Strand Kit (Qiagen). qRT-PCR data were analyzed using ΔΔCt method.

RNA interference.

RNA interference was performed using control (Cat. No. 4390853) and WDR5 (Cat. No. 4390771, ID: s100547, Lot: ASO0R7LI) Silencer® Select siRNAs from Ambion®. Transfections were carried out using Lipofectamine® RNAiMAX Reagent (Invitrogen) according to manufacturer's instructions.

Western blotting analysis.

Fibroblasts were lysed and collected in a buffer containing 20 mM Tris-HCl, 150 mM NaCl, 1% Triton-X-100, 0.1% SDS, 10 mM NaF along with protease inhibitors (PMSF, Na3VO4 and Leupeptin). Protein lysates were centrifuged to pellet cell debris, and the supernatant was removed and quantified by DC Protein Assay (Bio-Rad). Protein samples (15 mg per well) were run using SDS-PAGE and transferred to polyvinylidene fluoride (PVDF) membranes. Membranes were blocked in 3% nonfat milk and incubated with primary antibodies. Primary antibodies include AcH3, H3k4me3, HDAC 1, 2, 3, WDR5, H3, Actin, and GAPDH. Refer to Table 2.2 for all antibody information. All antibodies were used at a 1:1000 dilution and incubated overnight. Next, membranes were incubated with HRP-conjugated IgG secondary antibodies (Santa Cruz Biotechnologies) for one hour. Protein bands were visualized using Western LightningTM Plus - Enhanced Chemiluminscence Substrate (Perkin Elmer Life & Analytical Sciences).

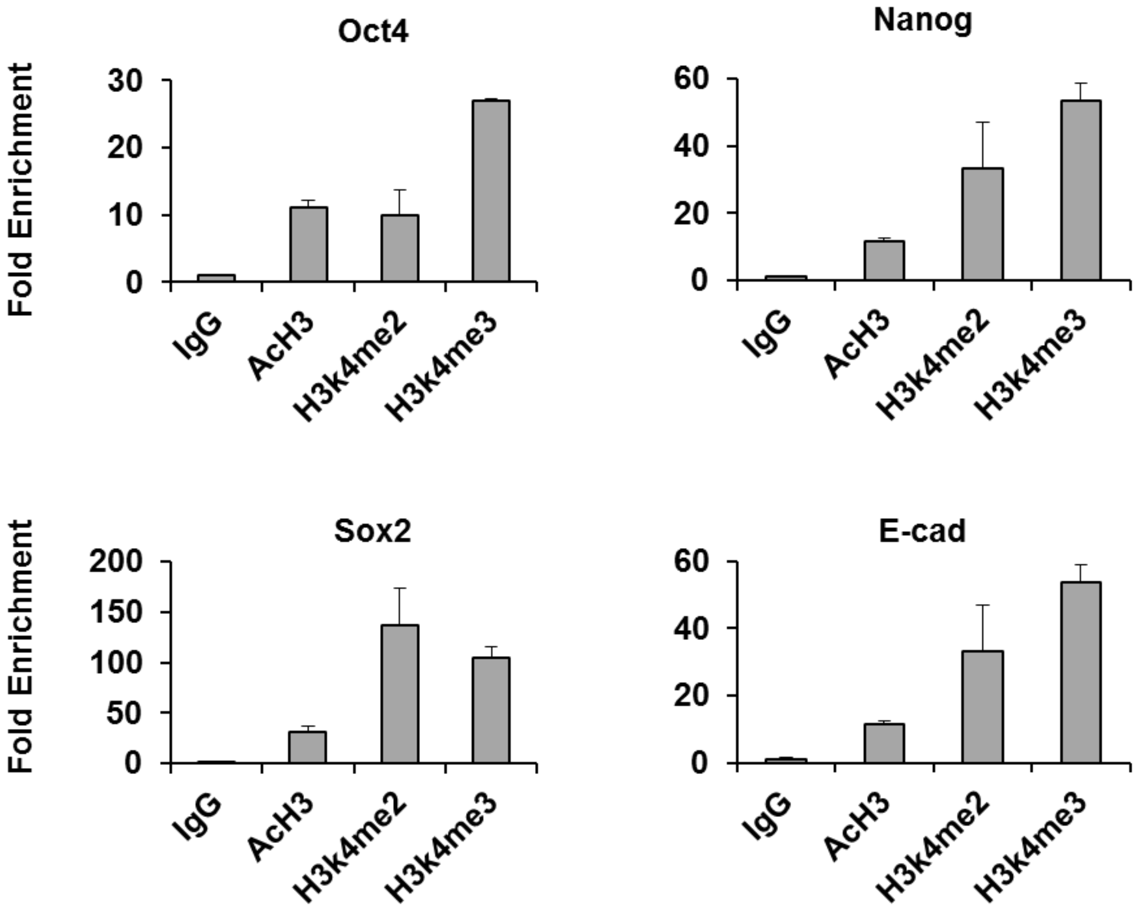

Figure 2.1. ChiP antibody fold enrichment. AcH3, H3k4me2 and H3k4me3 antibody fold enrichment over normal rabbit IgG control was quantified. Substantial enrichment was observed at the promoter regions of Oct, Sox2, Nanog, and E-cad genes following immunoprecipitation with antibodies against AcH3, H3k4me2 or H3k4me3.

Promoter	Forward Primer	Reverse Primer
Oct4	CCTAAGGGTTGTCCTGTCCA	GTGGAAAGACGGCTCACCTA
Sox2	CCCATTTATTCCCTGACAGC	GGGCTCCAAACTTCTCTCCT
Nanog	GGAGAATAGGGGGTGGGTAG	CAGCCTTCCCACAGAAAGAG
E-cad	TGGAATAGGAAGCTGGGAAG	CTCCCACACCAGTGAGCAG

Table 2.1. Forward and reverse primers used for ChIP-qPCR analysis.

Antibody	Company	Catalog #	Dilution/ Application
AcH3	Millipore	06-599	1:1000/WB; 1:500/IF
H3k4me2	Abcam	ab32356	1:1000/WB; 1:250/IF
H3k4me3	Millipore	07-473	1:1000/WB; 1:500/IF
HDAC1	Santa Cruz	sc-7872	1:1000/WB
HDAC2	Santa Cruz	sc-7899	1:1000/WB; 1:50/IF
HDAC3	Santa Cruz	sc1-1417	1:1000/WB
Actin	Santa Cruz	sc-1616	1:1000/WB
GAPDH	Santa Cruz	sc-32233	1:1000/WB
WDR5	Abcam	ab22512	1:1000/WB; 1:500/IF
H3	Abcam	ab1791	1:1000/WB
Nanog	Abcam	ab70482	1:500/IF
Oct4	Santa Cruz	sc-5279	1:50/IF
SSEA-1	Santa Cruz	sc-21702	1:50/IF
Sox2	Millipore	ab5603	1:500/IF

Table 2.2. Antibody information for immunostaining and Western blotting analysis.

Nuclear HDAC activity.

Nuclear HDAC activity was performed as previously described[37].

Statistical analysis.

The data are presented as mean, plus one standard deviation, where $n \geq 3$. Comparisons among values for groups greater than two were performed using a one-way analysis of variance (ANOVA). Differences between groups were then determined using a Tukey's post-hoc test. For two-group analysis, a two-tailed, unpaired t-test was used. For all cases, p-values less than 0.05 were considered statistically significant. GraphPad Prism® 6.0 software was used for all statistical evaluations.

2.3 Results and Discussion

2.3.1 Microtopography Enhances Cell Reprogramming

To assess whether topography might influence the process of cell reprogramming, primary fibroblasts, isolated from adult mouse ears, were first transduced using polycistronic lentiviral vectors, STEMCCA-loxP or STEMCCA-loxP-RedLight[40], encoding reprogramming factors OSKM or OSK, respectively. Following transduction, cells were seeded onto flat poly(dimethyl siloxane) (PDMS) membranes or those fabricated with parallel microgrooves of various width and spacing (40, 20, and 10 µm). The three-dimensional structure of PDMS membranes of 10 µm groove width is shown in Figure 2.2a. Groove heights were maintained at 3 µm for all cases. As expected, microgroove substrates had a dramatic effect on fibroblast alignment and nuclear elongation (Figure 2.2b). In general, cells aligned with microgrooves, and cell spreading decreased on microgrooves. In addition, nuclear shape index decreased (more elongated) as microgroove width and spacing decreased (Figure 2.3a). Cell proliferation, as quantified by EdU incorporation, also decreased slightly (Figure 2.3b).

After seeding, transduced cells were cultured in mouse ESC (mESC) culture conditions (see Figure 2.2c for the reprogramming procedure). After 12 to 14 days, iPSC colonies were subcultured and expanded or immunostained for Nanog protein expression and quantified. Colony formation was observed on all PDMS membranes. Interestingly, colonies formed on microgrooves exhibited a more elongated morphology relative to those formed on flat surfaces, and favored outgrowth along the axis of groove alignment (Figure 2.2d). In addition, we observed that microgroove topography significantly enhanced cell reprogramming efficiency in mouse fibroblasts transduced with OSKM, where microgrooves of 10 µm width (and spacing) displayed the most dramatic effect. Here, the number of Nanog+ colonies observed were over 4-fold higher than that seen on flat PDMS membranes (Figure 2.2e). A similar trend was observed in mouse fibroblasts infected with only 3 factors (OSK) (Figure 2.2f). This enhancement of reprogramming efficiency by microgrooves was also confirmed by using mouse fibroblasts isolated from Oct4-GFP reporter mice (Figure 2.4). Given that 10 µm-width grooves showed the greatest enhancement in cell reprogramming, we utilized these membranes to investigate the mechanism of action during additional experimentation.

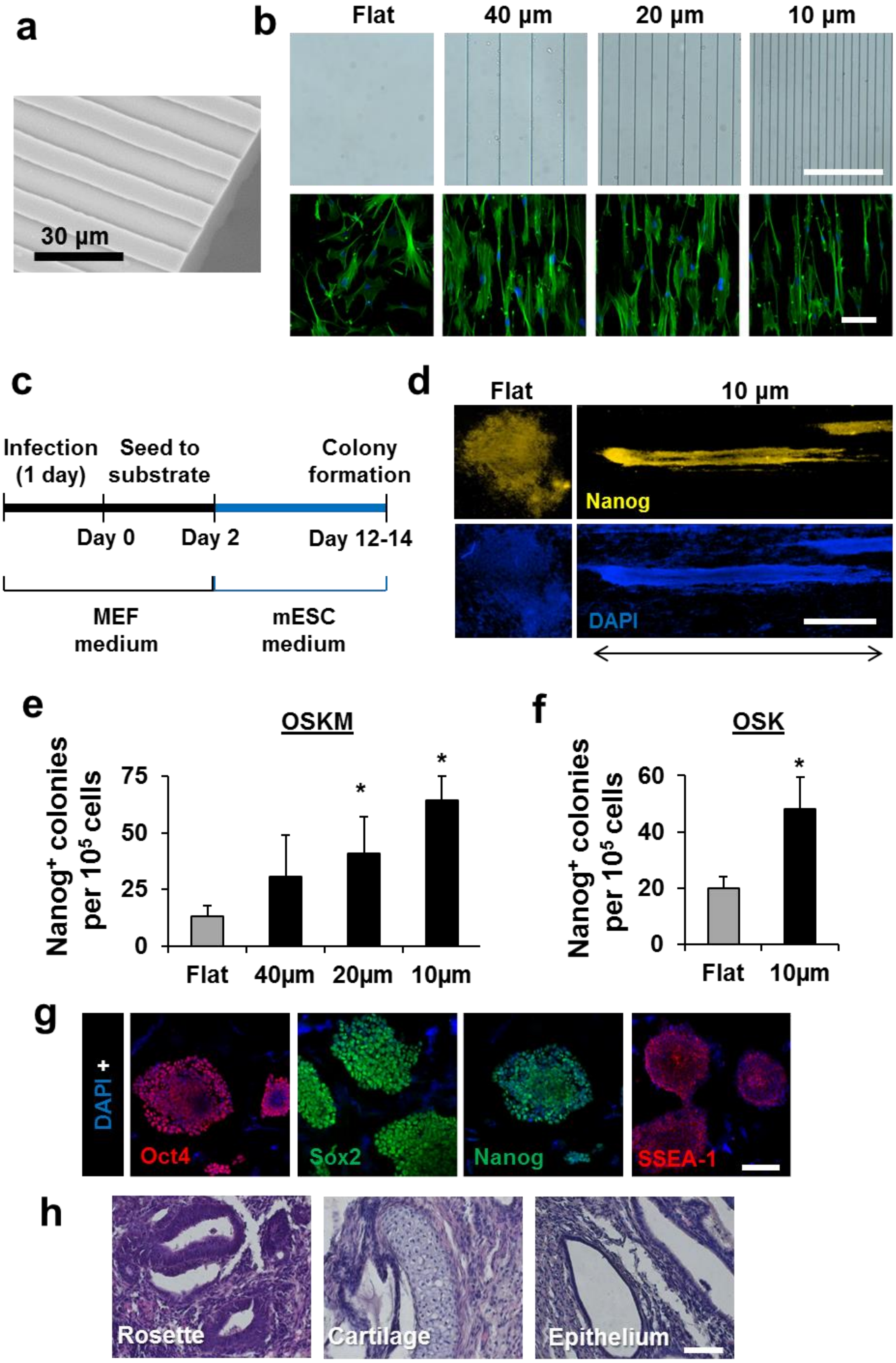
a
30 µm
b
Flat
40 µm
20 µm
10 µm
c
Infection (1 day)
Seed to substrate
Colony formation
Day 0
Day 2
Day 12-14
MEF medium
mESC medium
d
Flat
10 µm
Nanog
DAPI
e
OSKM
Nanog+ colonies per 10^5 cells
75
50
25
0
*
*
Flat
40µm
20µm
10µm
f
OSK
Nanog+ colonies per 10^5 cells
60
40
20
0
*
Flat
10µm
g
DAPI +
Oct4
Sox2
Nanog
SSEA-1
h
Rosette
Cartilage
Epithelium

Figure 2.2. Microgroove substrates altered fibroblast morphology and improved iPSC generation. a, Scanning electron micrograph (SEM) image of PDMS membranes with 10 µm groove width. All grooves were fabricated with a groove height of 3 µm. b, Top row shows phase contrast images of flat and grooved PMDS membranes with various width and spacing. Bottom row shows fibroblast morphology on various PDMS membranes. Images show fluorescence micrograph of the nucleus (DAPI, blue) and actin network (phalloidin, green) (scale bars, 100 µm). c, Reprogramming protocol. Colonies were subcultured and expanded or immunostained and quantified by day 12-14. d, Fluorescence micrograph shows the morphology of iPSC colonies generated on flat and grooved membranes (scale bar, 1mm). Groove dimensions were 10 µm width and spacing, denoted as "10 µm" in this and the rest of the figures. e, Reprogramming efficiency of fibroblasts transduced with OSKM and cultured on PDMS membranes with flat and grooved microtopography. The number of biological replicates, n, used for this experiment was equal to 6. Groove width and spacing were varied at 40, 20, and 10 µm. From here on out, differences of statistical significance are denoted by *, where p is less than 0.05 . f, Reprogramming efficiency in fibroblasts transduced with OSK (n=4). g, Immunostaining of stable iPSC line expanded from colonies generated on 10 µm grooves. These cells express mESC-specific markers Oct4, Sox2, Nanog, and SSEA-1 (scale bar, 100 µm). h, The expanded iPSCs in g were transplanted into SCID mice to demonstrate the formation of teratomas in vivo (scale bar, 50 µm).

To further characterize iPSCs, colonies generated on 10 µm-width grooved substrates were isolated and expanded for at least six passages. Colonies were then immunostained to confirm their expression of mESC-specific markers Oct4, Sox2, Nanog, and SSEA-1 (Figure 2.2g; Figure 2.5). Prior to immunostaining, we observed that iPSCs generated using STEMCCA-loxP-RedLight did not exhibit mCherry fluorescence, suggesting transgene expression was silenced after six passages (data not shown). In addition, we confirmed that the generated iPSCs were capable of forming teratomas in vivo (Figure 2.2h) and embryoid bodies in vitro, with differentiation potential for all three germ layers (Figure 2.6). Consistently, we also observed a similar trend in reprogramming efficiency of normal neonatal human dermal fibroblasts (NHDF) cultured on flat and microgrooved surfaces (Figure 2.7).

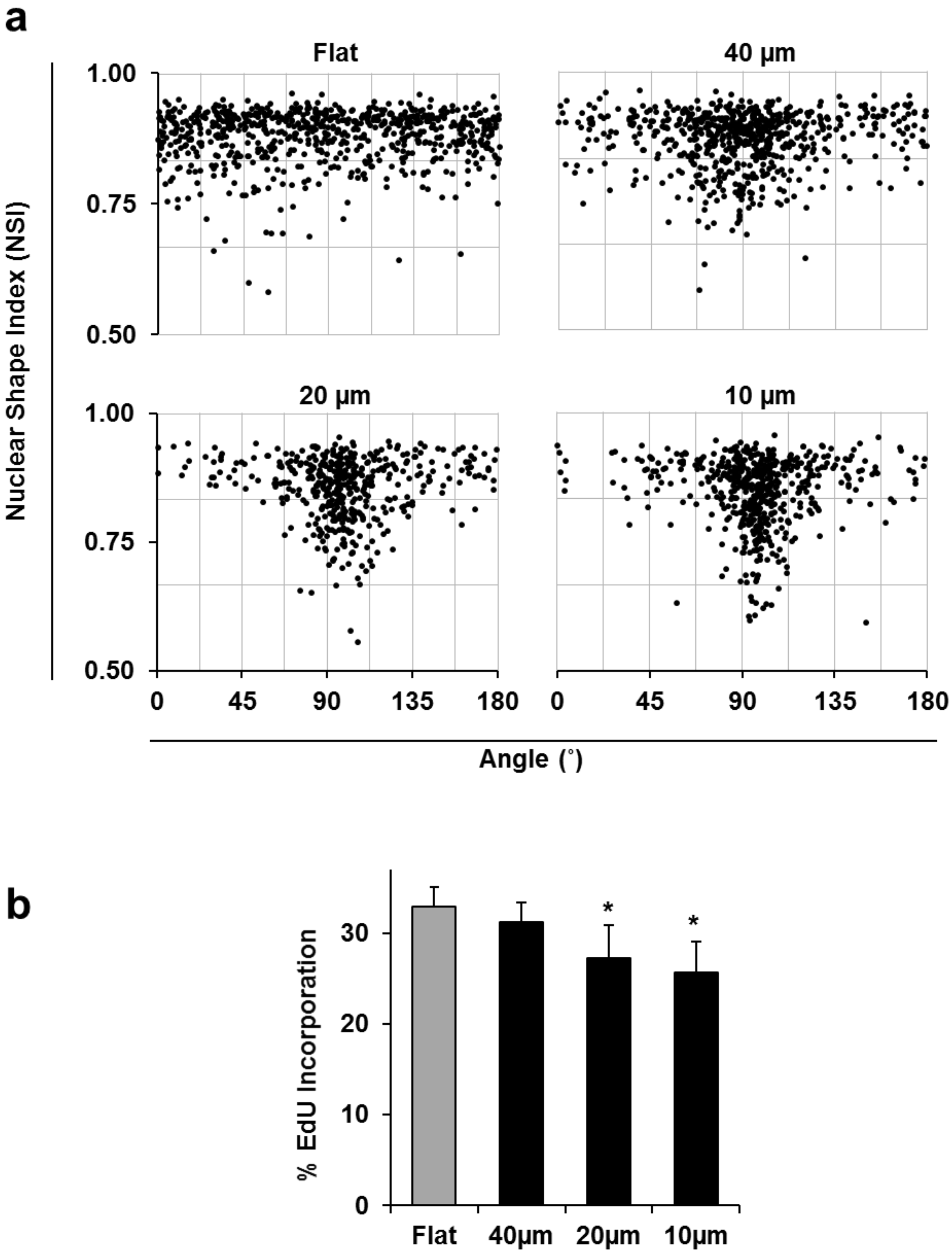

Figure 2.3. Effect of microgrooves on fibroblast nuclear shape and proliferation. a, Nuclear shape index (NSI) and alignment of fibroblasts cultured on different microgrooved substrates. We quantified nuclei elongation by calculating NSI according to the formula,

NSI = 4πA/P2, where A is nucleus projection area and P is nucleus perimeter. b, Edu incorporation analysis showing slight but significant decreases in fibroblast proliferation on microgrooved substrates (n=6). * indicates that there is statistically significant difference (p<0.05) compared with the control flat surface. Statistical analysis was performed by using ANOVA and post analysis.

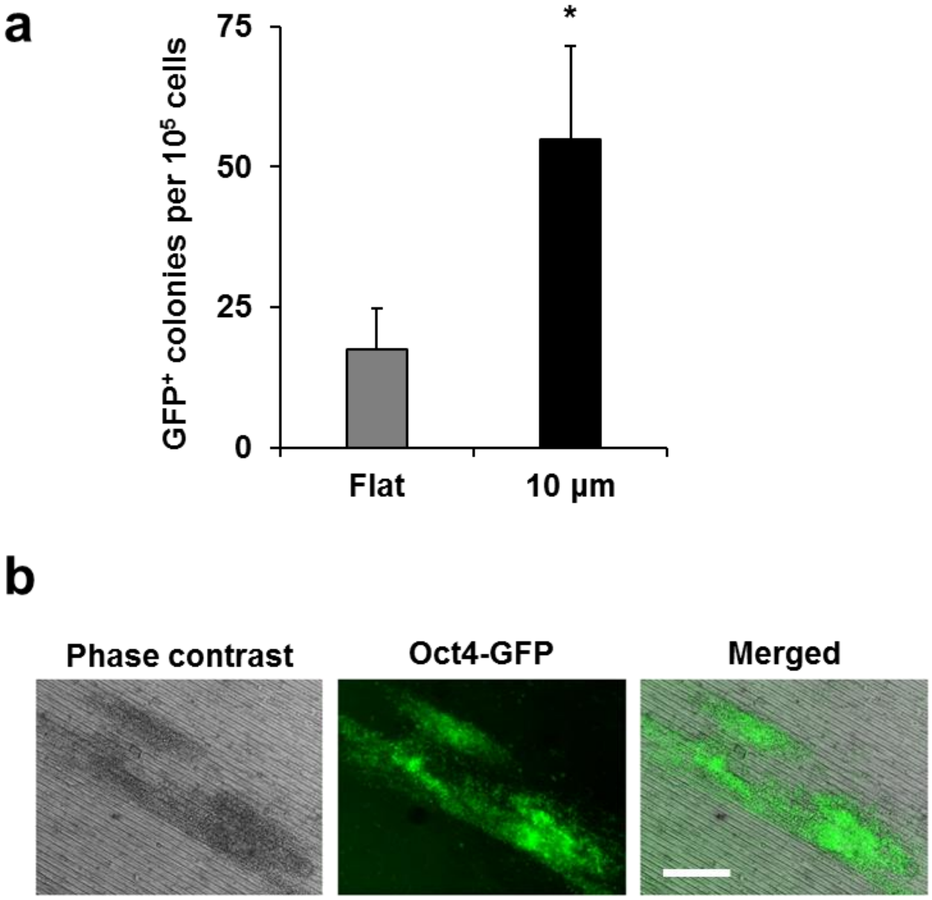

Figure 2.4. OSKM reprogramming on flat and microgrooved surfaces with Oct4-GFP mouse fibroblasts. a, Quantification of GFP+ colonies (n=4). * indicates that there is statistically significant difference (p<0.05) compared with the control flat surface. b, Phase contrast and fluorescence micrographs of GFP+ colonies (scale bar = 200 μm).

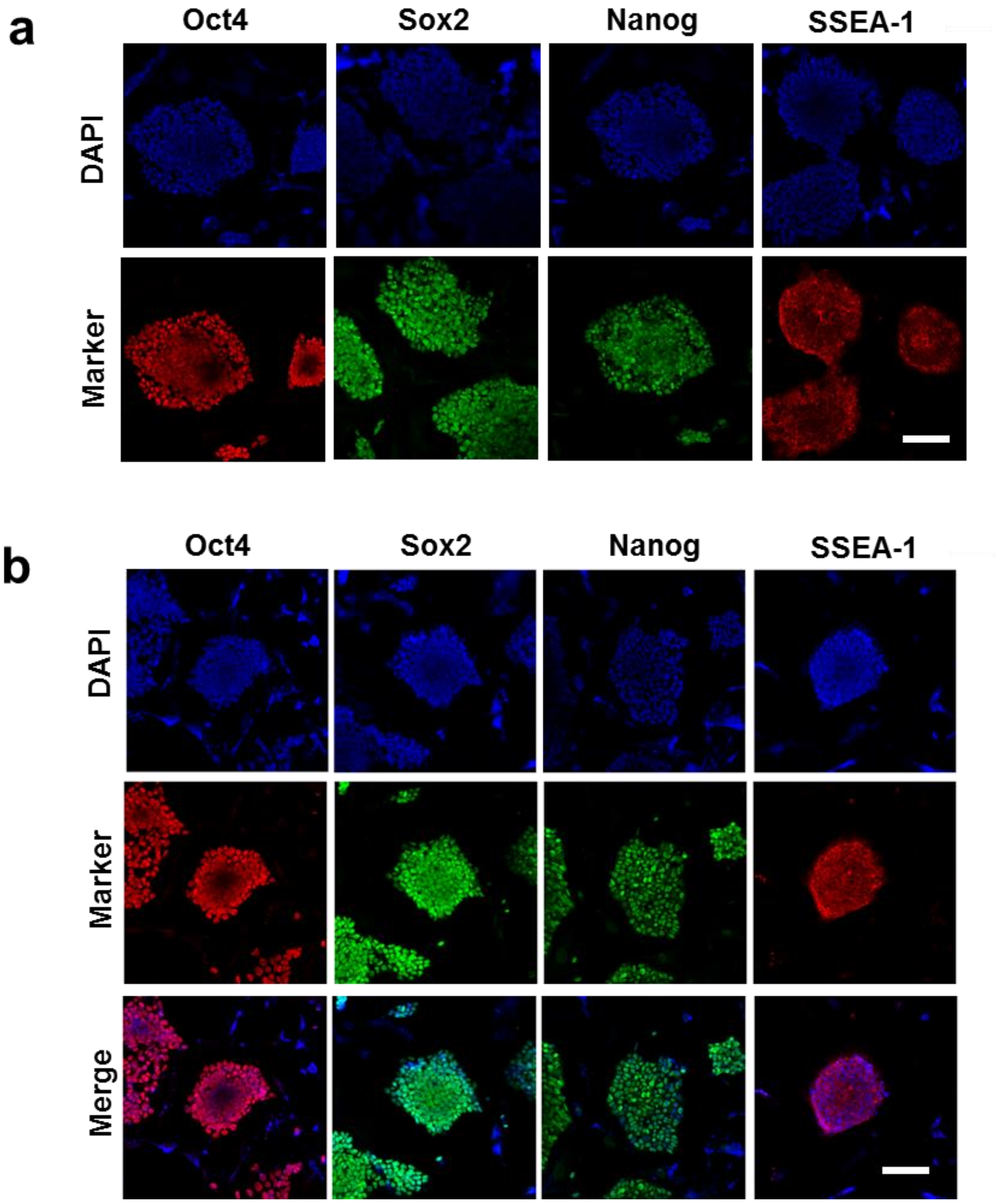

Figure 2.5. iPSC characterization. Immunostaining of iPSC colonies generated using OSK (a) and OSKM (b) reprogramming factors on grooves of 10 µm width. Colonies show nuclear localization of pluripotency genes Oct4, Sox2, and Nanog in generated iPSCs. Colonies also stained positive for SSEA-1, a cell surface marker specific to mESCs (scale bar = 100 µm).

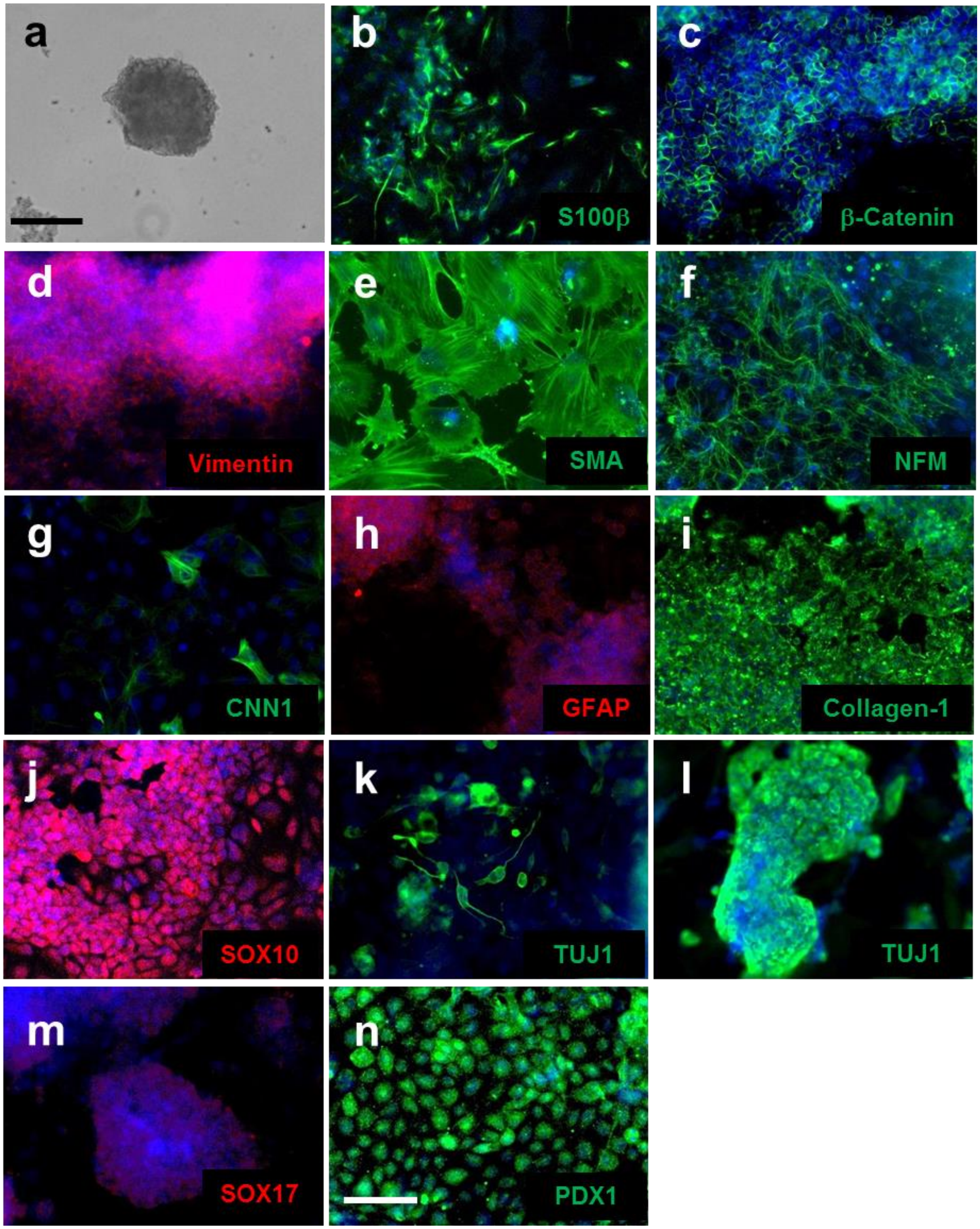

Figure 2.6. In vitro differentiation potential of mouse iPSC. a, iPSC embryoid body (EB) formation (scale bar = 200 µm). b-n, Immunostaining of spontaneously differentiated cells from iPSC EB. Cells express markers (shown in red or green) found in all germ layers. Cells are co-stained with DAPI for identification of nuclei (scale bar = 100 µm). Mouse iPSCs were differentiated for 2 weeks. Gene symbol key: S100 calcium binding protein B

(S100β); Cadherin associated protein, β1 (β -Catenin); Smooth muscle a-actin (SMA); Neurofilament medium polypeptide (NFM); Calponin 1 (CNN1); Glial fibrillary acidic protein (GFAP); SRY-box containing gene 10 (Sox10); SRY-box containing gene 17 (Sox17); b-III tubulin (TUJ1); pancreatic and duodenal homeobox 1 (PDX1).

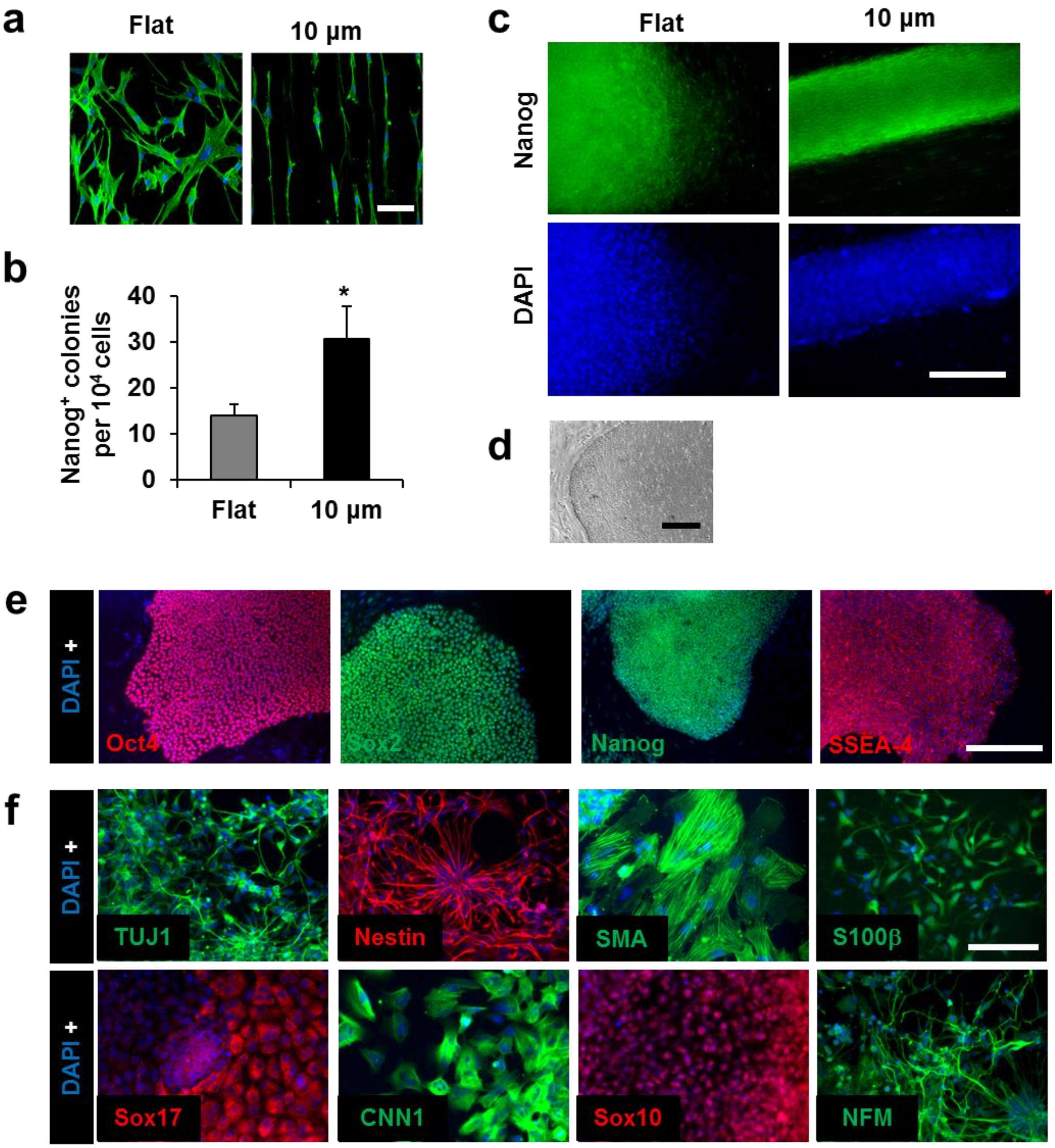

Figure 2.7. Effects of microtopography on human cell reprogramming. a, Images show fluorescence micrograph of nucleus (DAPI, blue) and actin network (phalloidin, green) of normal neonatal human dermal fibroblasts (NHDF) on flat and microgrooved PDMS surfaces (scale bars=100 μm). b, Reprogramming efficiency of NHDF transduced with

OSKM and cultured on PDMS membranes with flat and microgrooved surfaces. * indicates $p<0.05$ (n=6). c, Fluorescence micrographs show iPSC colonies generated on flat and microgrooved surfaces. d, Phase contrast image shows expanded colony morphology. e, Fluorescence micrograph shows expression of pluripotency markers in generated clones. (scale bar in c-e, 200 µm). f, In vitro differentiation potential of NHDF-iPSCs (scale bar = 100 µm).

2.3.2 Biophysical Regulation of Histone Modifications

Modulation of chromatin-modifying enzymes has a direct effect on cell reprogramming[16]. In addition, somatic cells must undergo dramatic changes in chromatin structure in order to overcome the epigenetic barriers of cell reprogramming[14,15]. A number of these barriers as they relate to histone modifications have been well characterized. Based on our previous observations in mesenchymal stem cells (MSCs)[37], we postulated that microgroove topography might increase the presence of histone H3 acetylation (AcH3) marks in adult fibroblasts, which tend to promote cell reprogramming. For this reason, we performed a Western blotting analysis to monitor global changes in AcH3 and other histone marks shown to influence cell reprogramming.

Through our analysis, we found that microgrooves dramatically increased global AcH3 marks in non-transduced mouse fibroblasts (Figure 2.8a) in the absence of reprogramming factors. Interestingly, we also observed an increase in methylation (both di- and tri-methylation) of histone H3 at lysine 4 (H3k4me2 and H3k4me3, respectively) on microgrooved substrates relative to flat surface (Figure 2.8a). A similar trend in histone modifications was observed in fibroblasts infected with OSKM (Figure 2.9). Confocal microscopy confirmed that this increase was localized in the nucleus (Figure 2.8b). Because AcH3, H3k4me2 and H3k4me3 marks are associated with transcript activation and/or critical in the early phase of reprogramming[41], we performed a chromatin immunoprecipitation (ChIP)-quantitative polymerase chain reaction (qPCR) assay at the promoter regions of Oct4, Sox2, and Nanog –the key regulators of the pluripotency network. ChIP analysis revealed significant increases in AcH3 at all three promoter regions on microgrooves relative to flat surfaces. The promoter region of Nanog showed a significant increase in H3k4me2 marks, while the promoter region of Sox2 showed a significant increase in H3k4me3 marks (Figure 2.8c). These data suggest that microgroove topography can induce global and local changes in histone H3 acetylation and methylation that are highly favorable in the activation of reprogramming genes.

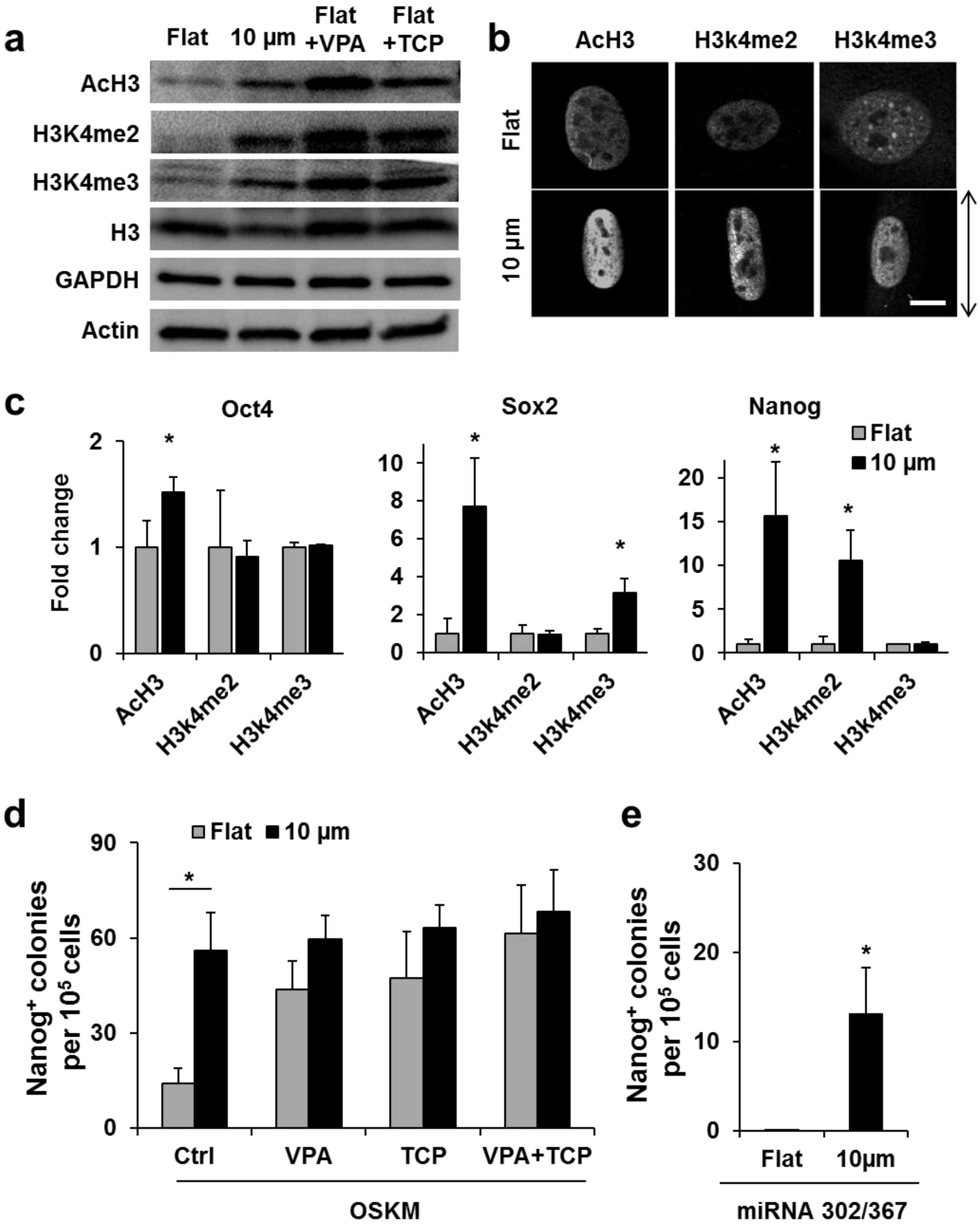

Figure 2.8. Microtopography induced histone modifications and replaced VPA and TCP in reprogramming. a, Mouse fibroblasts were cultured on microgrooved or flat surfaces in the absence or presence of VPA or TCP for 3 days, followed by Western blotting analysis of histone modifications AcH3, H3k4me2, and H3k4me3. Total histone H3, GAPDH and Actin are shown as loading controls. b, Confocal microscopy shows the fluorescence intensity of histone modifications localized in the nucleus (scale bar, 10 μm). c, ChIP-

qPCR analysis shows fold enrichment of histone modifications at the promoter regions of Oct4, Sox2, and Nanog (n=3). d, Reprogramming efficiency of fibroblasts transduced with OSKM in the presence of chemical compounds, VPA and TCP (n=5). e, Quantification of colony formation in fibroblasts transduced with miRNA 302/367 in the absence of VPA (n=4).

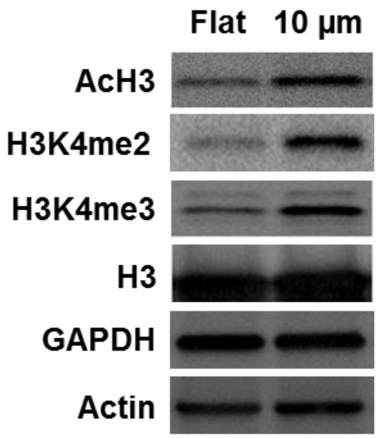

Figure 2.9. Biophysical regulation of epigenetics following the forced expression of OSKM. Western blotting analysis of mouse fibroblasts infected with OSKM and cultured on flat and microgrooved surfaces for 8 days.

To further test the hypothesis that the observed increases in histone H3 acetylation and methylation on microgrooves play a role in topography-enhanced cell reprogramming, we compared the microgroove effect with that of potent small molecule epigenetic modifiers. In particular, VPA and TCP –HDAC and histone demethylase (HDM) enzyme inhibitors, respectively –have been shown to greatly improve cell reprogramming efficiency[9,11]. Both VPA and TCP induced global increases in AcH3, H3k4me2, and H3k4me3 in our system (Figure 2.8a), suggesting that VPA and TCP had some overlapping effects on histone modifications. To test whether microgrooves and VPA or TCP have similar effects on cell reprogramming, we reprogrammed fibroblasts cultured on flat and microgrooved membranes in the absence or presence of chemical compounds –VPA and TCP, alone or combined. From this experiment, we make several noteworthy observations. As expected, VPA and TCP alone produced a significant increase in the number of Nanog+ colonies observed when the cells were reprogrammed on flat membranes (Figure 2.8d). Interestingly, the number of colonies generated on flat membranes in the presence of chemical compounds increased to comparable levels with that of microgrooves in the absence of VPA and TCP, indicating that microgroove substrates had a similar effect to the chemical compounds in enhancing reprogramming efficiency. In addition, VPA and TCP showed no effect on the number of Nanog+ colonies formed on microgrooves, suggesting that their mechanism of action might share a similar pathway in improving reprogramming efficiency.

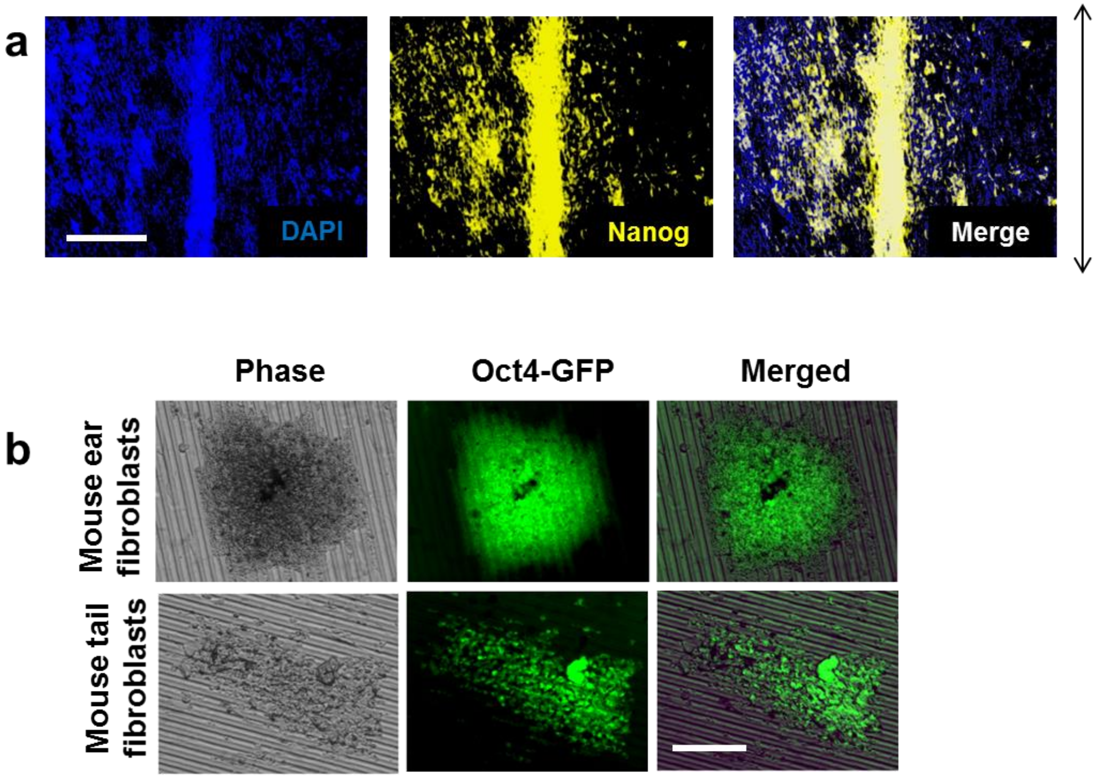

Figure 2.10. miRNA generated iPSC-like colonies. a, Fluorescence micrograph shows Nanog expression in iPSC-like colonies generated from wild-type mouse ear fibroblasts on microgrooved surfaces (scale bar = 1 mm) . b, Phase contrast and fluorescence micrograph of GFP+ colonies generated from mouse ear fibroblasts and mouse tail fibroblasts isolated from Oct4-GFP reporter mice (scale bar = 100 μm).

Because VPA was shown to be necessary for the generation of miRNA-induced pluripotent stem cells in mouse fibroblasts[13], although complete reprogramming may not be consistently achieved[42], we tested the ability of microgrooved membranes to generate colonies under the forced expression of the miRNA cluster 302/367 in the absence of VPA. Remarkably, we were able to generate colonies only on microgrooves but not on flat membranes (Figure 2.8e). We were also unable to generate any colonies with VPA alone. While our microgrooved surfaces showed the ability to form Nanog and GFP positive clones (using fibroblasts isolated from wild-type and Oct4-GFP reporter mice, respectively) (Figure 2.10), we were unable to expand these iPSC-like colonies, suggesting that microgrooved surfaces could enhance the early stage of cell reprogramming and additional chemical or reprogramming factors may be necessary to achieve complete reprogramming into iPSCs. Here, we report the ability of microgroove topography to replace or mimic the effects of chemical compounds, VPA and TCP, in cell reprogramming.

2.3.3 Mediators of Mechanotransduction, MET, and Actin-Myosin Contractility

To elucidate the upstream mechanotransduction pathways involved in the regulation of the histone H3 modifications observed, we first monitored nuclear HDAC activity in fibroblasts cultured on microgrooved and flat membranes. Indeed, nuclear HDAC activity was significantly reduced on microgrooved substrates relative to the flat surface (Figure 2.11a), which may account for the topography-induced AcH3. Western blotting analysis was performed to examine the expression of several HDAC proteins in mouse fibroblasts. Our results indicate that microgrooves induce drastic deceases in the expression of HDAC2 but not HDAC1 and HDAC3 (Figure 2.11b). By using confocal microscopy, we observed a presence of HDAC2 specifically within the nucleus of mouse fibroblasts, which is dramatically decreased on microgrooves (Figure 2.11c). Since miRNA-mediated reprogramming was shown to be specifically dependent on VPA-induced degradation of HDAC2 protein, microgrooved topography, as with VPA, might promote the increase in global AcH3 through the downregulation of HDAC2, which may lead to the observed enhancement in cell reprogramming via OSKM and in the partial reprogramming via miRNA302/367 transduction (Figure 2.2e and 2.8e).

To investigate potential upstream mediators of the observed increase in H3k4 methylation on microgrooves, we screened for regulators of histone methylation. Given the recent evidence that WD repeat domain 5 (WDR5) –a subunit of H3 methyltranferase – mediates both cell reprogramming and ESC self-renewal[43], we probed for its expression through Western blotting analysis and immunostaining. Interestingly, we observed that microgrooves dramatically upregulated the expression of WDR5 in mouse fibroblasts (Figure 2.11d-e). This result led us to perform RNA interference on WDR5 in the presence of microgrooves to determine its effects on histone modifications. Sufficient knockdown of WDR5 was confirmed at protein and gene expression levels (Figure 2.11f and Figure 2.12). Surprisingly, WDR5 knockdown on grooves resulted in substantially lower levels of both H3k4me2 and H3k4me3 as well as AcH3 in mouse fibroblasts (Figure 2.11f), suggesting that WDR5 plays a critical role in the modulation of both histone methylation and acetylation marks. This result also presents a novel role of WDR5 as a key mediator of mechanotransduction.

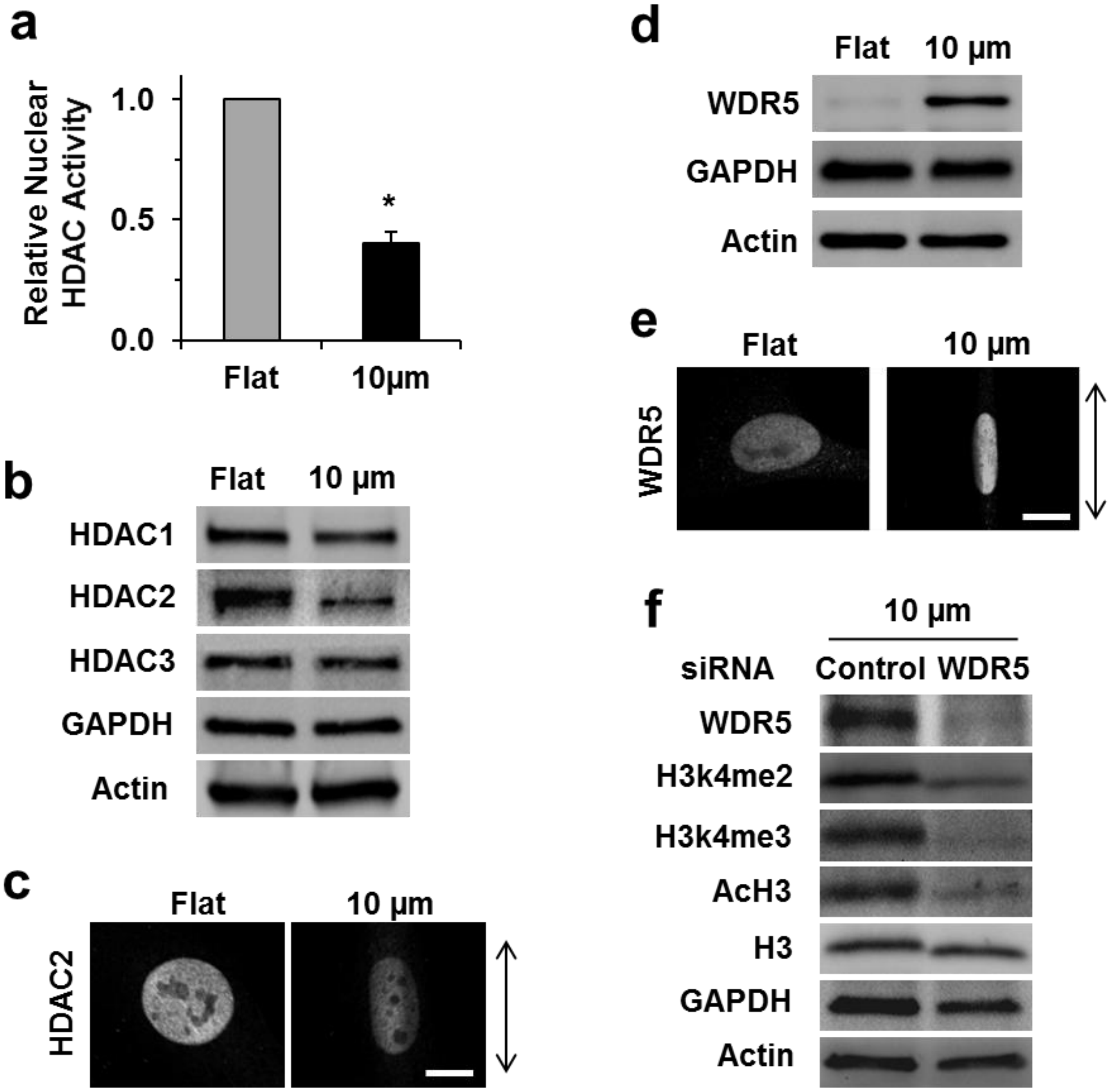

Figure 2.11. Microtopography reduced HDAC activity, downregulated HDAC2, and upregulated WDR5. For these experiments, mouse fibroblasts were analyzed after being cultured on flat or microgrooved surfaces for 3 days. a, Nuclear HDAC activity assay (n=3). b, Western blotting (WB) analysis of HDACs. c, Confocal microscopy of HDAC2 staining. d, WB analysis of WDR5. e, Confocal microscopy of WDR5. f, WB analysis performed on fibroblasts cultured on microgrooves after siRNA knockdown of WDR5. (Scale bars in c and e, 10 µm)

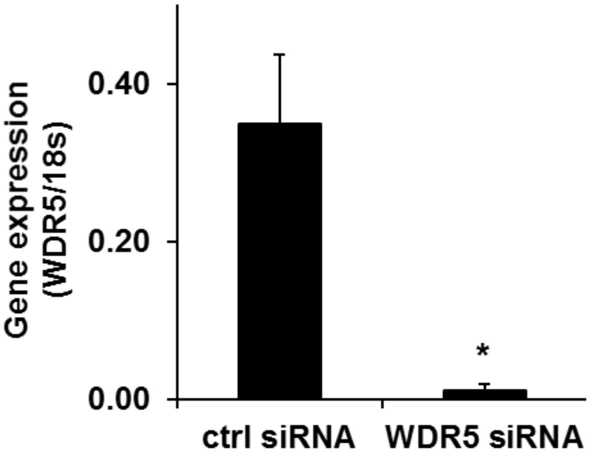

Figure 2.12. WDR5 RNA interference. qRT-PCR confirms the successful siRNA knockdown of WDR5 gene expression. Gene expression was normalized to 18S. * $p<0.05$ (n=3).

MET is required for nuclear reprogramming in mouse fibroblasts[7]. In addition, a number of studies have implicated the roles of both HDAC2 and WDR5 in the expression of several epithelial and mesenchymal-associated genes[44,45]. For these reasons, we monitored the effect of microgroove topography on the expression of several genes associated with a MET. Real-time RT-PCR analysis (qPCR) of non-transduced fibroblasts cultured on microgrooves for 3 days showed increased mRNA (relative to those cultured on flat membranes) for several epithelial-related genes (e.g., E-cad, epithelial cell adhesion molecule [Ep-CAM], keratin 8 [Krt8], occludin [Ocln], and claudin 3 [Cldn3]) and reduced mRNA for multiple mesenchymal markers (e.g., transforming growth factor β receptor 1 [Tgfbr1], snail homolog 1 [Snai1], snail homolog 2 [Snai2], vimentin [Vim], and integrin β1 [Itgb1]). This result suggests that microgroove topography promotes the initiation of a MET in adult mouse fibroblasts (Figure 2.13a). In an effort to link the histone modifications observed on microgrooved surfaces to the observed increases in epithelial-related gene expression, we performed ChIP-qPCR analysis on histone H3 modifications at the promoter of E-cad. Indeed we observed increases in the presence of H3k4me2 at the E-cad promoter (Figure 2.13b). Other marks showed no detectable change (Figure 2.14), suggesting that H3k4me2 mediates the enhanced E-cad expression and MET transition on microgrooves. Activation of transforming growth factor-β (TGF-β) pathways has been shown to block MET in cell reprogramming[7].

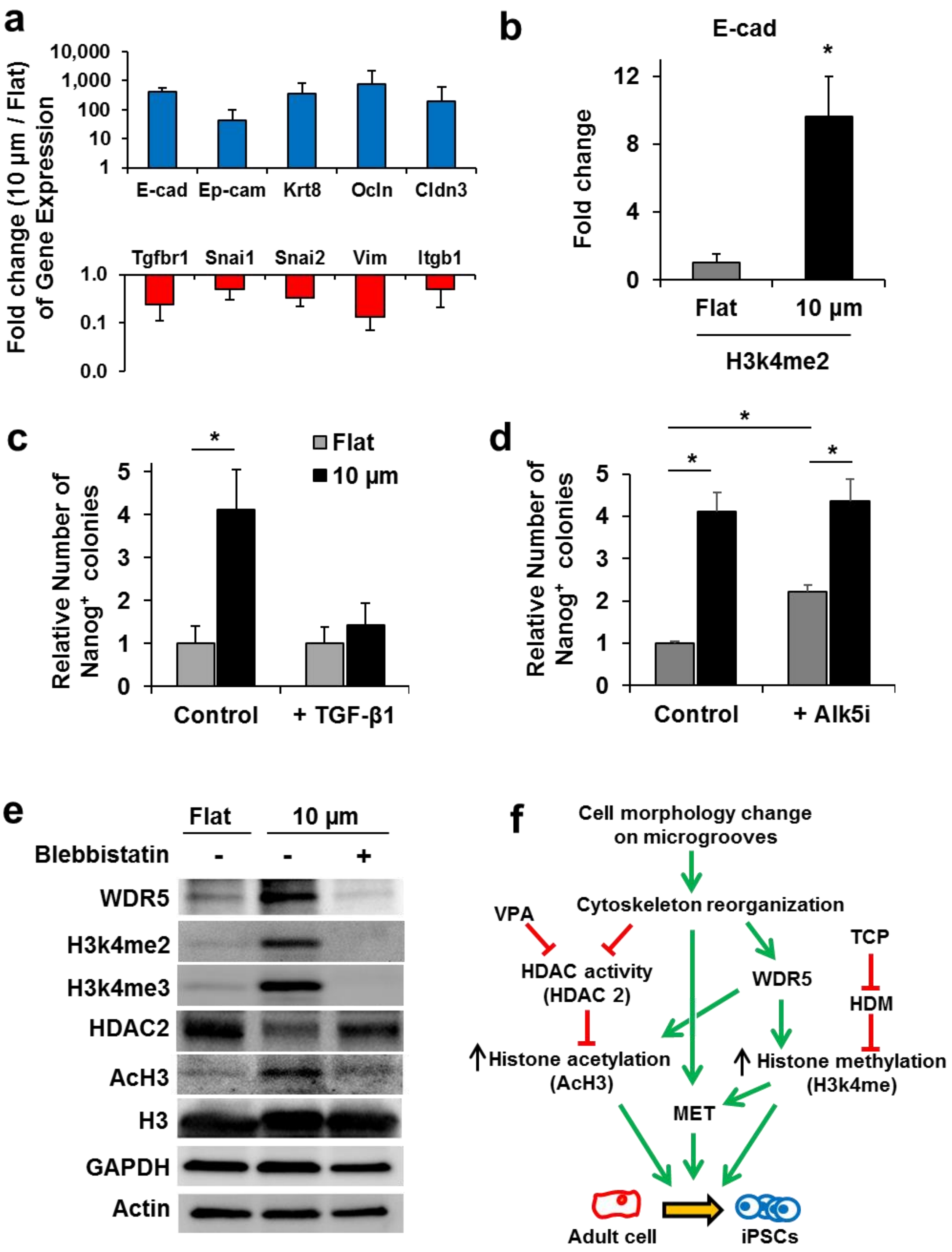

Figure 2.13. Initiation of MET and contractility dependent histone modifications. a, Mouse fibroblasts were cultured for 3 days on flat or microgrooved surfaces, followed by qRT-PCR analysis of epithelial-related genes and mesenchymal genes (n=3). b, ChIP-qPCR analysis for the fold enrichment of H3k4me2 modifications at the promoter region of E-

cad (n=3). c-d, Mouse fibroblasts were reprogrammed with OSKM in the absence or presence of (c) MET inhibitor, TGF-β1, or (d) TGF-β inhibitor, A-83-01 (Alk5i), and the number of Nanog+ colonies generated was quantified (n=5 and n=4, respectively). e, Western blotting analysis of mouse fibroblasts cultured on flat or microgrooved surfaces for 3 days in the absence or presence of blebbistatin. f, A summary of microtopographical regulation of histone modifications and cell reprogramming in adult mouse fibroblasts.

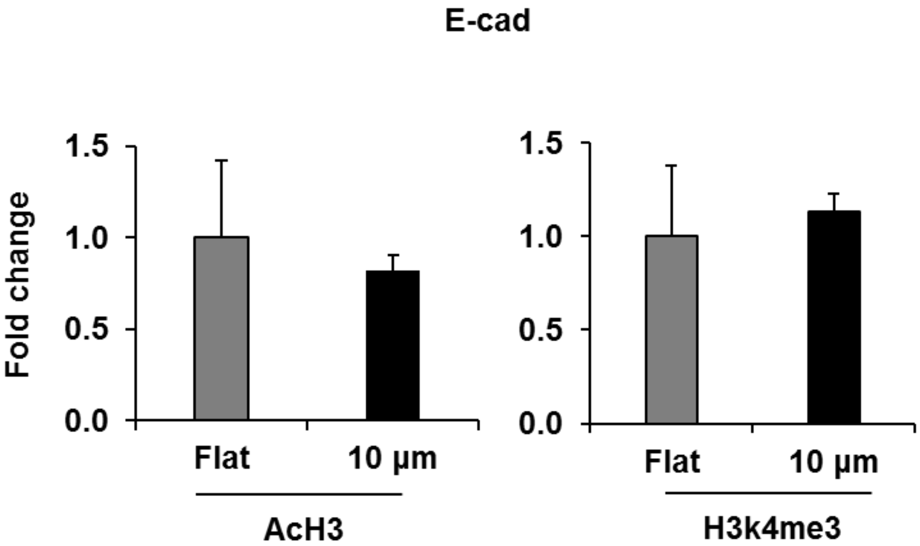

Figure 2.14. ChIP-qPCR analysis. ChIP-qPCR analysis shows that there is no significant fold enrichment of histone modifications, AcH3 and H3k4me3, at the promoter region of E-cad (n=3).

To study whether the observed MET plays a role in the topographical enhancement of cell reprogramming, we tested the effect of microgrooves on cell reprogramming in the presence of TGF-β1. As shown in Figure 2.13c, TGF- β1 completely blocked the enhanced reprogramming by microgroove topography. Furthermore, inhibition of the TGF-β pathway using Alk5i increased reprogramming efficiency on flat surfaces as expected, but showed no synergistic behavior in reprogramming efficiency on microgrooves (Figure 2.13d). Taken together, these results suggest that the MET induced by microgrooves plays an important role in topography-enhanced cell reprogramming.

Microgroove topography facilitates dramatic cytoskeleton reorganization in fibroblasts. Still, it is not clear how or if these cytoskeletal changes are important in the mechanomodulation of histone modifications and their upstream regulators. For this reason, we disrupted actin-myosin contractility in fibroblasts via treatment with blebbistatin, a non-muscle myosin-II inhibitor. Remarkably, blebbistatin treatment eliminates the effect of microgrooves on the epigenetic modulation of AcH3, H3k4me2, and H3k4me3 as well as the mediators HDAC2 and WDR5 (Figure 2.13e). This data strongly suggests that the cytoskeleton reorganization observed in fibroblasts on microgrooves and the actin-myosin contractility are critical in this mechanomodulation of epigenetic state and thus cell reprogramming. Figure 2.13f summarizes the effects of microgrooves on histone modifications and cell reprogramming in adult mouse fibroblasts.

2.3.4 Nanoscale Epigenetic Regulation

Nanofibrous scaffolds can regulate cell morphology, cell organization and cell migration, similar to microgrooves[23,25]. To generalize the role of topography in epigenetic mechanomodulation, we employed the use of nanofibrous membranes in our studies. Figure 2.15a shows nanofiber structure in aligned and random orientations and its effect on fibroblast morphology. As with microgrooves, aligned nanofibers encouraged fibroblast alignment and elongation over the random nanofibers. Western blotting analysis revealed that fibroblasts cultured on aligned nanofibers also exhibit global increases in AcH3, H3k4me2, and H3k4me3 marks over fibroblasts cultured on random fibers (Figure 2.15b). In addition, these changes correlated well with the decrease in HDAC2 and the increase in WDR5 protein expression. Next, we seeded fibroblasts transduced with OSKM onto nanofiber surfaces to test the effects of random and aligned fiber orientation on reprogramming efficiency. Indeed, aligned nanofibers generated significantly more Nanog+ colonies than random fibers (Figure 2.15c-d and Figure 2.16). These results confirm that nanofiber alignment produces an effect similar to microgrooves in epigenetic modification and cell reprogramming.

2.3.5 Cell Shape Effect on Histone Modifications

A common effect of microgrooves and aligned nanofibers is cell elongation. To directly test if this cell morphology change is sufficient to induce histone modifications or whether topography is required, we utilized micropatterning techniques to gain tight control over cell shape while culturing cells on topographically flat surfaces. Fibroblasts were cultured on micropatterned islands with well-defined cell shapes (round or elongated). Interestingly, fluorescence microscopy revealed that cells in an elongated shape (cell shape index or CSI = 0.1) exhibited significantly higher levels of nuclear AcH3, H3k4me2, and H3k4me3 as compared to cells in a circular shape (CSI = 1) (Figure 2.15e,f) with an equal spreading area. This data suggests that the morphological change experienced by fibroblasts, when interacting with the nano- and micro-scale features of cell adhesive materials is sufficient to induce epigenetic modifications. Cell elongation also significantly correlated with an elongation of the cell nucleus (Figure 2.17).

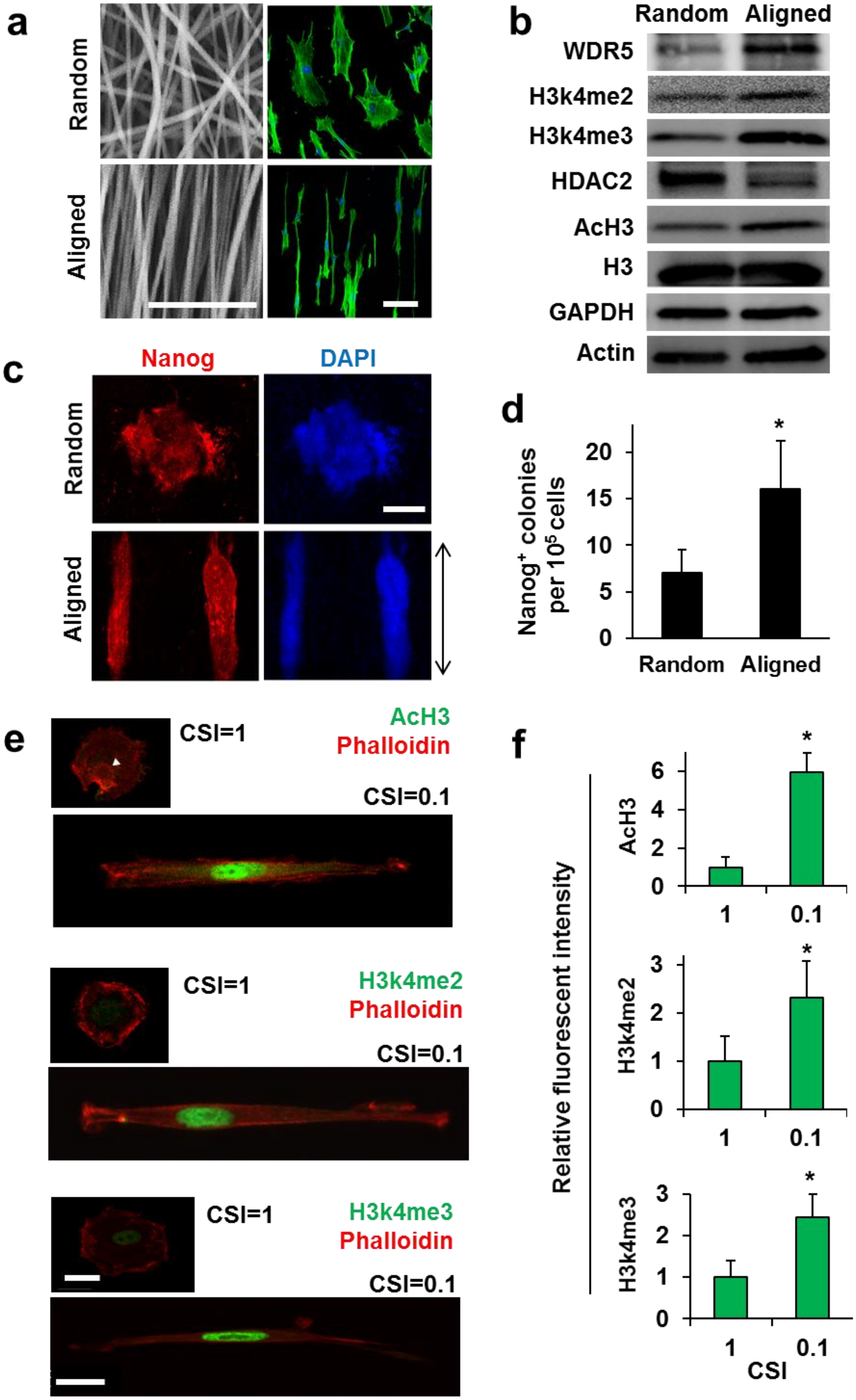
a
Random
Aligned
b
Random
Aligned
WDR5
H3k4me2
H3k4me3
HDAC2
AcH3
H3
GAPDH
Actin
c
Nanog
DAPI
Random
Aligned
d
Nanog$^+$ colonies per 10^5 cells
0
5
10
15
20
*
Random
Aligned
e
CSI=1
AcH3
Phalloidin
CSI=0.1
CSI=1
H3k4me2
Phalloidin
CSI=0.1
CSI=1
H3k4me3
Phalloidin
CSI=0.1
f
Relative fluorescent intensity
AcH3
0
2
4
6
*
1
0.1
H3k4me2
0
1
2
3
*
1
0.1
H3k4me3
0
1
2
3
*
1
0.1
CSI

Figure 2.15. Nanoscale and morphological regulation of histone modifications and cell reprogramming. a, SEM of nanofibers shows fiber morphology in aligned and random orientations (scale bar, 20 µm). Confocal fluorescence micrograph of fibroblasts cultured on nanofibers (DAPI [blue] and phalloidin [green] staining) (scale bar, 100 µm). b, Western blotting analysis for fibroblasts cultured on random and aligned nanofibers for 3 days. c, Fibroblasts were transduced with OSKM and seeded onto nanofiber surfaces, followed by immunostaining for Nanog expression (red) at day 12. Nuclei were stained with DAPI in blue, scale bar=500 µm. d, Quantification of colony numbers in c (n=5). e, Fibroblasts were micropatterned into single cell islands of 2000 µm2 area with cell shape index (CSI) value of 1 (round) or 0.1 (elongated). After 24 hrs, cells were immunostained for AcH3, H3k4me2, or H3k4me3 (in green). Phalloidin staining (red) identifies the cell cytoskeleton for cell shape accuracy. The white arrow indicates the location of nucleus (scale bars, 20 µm). f, Quantification of fluorescence intensity in e (n = 34, 20, and 34 for AcH3, H3k4me2, and H3k4me3, respectively).

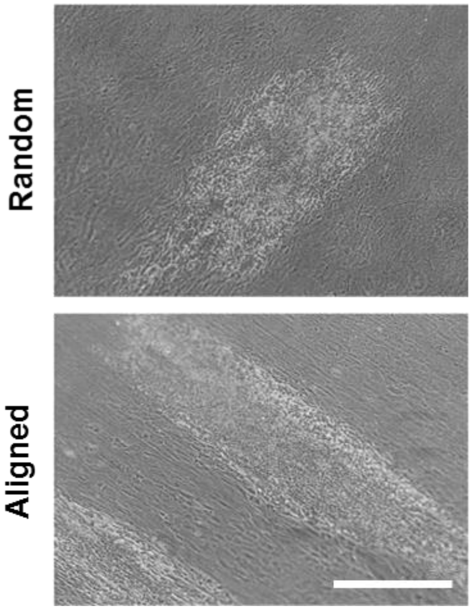

Figure 2.16. iPSC colony morphology on random and aligned nanofibers. Phase contrast image shows iPSC colony elongation on aligned versus random nanofibers (scale bar = 500 µm).

Our results demonstrate, for the first time, that biophysical cues, in the form of parallel microgrooves or aligned nanofibers on the surface of cell-adhesive substrates, can significantly improve reprogramming efficiency and replace the effects of small molecule epigenetic modifiers. The mechanism behind this biophysical enhancement of cell reprogramming relies on mechanomodulation of H3 acetylation and methylation marks, which are regulated by HDAC2 and WDR5. These epigenetic changes may also play a role in the increased epithelial-related genes on microgrooved membranes. We believe this novel biophysical regulation of epigenetics has important implications in the broad scope of cell biology and provides a rational basis for the optimization of biomaterials and the cellular microenvironment for a number of biological applications.

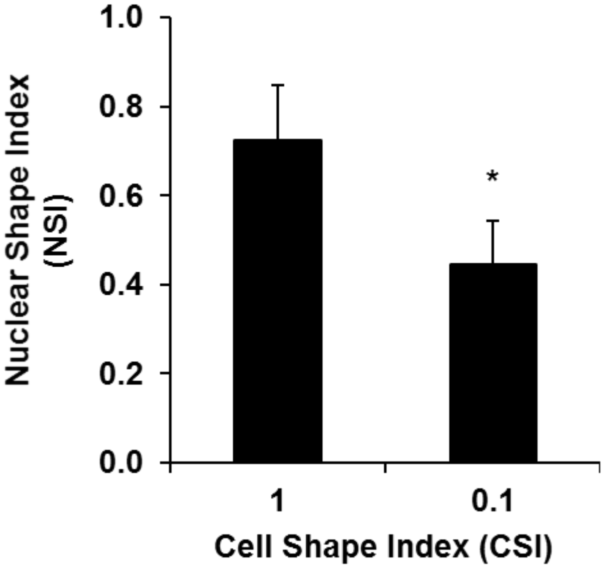

Figure 2.17. Effect of cell shape on nuclear shape index (NSI). Quantification of NSI for fibroblasts seeded onto micro-islands of round (CSI=1) and elongated (CSI=0.1) morphologies.

2.3.6 Effect of Substrate Rigidity on Cell Reprogramming

To assess whether substrate rigidity can modify the efficiency of reprogramming with different numbers and combinations of exogenous transcription factors (TFs), cells were transduced with various lentiviral polycistronic reprogramming vectors, each comprised of a different combination of reprogramming TFs (Figure 2.18A). These combinations include: OSKM, OSK, OSM, SKM, and OKM (EGFP for control). Twenty-four hours after transduction, cells were split and plated onto collagen coated PA gels of variable stiffness (ranging from 0.6 to 40 kPa and glass). After seeding, cells were cultured in mouse ESC (mESC) maintenance media for 11 days. At day 11 cells were fixed and immunostained for nanog protein expression.

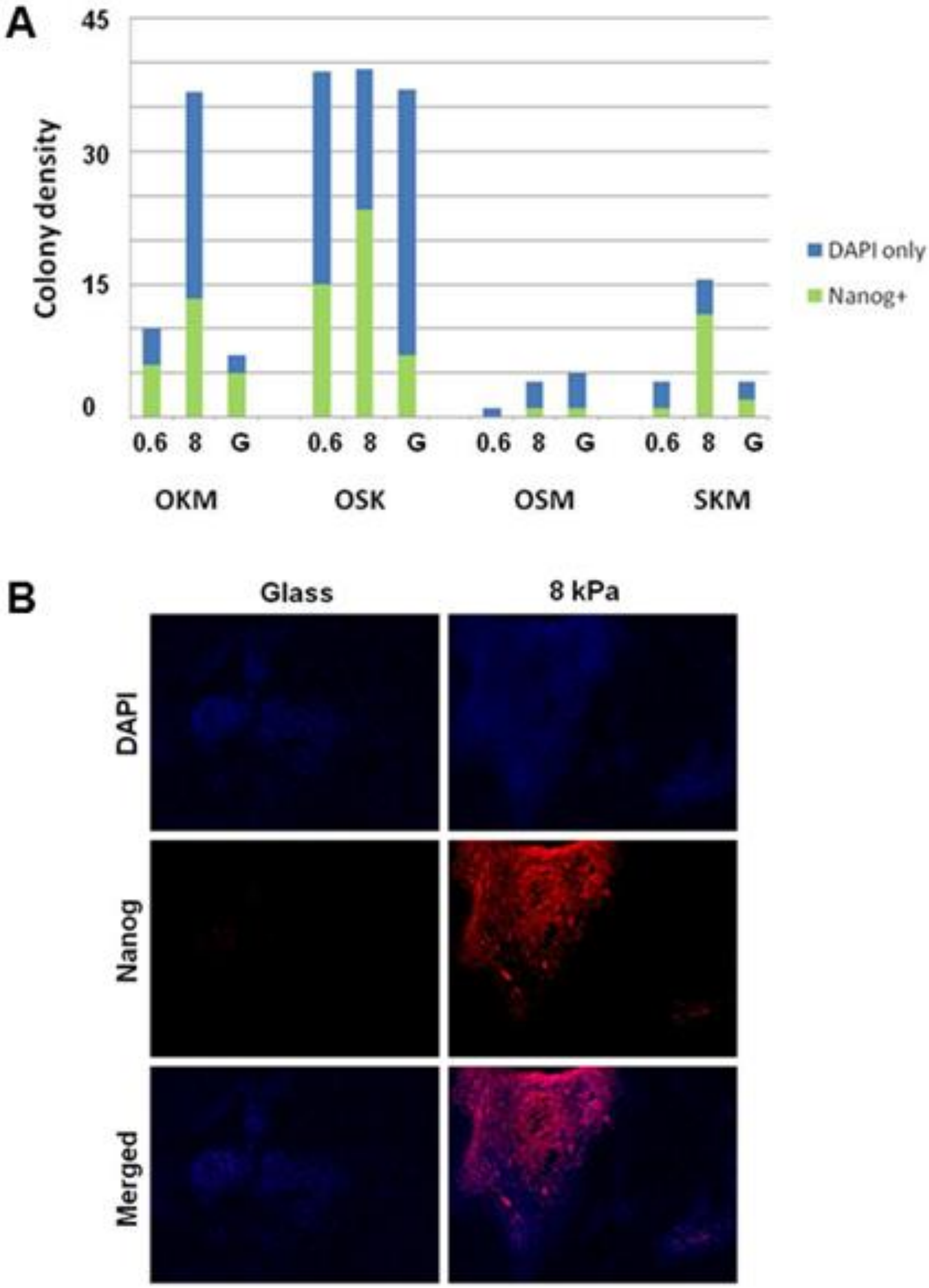

Figure 2.18. Effect of substrate stiffness of 3-factor reprogramming. a, Quantification of Nanog+ and Nanog- colony formation after 3-factor (OKM, OSK, OSM, andSKM) transduction across 3 stiffnesses (0.6 and 8 kPa and Glass~2 GPa). b, iPSC colony immunostaining morphology after SKM 3-factor transduction on different stiffnesses, after 11 days.

Our data shows that intermediate substrate rigidities may be better at replacing some of the most critical transcription factors (e.g., Oct4) during the reprogramming process (Figure 2.18). Interestingly, we also see a retention of stiffness mediated reprogramming in fibroblasts cultured on PA gels for only 5 days (before any apparent colony formation) prior to being passaged to MEFs. After being removed via trypsinization from PA gels, cells are then passaged at identical seeding densities and viabilities, and the effect of stiffness on reprogramming efficiency is retained.

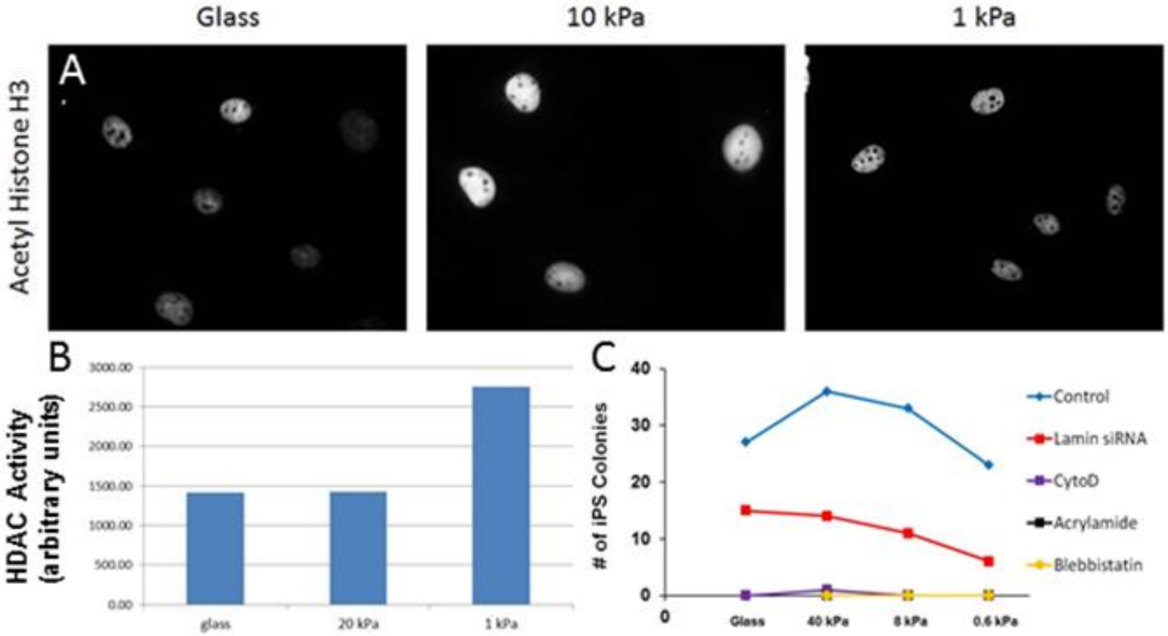

Figure 2.19. Characterization of substrate rigidity effect on reprogramming. a, AcH3 immunostaining respectively in MERFs seeded 24h on different substrate stiffness. b, HDAC activity of MERFs seeded 24h on different substrate stiffness. c, iPS colonies count with different cytoskeletal or nucleus matrix proteins knockdowned during iPS reprogramming.

Given our prior rationale and result on topography enhanced reprogramming, we first analyze the effect of substrate stiffness on the acetylation histone H3 and HDAC activity. In addition, we also sought to assess how substrate stiffness can affect reprogramming after disrupting the cytoskeleton and nuclear matrix proteins. From these studies we found that matrix rigidity modulates both AcH3 marks and HDAC activity in adult fibroblasts, where AcH3 is highest on intermediate rigidities and HDAC activity is increased on soft surfaces (Figure 2.19 a and b). After disruption of various cytoskeletal and nucleoskeletal elements (via drug inhibitors and RNA interference) we observe drastic modulation of stiffness mediated reprogramming trends (Figure 2.19c). Taken together, these data suggest that both the cytoskeleton and nucleoskeleton play a critical role in stiffness mediated reprogramming.

In any given physiological microenvironment, cells may experience a number of different biophysical inputs, which, as we show, might induce critical changes in epigenetic signature. Given the broad influence of epigenetics in cell behavior and phenotype determination, our results have interesting implications beyond this field. It will be useful to explore, for example, if these microtopography-induced changes in histone marks poise adult fibroblasts into a more unstable epigenetic state, allowing it to more readily transition into other phenotypes. Such evidence could greatly advance the field of cell biology by helping understand how mechanomodulated epigenetic changes alter cell behavior in cell-materials interactions, direct cell reprogramming into cardiomyocytes and neurons[46–51], tumor growth and metastasis, and adult stem/progenitor cell differentiation. This information is critical to the medical field as it presents new ways to maximize the potential of stem cell technologies, mitigate pathophysiological response in injured and diseased states, and greatly improve the design of next-generation biomaterials.

Chapter 3: Drug-Eluting Biomaterials for Spinal Cord Regeneration

3.1 Introduction

3.1.1 Pathophysiological Response to Spinal Cord Injury

Spinal cord repair remains one of the biggest challenges for regenerative medicine. Recent studies have found that spinal cord injury (SCI) is over five times more prevalent than previously estimated, bringing the total number of people living with SCI to over one million in the United States alone[52] . In addition, as palliative care continues to advance, this number will continue to rise.

Severe SCI is marked by a disruption in the ascending and descending axons of the spinal tracts. This disruption prevents vital communication between the brain and other parts of the body. Following injury, neural cells die – namely neurons and oligodendrocytes; molecules that are inhibitory to axon growth are secreted; and reactive astrocytes and infiltrating macrophages facilitate glial scar formation, leading to the physical and chemical impedance of axon growth[53–58]. These events are accompanied by active secondary degeneration of myelin tissues, causing additional losses in neural cell populations at or near the injury site[59,60]. Together, these events cause paralysis and prevent natural recovery. Considering this, a successful regenerative strategy might require a combination of therapies that have independently been shown to mitigate the previously mentioned pathophysiologies. Before such a strategy can become a reality, however, the efficacy and safety of each individual therapy must be ensured.

3.1.2 Boosting Local cAMP Levels for Spinal Cord Repair

Previous research has demonstrated the therapeutic utility of small molecule drugs such as rolipram in spinal cord repair[58,61]. With its anti-inflammatory[62,63] and cyclic adenosine monophosphate preserving properties, rolipram has been shown to promote regeneration of new axons[64,65], aid in the preservation of myelinated tissues[66], attenuate acute oligodendrocyte death[67,68], reduce reactive gliosis and subsequent glial scar formation[65], and significantly improve functional recovery[64,65,68,69] after SCI. However, more recent studies have presented data that leave the efficacy and safety of rolipram usage for spinal cord repair in question.

A study led by Sharp et. al. was unable to replicate the beneficial effects observed through the subcutaneous (s.c.) delivery of rolipram in combination with the transplantation of Schwann cells as previously reported by Pearse et. al[70]. A second report also found little added functional recovery from the systemic delivery of rolipram with the transplantation of a glial restricted precursor cell population[71]. Interestingly, the latter report also suggested that the s.c. delivery of rolipram could lead to adverse effects locally within the spinal cord (e.g., increased death of transplanted cells) as well as systemically (e.g., increased body-weight loss and micturition peak frequencies). While others have reported the importance of the local concentration of rolipram within the spinal cord[65], the conflict surrounding rolipram usage for spinal cord repair remains largely unresolved.

3.1.3 Enzymatic Digestion of the Glial Scar for Spinal Cord Repair

Studies lead by Bradbury et. al. have described the therapeutic potential of chondroitinase ABC (chABC) in spinal cord repair given its ability to degrade chondroitin sulfate proteoglycan (CSPG) glycosaminoglycan (GAG) chains. These CSPGs make up a large portion of the regeneration-inhibiting glial scar of the injured spinal cord and degradation of CSPG GAG side chains have been shown to promote the regeneration of axons into the injury site and yield a greater degree of functional recovery. The difficulty in using chABC as a therapeutic agent for spinal cord injury lies in its rapidly decaying enzymatic activity profile. Due to this limitation, researchers typically deliver chABC directly into the injury site via multiple intrathecal injections. These types of injections are less ideal for human treatments as they pose the threat of damaging existing or newly regenerated tissues within the delicate spinal cord.

3.1.4 Biomaterials for Spinal Cord Repair

With the above in mind, this work aims to develop a drug-delivery platform that 1) allows for diversity in deliverable drugs (i.e., small molecules and large enzymatic proteins), 2) is non-invasive to the delicate spinal cord tissues, and 3) is biodegradable to eliminate the need for device retrieval. Towards this goal we have developed drug-eluting microfibrous patches for spinal cord repair.

Several groups have utilized biodegradable scaffolds for many neural regeneration strategies[23,72–79]. Previously we have explored the use of natural materials[80] and synthetic scaffolds with and without drug-delivery for spinal cord regeneration[81,82]. Electrospun nanofibrous patches, with rolipram immobilized to the surface via hydrophobic adsorption, showed anatomical as well as functional improvements after a T9-T11 level SCI. The direct combination of rolipram with the fibrous topography of patches was shown to increase axon growth through the membrane and in the lesion, promote angiogenesis through the membrane, and decrease the population of astrocytes and chondroitin sulfate proteoglycans at the lesion[81]. However, with only the adsorption of rolipram onto fibrous patches via hydrophobic interactions, very little control over drug loading and subsequent release-kinetics was achieved. A new platform with greater control over the local delivery of small molecule drugs and enzymatically stable proteins into the spinal cord would greatly assist in better understanding the effects of both rolipram and chABC dosage in spinal cord repair, ultimately allowing for the development of more robust therapeutic strategies.

3.2 Materials and Methods

3.2.1 Drug-Eluting Microfibrous Patch Fabrication and Characterization

The assembly of drug-eluting microfibrous patches began with the fabrication of biodegradable microfibrous membranes. Electrospinning technology was employed for this purpose as previously described[23,83]. Briefly, a polymer solution composed of 19% (w/v) poly(L-lactide), M.W. 85,000 – 160,000 (PLLA, Sigma) dissolved in 1-1-1,3-3-3 hexafluoro-2-propanol (Matrix Scientific) was jetted from an electrically charged (12 kV) single-needle spinneret and collected onto a grounded rotating mandrel (800 RPM; 10 cm diameter). The electrospinning distance was fixed at 7 cm. Once formed, membranes where submerged in water at 65ºC and mechanically stretched to further induce fiber alignment. For decontamination, membranes were submerged in 75% ethanol for 30 minutes and thoroughly washed in sterile PBS.

PRONOVA™ Ultrapure LVM sodium alginate (NovaMatrix™; FMC BioPolymer) was used to form a thin hydrogel layer on top of microfibrous membranes. This hydrogel layer was used as a drug excipient for the local delivery of rolipram into the spinal cord. Removable polystyrene chamber gaskets were modified from Lab-Tek™ II Chamber Slide™ Systems (Thermo Scientific). Chamber gaskets were placed on top of microfibrous membranes and secured, creating a 2 cm by 2 cm well for hydrogel placement (Figure 3.1a). Five-hundred microliters of a 2% (w/v) sodium alginate solution, dissolved in deionized (d.i.) water, was added to chamber wells and layered over each membrane surface. In order to obtain a flat and homogenously polymerized hydrogel, this sodium alginate layer was crosslinked using a calcium chloride-rich mist. Mist was produced via ultrasonic vibrations generated by a Nutramist™ 3-head fog module (FutureGarden™). Following crosslinking, newly formed alginate hydrogels were air-dried onto microfibrous membrane surfaces at 37°C overnight and chamber gaskets were removed. This process helped to slow the elution of loaded drugs during rehydration[84] as well as reduce patch thickness for implantation. The microscale structure of drug-eluting microfibrous patches was resolved under high-powered scanning electron microscopy (SEM). Microfiber diameter typically ranged from 500 nm to 1 μm; however, fiber diameters up to 2 μm were occasionally observed.

Drug-eluting microfibrous patches were loaded with variable concentrations of rolipram. To do so, rolipram was first dissolved in DMSO (0.1 mg/μl) and then added to a larger volume of d.i. water. An equal volume of 4% sodium alginate was then added to rolipram solutions, bringing the final sodium alginate concentration to 2%. Final concentrations of rolipram were 25 (low-dose) and 500 (high-dose) μg/ml. The final amounts of DMSO within hydrogels were $\leq 0.5\%$ (vol/vol). To minimize the risk of contamination, patches were fabricated under sterile conditions in a laminar airflow hood. In addition, all materials and devices used were decontaminated with 70% ethanol and solutions were sterile-filtered through a 0.2 μm filter prior to use.

To obtain the release profiles of rolipram, drug-eluting microfibrous patches were made by using either 100 or 500 µl of rolipram-loaded sodium alginate. After fabrication, patches were submerged in 0.5 ml of PBS and incubated at 37°C for up to 14 days. At selected time points (18 hours; 1.5, 3, 7, and 14 days) solution was withdrawn and the amount of rolipram in the withdrawn solution was determined via HPLC. From this information the total amount of released rolipram was calculated and release profiles were generated.

3.2.2 Cervical Spinal Cord Hemisection and Subdural Patch Implantation

All experimental procedures with animals were approved by the ACUC committee at UC Berkeley and were carried out according to the institutional guidelines. All efforts were made to minimize the number of animals used and their suffering. Adult female athymic rats (National Cancer Institute) weighing 170-243 g were used in all experiments. Four experimental groups were included: hemisection injury with (1) no patch or treatment (untreated), (2) empty drug-eluting microfibrous patch treatment (blank patch), (3) low-dose rolipram patch treatment (low-dose rolipram), and (4) high-dose rolipram patch treatment (high-dose rolipram).

Drug-eluting microfibrous patches were implanted subdurally for the direct delivery of rolipram to the spinal cord. Laminectomies were performed on the fourth through sixth cervical vertebrae, exposing the spinal cord at the desired lesion site. The dura was opened with a single longitudinal incision approximately 0.5 cm in length. A fine scalpel blade was used to create spinal cord hemisection lesions moving outward starting from the midline. This lesion only caused damaged on the right side of the spinal cord. Each injury was inspected to ensure the complete severance of spinal cord tissues above and below the lesion site. Additional damage to the dura was avoided. Before implantation, patches were trimmed down to an appropriate size (0.5 cm by 0.3 cm). Patches were then carefully implanted underneath the dura, insuring that the hydrogel layer faced medially toward the injury site. The dura was then sutured closed over implanted patches using 9-0 sutures. Untreated animals received no additional therapy and the dura was closed immediately after hemisection. In all cases, the surgery site was closed in multiple layers.

3.2.3 Forelimb Motor Assessment

In order to assess the degree of animal functional motor recovery after cervical SCI we utilized the open-field forelimb recovery rating scale as previously described[85,86]. Briefly, at various time points post injury (2 day; 1, 2, 3, 4, 6, and 8 weeks) animals were placed in a circular foam-enclosed arena (100 cm diameter, 40 cm wall height) and scored. Scoring was separated into six major categories: articular movement of the shoulder (2), elbow (2), and wrist (2); stationary (2) and active (2) weight support; digit position (2); stepping (6); forelimb-hindlimb coordination (3); and tail position (1); (note: parenthesis denotes point totals for each category). Scores were summed to obtain an overall Martinez forelimb score (20 points max). All rats were scored over a 4 minute time window, and all scorers were blind to the animals' experimental group. Open-field sessions were video recorded for score accuracy confirmation.

3.2.4 Histopathology and Immunohistochemistry

Eight weeks after spinal cord hemisections, animals were sacrificed and immediately perfused with 4% paraformaldedyde (PFA). The C2-C7 segment of rat spinal cords were explanted and kept in 4% PFA at 4oC for 24 hours and later cryoprotected in 30% sucrose in PBS. Cross sections of the spinal cord, through the lesion site, were cryosectioned (10 µm in thickness) for H&E (hematoxylin and eosin) staining and immunostaining. Spinal cord cross sections were immunostained for the following: neurofilament (NFM, rabbit polyclonal antibody, Sigma-Aldrich) to identify axons, myelin basic protein (MBP, rabbit polyclonal antibody, Sigma-Aldrich) for oligodendrocyte myelin, and glial fibrillary acidic protein (GFAP, rabbit polyclonal antibody, Millipore) for reactive astrocytes. For chondroitin sulfate proteoglycan (CSPG, mouse monoclonal antibody, Sigma-Aldrich) identification, slides were kept in 10 mM sodium citrate buffer (pH 6.0) at 95-99°C for 10 minutes for antigen retrieval before the immunostaining procedure was performed. For fluorescence signal intensity quantification, multiple images within the lesion sites of animals from each group were captured and a threshold of intensity was defined to identify proteins of interest. ImageJ software was then used to calculate the average total pixels per image for NFM, MBP, GFPA and CSPG marker expression.

All data are presented as mean ± standard deviation. Data from behavioral scores, where time and treatment vary, were analyzed using a two-way analysis of variance (ANOVA) with repeated measures. Differences between groups were determined using Tukey's post-hoc test. A one-way ANOVA was used to analyze in vitro release profiles and average total pixel quantifications. Survival data were analyzed using a log-rank (Mantel-Cox) test where the survival curve of each treatment group was compared to that of untreated animals. Linear regression analysis was performed on animal weight loss over time to determine if slopes varied significantly from zero. For all cases, p-values less than 0.05 were considered statistically significant. GraphPad Prism® 5.0 software was used for all statistical evaluations.

3.3 Results and Discussion

3.3.1 Structure and Apperance of Drug-Eluting Microfibrous Patches

We used electrospinning technology to produce biodegradable PLLA microfibrous membranes. Membranes were mechanically stretched to induce fiber alignment. After membranes were fabricated, a thin alginate hydrogel layer was formed on top. SEM revealed the intimate juxtaposition of the highly aligned microfibrous membrane and thin alginate hydrogel layer (Figure 3.1b) – with fibers extending outward with respect to the plane of the captured image. Fluorescence microscopy confirmed the ability of drug-eluting microfibrous patches to encapsulate small fluorescent molecules (4',6-diamidino-2-phenylindole, DAPI) within their thin hydrogel layer (Figure 3.1c). Membrane thickness ranged from 50 – 100 μm and the dried alginate hydrogel layer typically added an additional 5.3 μm in thickness. After rehydration, hydrogel thickness was approximately 20 μm.

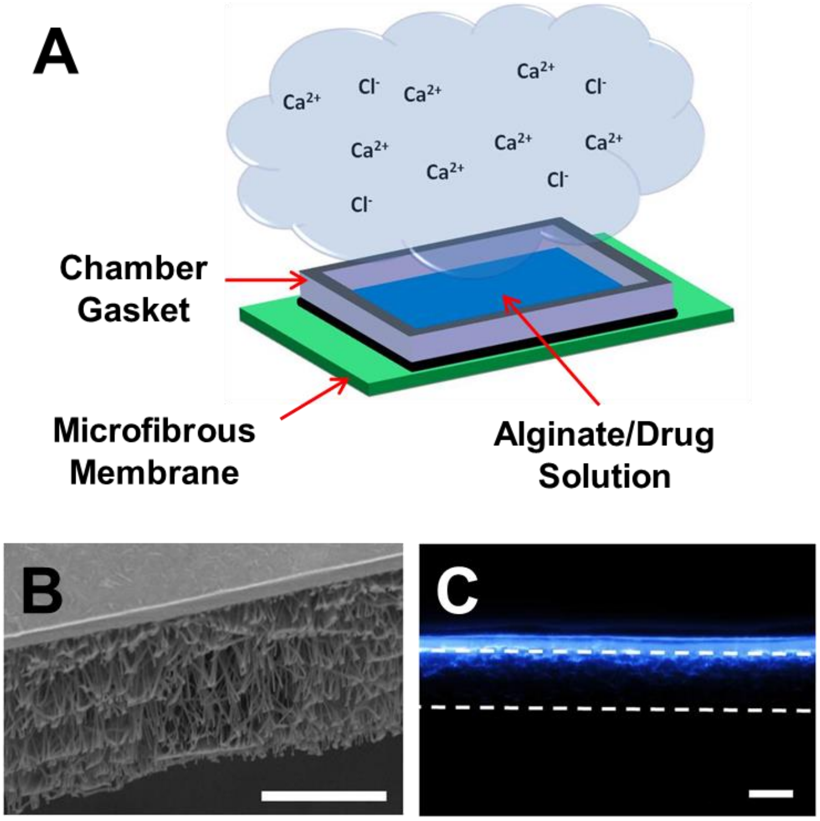

Figure 3.1. Assembly and structure of drug-eluting microfibrous patches. a, A schematic illustrating the assembly of drug-eluting microfibrous patches. Chamber gasket is used to create a well for sodium alginate solution (loaded with drug or empty) placement over top of PLLA microfibrous membranes. In addition, a novel calcium chloride-rich mist

crosslinking mechanism is demonstrated. SEM image reveals (b) the structure of microfibrous membrane and alginate layers within drug-eluting microfibrous patches. c, Fluorescent micrograph of patch cross-section shows the incorporation of small fluorescent molecules (DAPI) into the alginate layer. Dashed lines indicate microfibrous membrane boundaries. Scale bars = 50 μm.

3.3.2 Release Profile and Ezymatic Activity

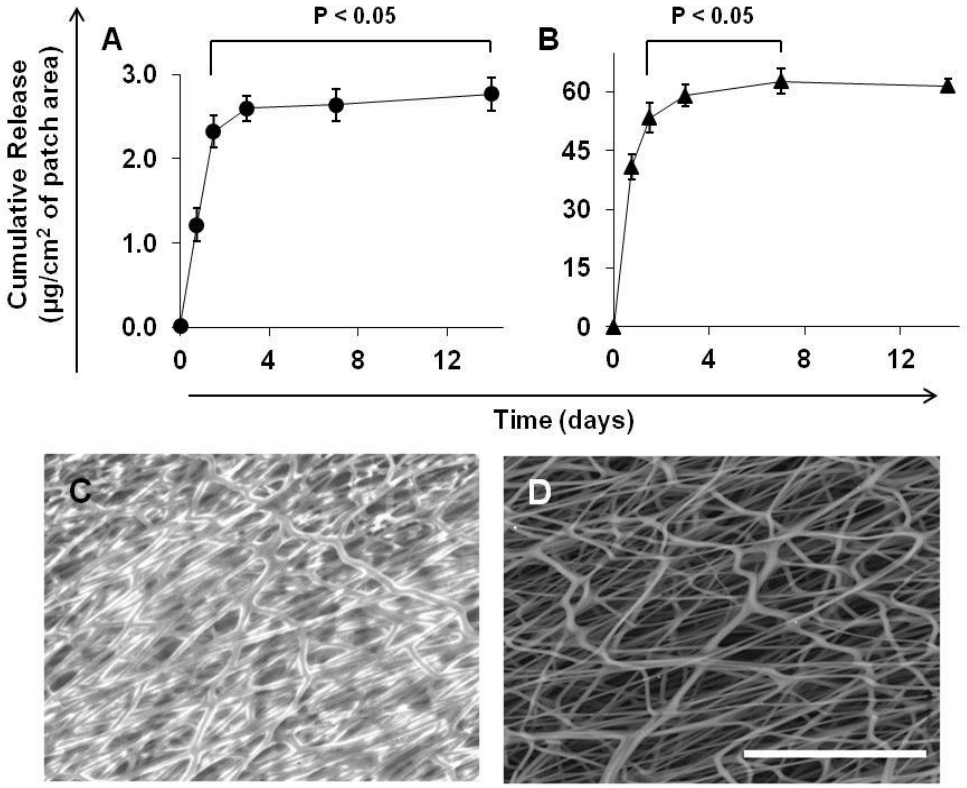

Figure 3.2. Low and high-dose rolipram in vitro release profiles. Cumulative release profiles of low (a) and high-dose (b) rolipram patches at 37°C in PBS. Statistical analysis shows a significant amount of rolipram was released beyond 1.5 days for both cases. SEM image reveals (d) residual alginate hydrogel on microfibrous membrane surface after 12 days at 37°C in PBS. (d) SEM image of bare microfibrous membrane surface for comparison. Scale bar = 50 μm.

Drug-eluting microfibrous patches were loaded with low-dose or high-dose concentrations of rolipram (3.1 and 62.5 μg/cm2, respectively) and the subsequent in vitro release profiles were observed (Figure 3.2a,b). The low-dose concentration of rolipram (in amount per unit area) was consistent with our previous SCI study where rolipram-loaded patches significantly enhanced spinal cord regeneration[81]. The high-dose concentration was chosen as an upper limit for drug loading capacity as to not compromise alginate's gelation properties. As expected, high-dose rolipram patches delivered approximately 20 fold more drug than low-dose rolipram patches. It is important to note that nearly 10% of loaded rolipram remained unreleased in low-dose rolipram patches after 14 days, leaving the possibility of additional drug release. Release profiles showed drug-eluting microfibrous patches were capable of maintaining a significant release of rolipram beyond 1.5 days over a wide range of loading concentrations. Furthermore, low-dose rolipram patches exhibited an 18-hour burst release of 38.7% while high-dose rolipram patches showed a burst release of 65.6%. Both conditions demonstrated significant improvements over our previous drug-delivery platform which, through the passive adsorption of rolipram, displayed a 4-hour burst release of over 90%[81]. It is also worth noting that patches retained residual amounts of their hydrogel layer after 12 days at 37°C in PBS. SEM reveals the structure of this residual hydrogel layer relative to the membrane's bare surface (Figure 3.2c,d, respectively).

3.3.3 Effect of Local Drug Concentrations on Forelimb Recovery

To assess the therapeutic utility of drug-eluting microfibrous patches for the study and repair of SCI, rats were subjected to a C5 hemisection lesion. Immediately after injury, animals were either left untreated or given one of three drug-eluting microfibrous patches: a blank patch; a low-dose rolipram patch, or a high-dose rolipram patch. Figure 3.3 illustrates the implantation of patches post SCI.

In general, animals treated with empty patches experienced modest improvement over untreated animals. When animals were treated with low-dose rolipram patches we observed drastic improvements in functional outcomes. Specifically, Martinez forelimb open-field scores showed that animals treated with low-dose rolipram patches (n=3) score significantly higher, from weeks 1 through 4, 6 and 8, when compared to all other animals (Figure 3.4a). In contrast, animals treated with patches loaded with 20 times more rolipram (high-dose rolipram; n=4) showed no significant differences with respect to untreated animals (n=4). Statistical significance of open-field score differences was assessed using a two-way ANOVA.

Articular movement scores show early motor improvements for low-dose rolipram-treated animals. During the first week of this study, these animals displayed significantly more range-of-motion in forelimb joints (e.g., shoulder, elbow, and wrist). Figure 3.4b shows animal forelimb articular movement scores at 2 day and 1 week time points. After 1 week, low-dose rolipram-treated animals scored significantly higher than all other groups. No other scores were significantly different.

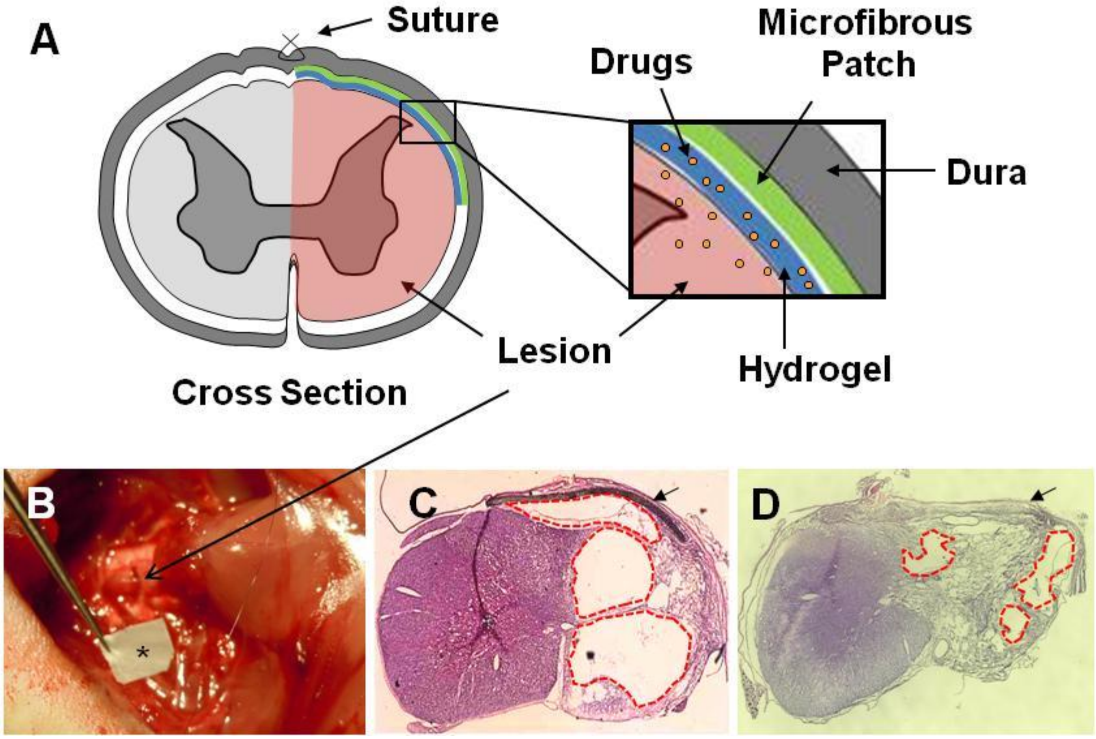

Figure 3.3. Implantation of drug-eluting microfibrous patches after SCI. a, Schematic of subdural implantation of drug-eluting microfibrous patches into the injured cord. b, Macroscopic view of lesion site and patch during animal surgery. An asterisk was used to mark location of drug-eluting microfibrous patch. c, d, Gross histology of spinal cord cross section 8 weeks post SCI. H&E staining reveals new tissue formation at the lesion site and patch's ability to integrate into the surrounding tissues (d). c, Less regenerated control for comparison. Here, arrows point to the implantation site for drug-eluting microfibrous patches. Red dashes outline areas of less tissue formation for comparison.

During week 8 of this study, animal forelimb-hindlimb coordination frequencies were observed (Figure 3.4c). Sixty-seven and thirty-three percent of rats treated with low-dose rolipram patches experienced “consistent” and “frequent” coordination behaviors, respectively. Animals in other groups experienced no consistent coordination at all. Twenty-five percent of rats treated with empty patches (n=4) showed frequent coordination and another 50% showed “occasional” coordination, leaving 25% with no coordination. Untreated animals remained mostly (75%) uncoordinated. Animals treated with high-dose rolipram-loaded patches showed no coordination whatsoever.

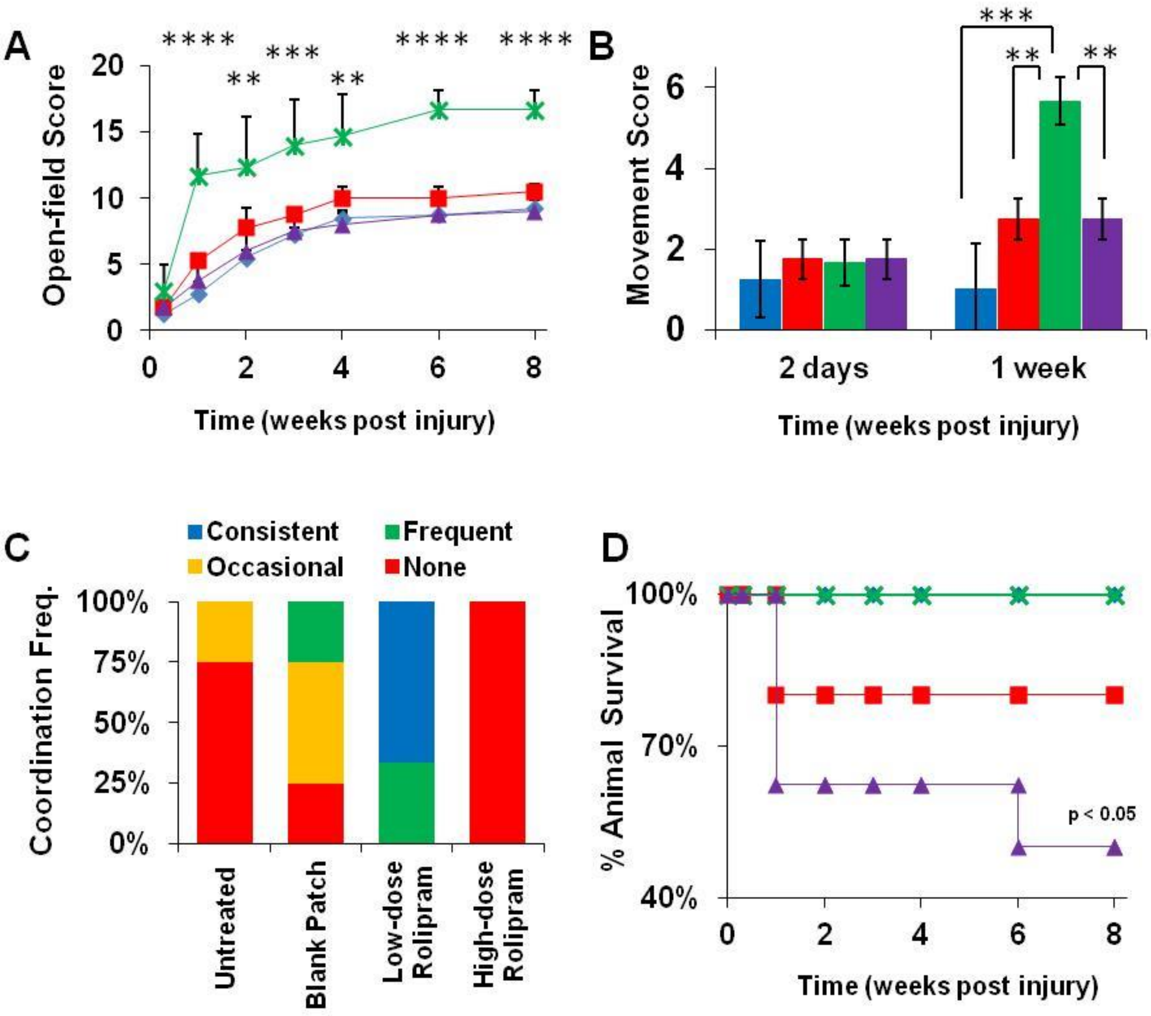

Figure 3.4. Functional recovery of forelimb locomotion based on the Martinez recovery scale and animal survival. (a, b, d) Scoring was performed across four groups: untreated (blue, -♦-), blank patch (red, -■-), low-dose rolipram patch (green, -X-), and high-dose rolipram patch (purple, -▲-). a, Overall Martinez open-field scores from weeks 1 through 4, 6 and 8. Asterisks indicate where low-dose rolipram scores were significantly greater than all other animals (****, ***, and ** denote where $p < 0.0001$, 0.001, and 0.01, respectively). b, Forelimb articular movement scores at 2 days and 1 week post SCI (*** and ** denote where $p < 0.001$ and 0.01, respectively). c, Animal forelimb-hindlimb coordination frequency at 8 weeks post SCI. d, Animal survival over the course of 8 weeks following the initial SCI. A log-rank (Mantel-Cox) test was used to determine significance.

At the completion of this study we reviewed animal survival data in an effort to assess overall animal health (Figure 3.4d). Upon the recommendation of unbiased veterinary experts, animals were sacrificed for various health-related reasons. These included excessive weight-loss, self-mutilation, and poor general health. For untreated animals and animals treated with blank and low-dose rolipram patches, animal survival rates ranged from 80-100%. Animals treated with high-dose rolipram patches showed a drastic drop off in survival rate (50%). Statistical analysis reveals that this survival curve is significantly ($p<0.05$) different than that of untreated animals. Although most animal deaths were sacrificial, one animal within the high-dose rolipram group was found deceased in its cage at week 6. There were no other cases where animal death was observed beyond the first week. To confirm this apparent increase in toxicity, we performed an analysis on animal weight loss over days 3 through 6 after SCI (Figure 3.5). From this analysis, we confirmed that high-dose treated animals continued to experience significantly ($p<0.05$) more weight loss within the first week.

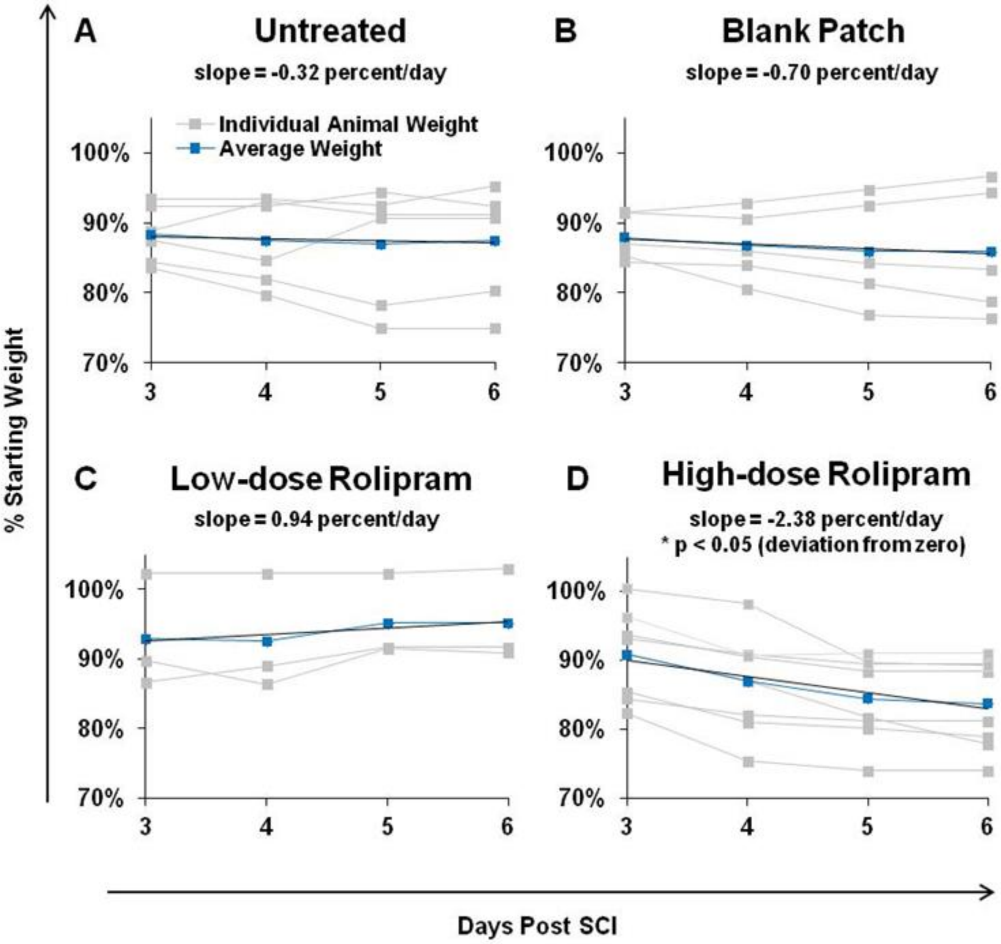

Figure 3.5. Analysis on animal weight loss over days 3 through 6 after SCI. From this analysis, we confirmed that high-dose rolipram-treated animals experience weight loss at a ignificantly ($p<0.05$) higher rate than all other animals in the first week post SCI

3.3.4 Gross Histopathology and Anatomical Improvement

Eight weeks after initial injuries, rats were sacrificed and immunohistological analyses were performed on spinal cord tissues and patches. Spinal cord sections from each experimental group were stained for NFM (Figure 3.6 a-d), MBP (e-h), GFAP (Figure 3.7 a-d), and CSPG (e-h). Figures 3.6 and 3.7 illustrate the representative trends observed across all stains. In general, animals treated with blank patches commonly showed slightly more axon outgrowth (indicated with NFM immunostaining) into the lesion site when compared to untreated animals. Furthermore, animals treated with low-dose rolipram patches exhibited the greatest degree of axon outgrowth into the lesion site when compared to all other groups. Animals treated with high-dose rolipram patches showed a drastic decrease in the number of axons present when compared to low-dose rolipram and blank patch treated animals.

A similar trend was observed regarding the presence of oligodendrocyte cell (MBP+) populations within the injury site after low-dose rolipram delivery. Specifically, immunostained sections for animals treated with low-dose rolipram patches showed a drastic increase in the number of MBP+ cells with respect to all other groups (Figure 3.6 e-h), suggesting the enhancement of myelin formation and/or sparing of oligodendrocytes. Figure 3.6 i and j attempt to quantitatively represent the degree of anatomical recovery seen in axon outgrowth and oligodendrocyte myelin, respectively.

As expected, animals left untreated showed a substantial number of reactive astrocytes present within their lesion sites (Figure 3.7 a). The application of any type of patch seemed to reduce the number of astrocytes seen at the lesion (Figure 3.7 b-d). While high-dose treatment produced a significant decrease in the number of astrocytes present, low-dose treatment resulted in the most dramatic decrease (Figure 3.7 i). After analyzing extracellular matrix components within cord lesions we found that animals treated with low-dose rolipram patches had no significant change in CSPG content at their lesion site relative to animals from untreated and blank patch groups (Figure 3.7 e-g). Interestingly, animals treated with high-dose rolipram patches showed a dramatically higher CSPG content (Figure 3.7 h) within their lesions compared to low-dose treated and untreated animals (Figure 3.7 j).

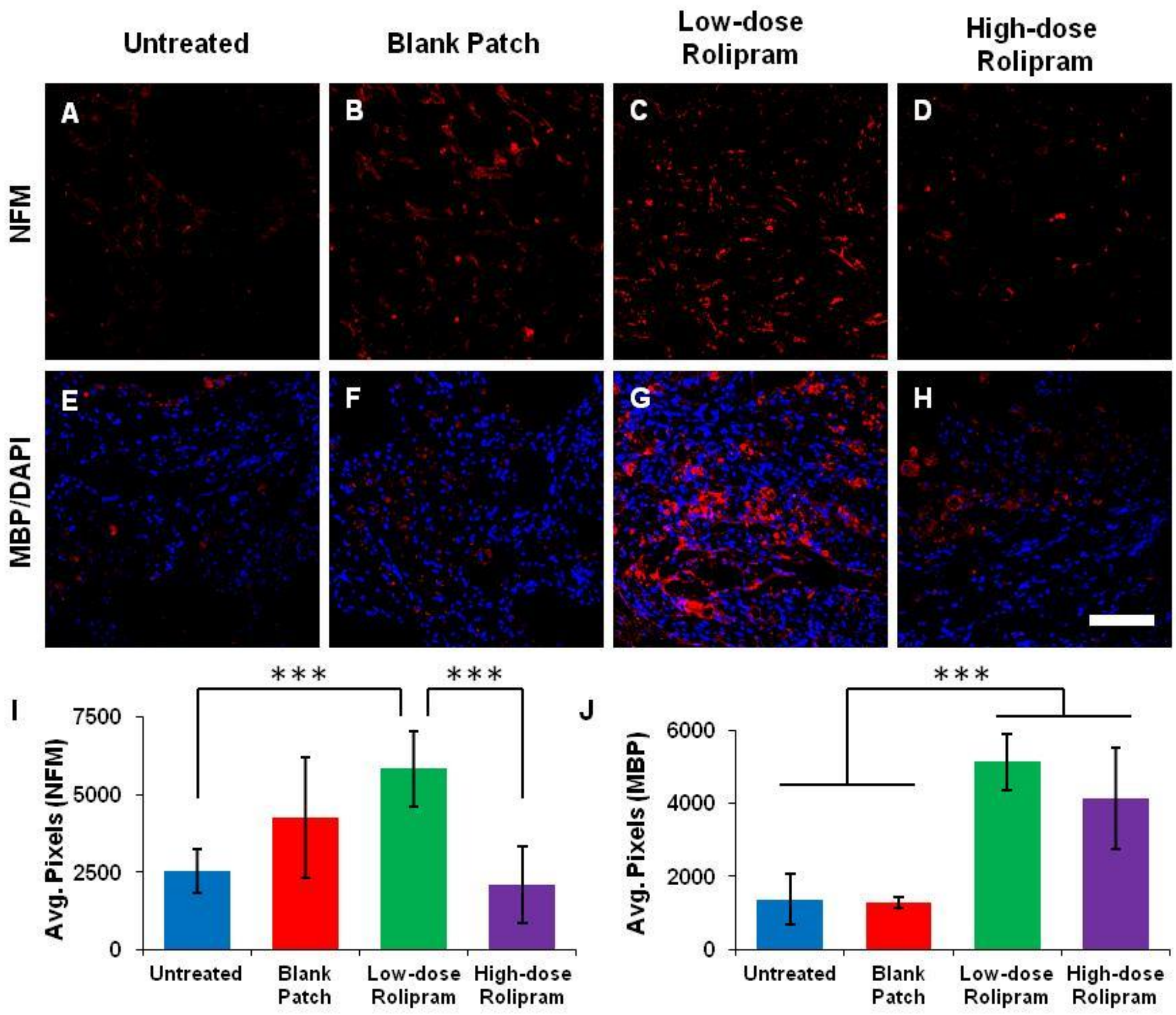

Figure 3.6. Histological analysis of NFM and MBP staining at 8 weeks post SCI. Representative immunofluorescent staining of tissue regeneration within the lesion site of spinal cord cross sections in untreated animals (a, e), blank patch treated animals (b, f), low-dose rolipram-treated animals (c, g), and high-dose rolipram-treated animals (d, h). Axons in the lesion were identified using NFM antibodies (a-d). Oligodendrocyte myelin was identified using MBP antibodies (e- h). DAPI staining was used to identify cell nuclei. Scale bar = 100 µm. (i, j) ImageJ software was used to quantify the average total pixels for NFM+ axons or MBP+ oligodendrocytes, respectively, within immunostained sections.

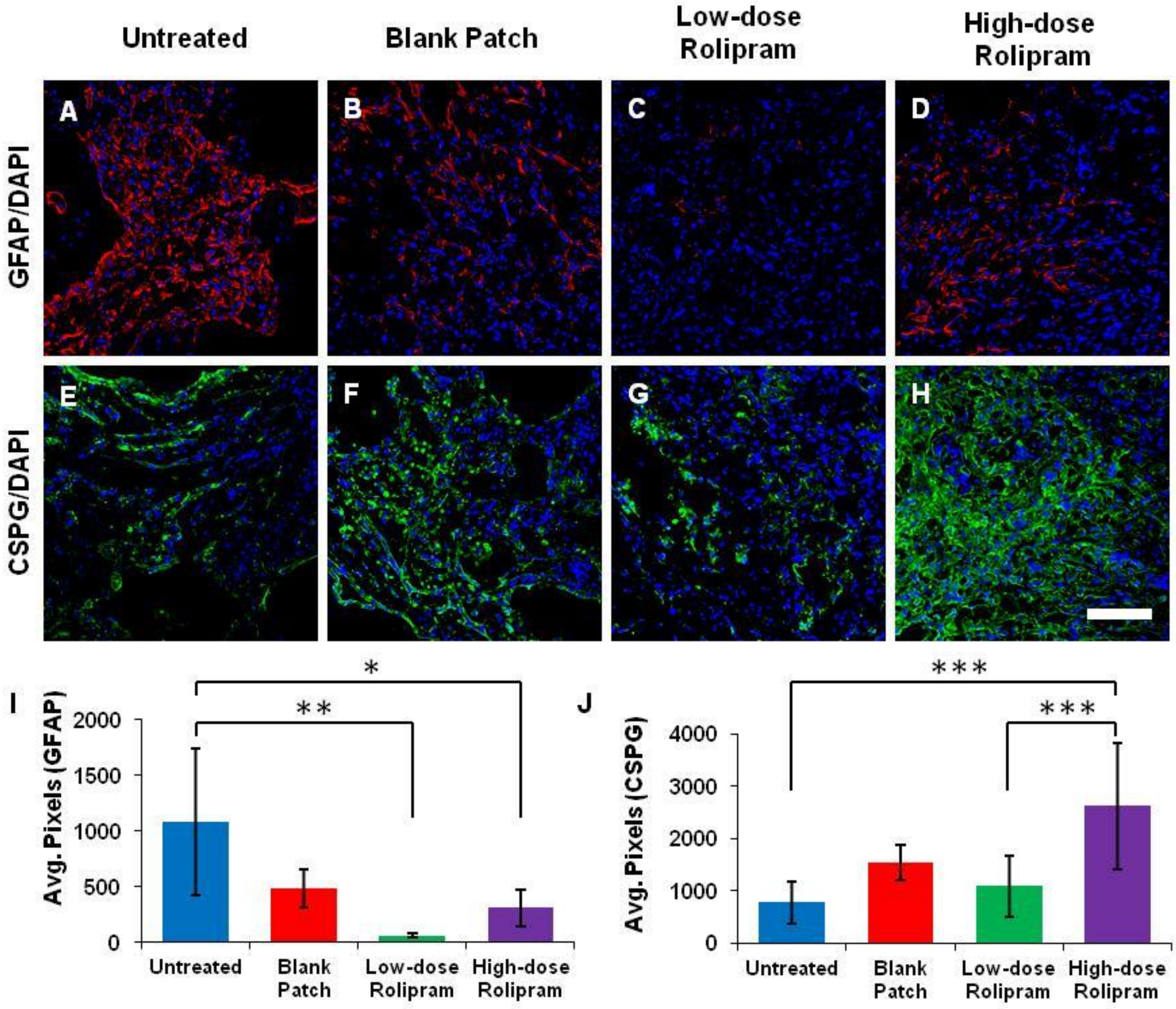

Figure 3.7. Histological analysis of GFAP and CSPG staining at 8 weeks post SCI. Representative immunofluorescent staining of tissue regeneration within the lesion site of spinal cord cross sections in untreated animals (a, e), blank patch treated animals (b, f), low-dose rolipram-treated animals (c, g), and high-dose rolipram-treated animals (d, h). Astrocytes in the lesion were identified by GFAP antibody staining (a-d). Glial scar formation was identified using CSPG antibodies (e-h). DAPI staining was used to identify cell nuclei. Scale bar = 100 μm. (i, j) ImageJ software was used to quantify the average total pixels for GFAP+ cells or the presence of CSPG within the lesion site extracellular environment.

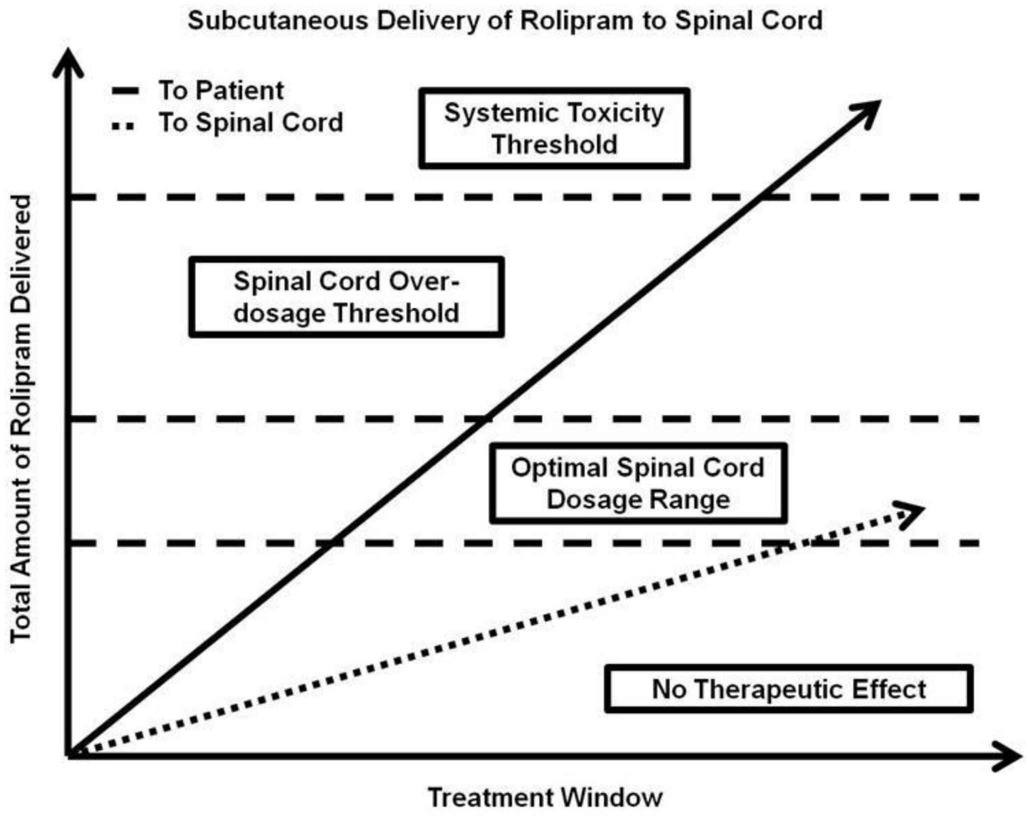

Figure 3.8. A schematic illustrating the complex balance involved in the s.c. delivery of rolipram to the injured spinal cord for repair. Because only a fraction of the total amount of rolipram delivered s.c. to the patient will reach the spinal cord, systemic rolipram concentrations reach unnecessarily high levels, increasing toxicity related risks. In addition, injury-to-injury and/or patient-to-patient variations can cause uncertainty in the local concentration of rolipram within the spinal cord. As we have shown, inappropriate local concentrations of rolipram within the spinal cord can be detrimental to regeneration. Much of the uncertainty in local spinal cord and systemic rolipram concentrations can be removed with the local delivery of rolipram via drug-eluting microfibrous patches.

Many studies have outlined the beneficial role that rolipram can have in spinal cord repair. However, recent studies suggest that its s.c. delivery may lead to systemic toxicity and less robust functional recovery[70,71]. Figure 3.8 attempts to illustrate the concerns and potential pitfalls that may complicate the usage of rolipram through s.c. injections for spinal cord repair. Achieving an optimal concentration of rolipram within the spinal cord requires a complicated balance of minimizing systemic toxicity, avoiding spinal cord over-dosage, and appropriately accounting for patient/injury variations. Furthermore, the co-delivery of other therapeutic agents (i.e., transplanted cells) may further convolute this balance[87]. Conceptually, this may help to explain conflicting results found by previous studies. For example, while Pearse et al.[64] demonstrated significant spinal cord recovery after systemic delivery of rolipram, they also reported that "rats treated with rolipram showed increased secretion of porphyrin from the eyes" indicating that some degree of toxicity was reached. Under nearly identical experimental conditions, Sharp et al.[70] found that rolipram offered no additional recovery over untreated animals. Using similar experimental conditions, Nout et al.[71] showed that systemic delivery of rolipram offered little functional recovery over untreated animals and resulted in significant reductions in animal health. Interestingly, Nikulina et al.[65] found that rolipram offered improvements in recovery when delivered at a rate approximately 10 times greater than the previously mentioned studies. Even more, there was evidence that even higher dosages can yield local toxicity within the injured cord (e.g., less regeneration). This study was, however, done using a different injury model (e.g., hemisection versus contusion) and different rat strains and, therefore, may be difficult to compare. Given these conflicting results and the fact that the local rolipram concentration within the spinal cord is often unknown or unreported, we are unable to definitively determine specific systemic dosages that are therapeutic versus toxic. Still, these results, considered together, highlight the variability that s.c. delivery of rolipram brings to spinal cord repair.

In an effort to avoid the complications observed with the s.c. delivery of rolipram, we attempted to create a new and improved platform that would allow for controlled, local drug-delivery into the spinal cord. With the incorporation of an alginate hydrogel layer as a drug excipient, drug-eluting microfibrous patches successfully demonstrated their ability to 1) suppress the extent of burst release previously seen with our small molecule drug-delivery devices and 2) sustainably deliver rolipram beyond 1.5 days in vitro over a large range of drug loading concentrations. Several studies demonstrate rolipram's efficacy even when delivered acutely (3 days or less)[69,88,89]. Given this, we felt our patches were suitable for in vivo experimentation. While our previous spinal cord patch fabrication utilized blends of PLLA and poly(D,L-lactide-co-glycolide) (PLGA), here patches were composed of only PLLA polymer to reduce the potential influence of acidic polymer contaminants due to the rapid degradation of PLGA.

Consistent with our previous result[81], drug-eluting microfibrous patches loaded with a low-dose (3.1 – 3.9 μg/cm2) concentration of rolipram facilitated the greatest degree of animal functional and anatomical recovery. In particular, improvements in overall forelimb recovery as well as early forelimb joint movement were greater for animals treated with a low dosage of rolipram. Anatomical improvements included increases in the number of both axons and oligodendrocytes seen within the lesion site. In addition, a decrease in the number of reactive astrocytes and the amount of CSPG molecules present were observed. For most outcomes, patches loaded with a high-dose concentration of rolipram appeared to have little variation from the no treatment case. Interestingly, CSPG content within lesions, however, was much higher for animals treated with a high dosage of rolipram. In addition, high-dose rolipram-treated animals also displayed the lowest survival rate over the course of eight weeks suggesting that higher local rolipram dosages could subsequently lead to higher levels of rolipram in the spinal cord and/or body, which could ultimately prove detrimental to the overall health[90,91]. Patches without rolipram proved only slightly advantageous when compared to the no treatment case, thus demonstrating the need to incorporate additional therapeutic agents.

With respect to previous studies, these results suggest that by delivering a low dosage of rolipram directly into the spinal cord, we are able to achieve comparable outcomes with less than 1% of total rolipram delivered (over the course of 3 days). Interestingly, we've also shown that a higher dosage of rolipram directly into the spinal cord (still less than 1% of previous studies), may cause some local toxicity (less recovery within spinal cord) as well as systemic toxicity (increased animal death and weight loss). Because the total amount of rolipram delivered to animals is dramatically less than previous studies, we posit that the apparent variations in outcomes after systemic delivery of rolipram (e.g., via osmotic mini-pumps implanted s.c.) may be due to variations in the amount of drug that enters into the CNS through the blood-brain barrier and injury site.

It is important to note that unlike other rolipram related SCI studies, our model utilizes athymic animals. Several other SCI studies have used similar models to help promote the acceptance of xenogenic donor cells after transplantation. Because many of our previous and future studies aim to understand the combined effects of drug-delivery, fibrous scaffolds, and human stem cell transplantation on neural regeneration, an athymic animal model was chosen for clear comparison. This study suggests that drug-eluting microfibrous patches, through a local drug-delivery approach, have the ability to more clearly distinguish optimal and sub-optimal drug dosages for spinal cord repair. In order to further improve recovery and to more thoroughly study the effects of combination therapies on spinal cord repair, future studies will aim to explore the combined delivery of rolipram with other therapeutic agents (i.e., other drugs and/or cells) in addition to creating a more bioactive, cell adhesive hydrogel layer. Release-kinetics will be further improved through additional modifications aimed to enhance hydrogel stability on microfibrous membranes - through the use of various crosslinkers[84] and functional chemistry - thus, preventing rapid hydrogel erosion and delamination.

This study demonstrates the potential of drug-eluting microfibrous patches as a drug-delivery platform for the local release of rolipram into the injured spinal cord. Here we distinguish the therapeutic outcomes observed from the subdural implantation of patches loaded with low and high doses of rolipram. Patches loaded with lower concentrations yielded significant improvements in functional and anatomical recovery. With increasing loading concentration both functional and anatomical improvements diminished and overall animal health worsened. In all, this study demonstrates the therapeutic utility of drug-eluting microfibrous patches in the study and repair of SCI.

In addition, as we examine the functional recovery of animals treated with variable concentrations of chABC we see a similar dependence on drug loading concentration. Figure 3.9 illustrates these differences in functional recovery. Specifically, animals treated with 1X chABC loaded-patches had more forelimb movement at one week, higher occurrences of coordination in the 8th week, and higher overall Martinez forelimb scores than other groups (untreated, scaffold/patch alone, and 2X chABC loaded patches). Although glial scaring has been shown to prevent the regeneration of axons in the injured spinal cord, many scientists postulate that “some” glial scar formation is necessary in order to reestablish the compromised blood-brain barrier following SCI. In this case one would presume that there is a point when CSPG digestion (via delivery of chABC) could yield adverse results. Still, few studies have demonstrated this concept. The implications of chABC delivery rate dependent recovery is very exciting and future studies will look to explore this in more detail.

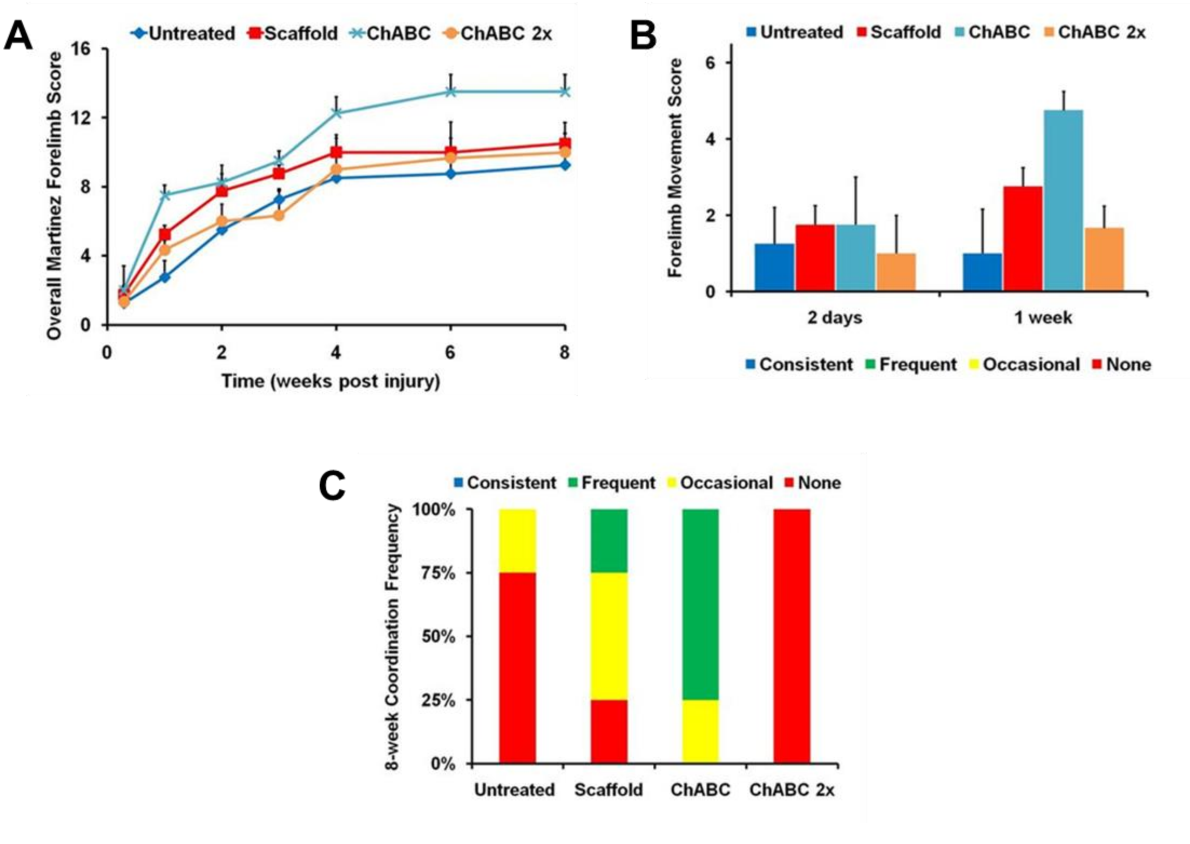

Figure 3.9. Plots of animal forelimb functional recovery after variable doses of chABC. Functional recovery of forelimb locomotion based on the Martinez recovery scale and animal survival. (a, b) Scoring was performed across four groups: untreated (blue, -♦-), blank patch (red, -■-), low-dose chABC patch (light blue, -X-), and high-dose chABC patch (orange, -▲-). a, Overall Martinez open-field scores from weeks 1 through 4, 6 and 8. b, Forelimb articular movement scores at 2 days and 1 week post SCI. c, Animal forelimb-hindlimb coordination frequency at 8 weeks post SCI.

Chapter 4: Biomaterials for In Utero Repair of Spina Bifida

4.1 Introduction

4.1.1 Spinal Cord Damage in Spina Bifida

Spina bifida is the most common congenital cause of lifelong lower extremity paralysis. It has an estimated incidence of 1/2700 live births in the United States. Open spina bifida, or myelomenigocele (MMC), is a neural tube closure defect that is often associated with impaired distal neurological function and cognitive disabilities. Spinal cord damage associated with MMC is due first to abnormal spinal cord development, and secondly to subsequent traumatic and chemical injury to the exposed cord[92,93].

4.1.2 Prenatal Repair of Spina Bifida

Results of the recently completed NIH-sponsored Management of Myelomeningocele Study (MOMS) randomized-controlled clinical trial comparing prenatal versus postnatal repair demonstrated that prenatal repair is both safe and efficacious[80]. In addition to a significantly decreased rate of shunt placement at 1 year compared to postnatal surgery, prenatal repair also showed partially improved motor outcomes at 30 months. Despite these promising results, distal neurological function remains incomplete even after prenatal MMC repair. Presumably, simple prenatal closure fails to reverse the neurological injury already incurred prior to the time of surgery.

To prevent the secondary ongoing in utero damage associated with an open spinal cord, prenatal MMC surgery consists of in utero closure of the dura mater and overlying soft tissues, with or without retubularization of the spinal cord. If primary closure is not feasible, closure with biosynthetic patch can be performed. This repair strategy was adapted from the experience of neurosurgeons performing postnatal repair in order to prevent further trauma and infection. Similarly, prenatal MMC repair is aimed solely at preventing further in utero damage to the spinal cord and stopping continued leakage of cerebrospinal fluid. Still, improvement in distal neurological function remains limited even after prenatal repair, however, because simple closure fails to reverse the neurological injury incurred prior to the time of repair.

4.1.3 Biomaterials for Spina Bifida Repair

Because prenatal MMC repair fails to completely reverse established neurological injury, further modifications are warranted to target prior damage. To address this, we hypothesized that the addition of a biodegradable scaffold to prenatal repair would promote tissue remodeling and neuronal pathfinding, and thus preserve distal neurological function better than simple closure. Biodegradable nanofibrous scaffolds serve as temporary 3D substrates to guide organized neo-tissue formation across damaged tissue[23,94]. These biomaterials promote new tissue formation by providing a surface with adequate porosity to foster cellular attachment, migration, proliferation, and differentiation of specific cell phenotypes at the nanometer scale. Furthermore, through the process of electrospinning, these scaffolds can be aligned in to provide directionality to cellular growth [23,94,95]. In this pilot study, we aimed to evaluate the practicality and safety of using aligned biodegradable nanofibrous scaffolds as a regenerative device in the sheep model of prenatal MMC.

4.1.4 Stem Cell Transplantation for Spinal Cord Regeneration

Neural crest stem cells (NCSCs) are a migratory, multipotent population of cells that form adjacent to the dorsal side of the developing neural tube during embryogenesis. The transplantation of NCSCs can improve neurological outcome in animal models of nerve injury[76,96–98]. Homologous skin-derived NCSCs have improved the distal locomotor and sensory function of rodents after spinal cord injury[97,98]. Recently, we developed a protocol to derive NCSCs from human induced pluripotent stem cells (iPSC-NCSCs) and reported that iPSC-NCSCs can facilitate the regeneration of injured peripheral nerves in rats[76].

Therapeutic NCSCs are postulated to act by exerting a combination of pertinent functions such as cell replacement, myelination, angiogenesis, and the modulation of scar formation in damaged nervous tissue[99,100]. IPSC-NCSCs may similarly repair and augment existing neuronal pathways and improve distal neurological function in MMC to a greater degree than seen when the spinal cord is covered only by dura and fetal skin. These stem cells can be seeded on a biocompatible surgical scaffold that has been previously implanted in the lamb model of fetal MMC[82]. The aims of this study were to derive human iPSC-NCSCs, surgically implant these cells in the fetal lamb model of MMC, and evaluate their subsequent survival, engraftment, and neuronal differentiation in the injured host spinal cord.

4.2 Materials and Methods

4.2.1 Scaffold Fabrication and iPSC-NCSC Seeding

Biodegradable aligned nanofibrous scaffolds composed of poly(L-lactide-co-caprolactone) (70:30, Purac Biomaterials, Amsterdam, Netherlands), poly(propylene glycol) (Acros Organics, Morris Plains, NJ) and sodium acetate (Sigma, St. Louis, MO) were fabricated by using a customized electrospinning process[94]. Scaffolds were sterilized by ethylene oxide gas sterilization before use. NCSCs were detached and re-suspended in SFM (2-3x104 cells/ul). The cell suspension was mixed with a cold hydrogel solution at a 2:1 ratio (volume to volume), and spread onto the surface of the scaffold (1.5 ml for one 5 cm × 5 cm surface). The cell-hydrogel-scaffold constructs were kept in the incubator for 1 h, and NCSC maintenance medium was added to cover the constructs. The culture was maintained in the incubator overnight before surgery.

4.2.2 In Vitro iPSC-NCSC Incorporation into 3D Hydrogel

A LIVE/DEAD assay (Molecular Probes, Grand Island, NY) was used to assess the viability of the NCSCs in the engineered scaffold in vitro. To test the neuronal differentiation capability of the iPSC-NCSCs incorporated with hydrogel and scaffold, the stem cell-hydrogel-scaffold construct was cultured in neural induction medium for 2 weeks. The neural induction medium was composed of DMEM supplemented with N2 neural supplement (Invitrogen), brain-derived neurotrophic factor (BDNF), nerve growth factor (NGF), glial cell-derived neurotrophic factor (GDNF) (R&D Systems, Minneapolis, MN), and 1 mM dibutyryl-cAMP (Sigma-Aldrich, St. Louis, MO).

4.2.3 In Vivo Transplantation in Fetal Spina Bifida Model

All experimental procedures with animals were approved by appropriate Institutional Animal Care and Use Committees, and all animals received care in compliance with the Guide for the Care and Use of Laboratory Animals in a facility accredited by the Association for the Assessment and Accreditation of Laboratory Animal Care International[101].

Multiple time-mated ewes were obtained one week prior to the first surgical intervention and housed in an appropriate establishment with free access to food and water except the last 24 hours. At approximately 75 days gestation, each ewe underwent survival laparotomy and hysterotomy for the creation of a fetal MMC defect. The MMC lesion was surgically created by exposing the spinal cord and opening the dura of each lamb[93,102]. At approximately 100 days gestation, ewes underwent a second survival laparotomy and hysterotomy, and some ewes underwent repair of the MMC defect with a rectangular iPSC-NCSC seeded scaffold and other received repair with only scaffold. The scaffold was longitudinally aligned, tailored to size, and surgically implanted over the exposed spinal cord using a continuous 6-0 absorbable suture (Figure 4.1). The skin of the fetal lamb was then closed in a second layer overlying the implanted scaffold.

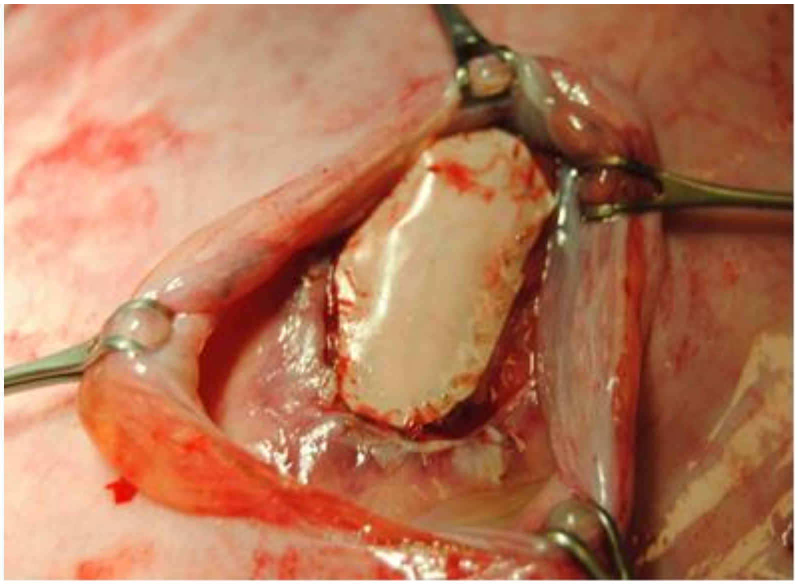

Figure 4.1. Surgical placement of the nanofibrous scaffold seeded with human iPSC-derived NCSCs at the time of fetal lamb MMC repair.

4.2.4 Delivery and Histopathological Analysis

Lambs were delivered via terminal cesarean section approximately ten days prior to term to prevent natural parturition and to optimize histopathological analysis. Lambs were sacrificed and perfused with an initial bolus of lidocaine (40mg) and heparin (1000 IU), followed by 1L of NaCl 0.9 % and 2L of 4% paraformaldehyde in 0.1M phosphate buffer. The brain, kidney, liver, spleen, and gastrointestinal tract of each lamb were grossly examined for the presence of tumors. The brain and spinal cord were then harvested for pathological analysis. Microscopy and immunohistochemical staining of the spinal cords were performed to identify the presence of cells expressing a human nuclear mitotic apparatus protein (NuMA) and of a mature axonal neurofilament subunit (Neurofilament M, NFM). In addition, other tissues sections were stained with Eriochrome Cyanate and Neutral Red (EC/NR), for myelin and neural cell bodies respectively, and Hematoxilin and Eosin (H&E).

4.3 Results and Discussion

4.3.1 In Vitro Characterization of iPSC-NCSCs

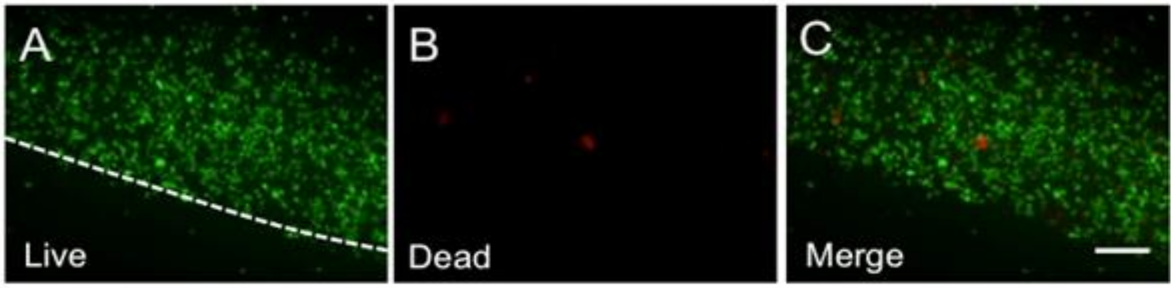

Figure 4.2. Concurrent viability assay of human iPSC-NCSCs at time of surgical transplantation. Cells were mixed with a 3D hydrogel, seeded on top of a nanofibrous scaffold, and cultured in vitro for 24 hours. Prior to transplantation, a cell viability was tested by using a live/dead assay. Live cells (calcein staining, in green) are shown in (a). Dead cells (ethidium homodimer-1 staining, in red) are shown in (b). A merge of live and dead cells is shown in (c). Dashed line indicates the interface between hydrogel (top) and scaffold (bottom). Scale bar = 100 μm.

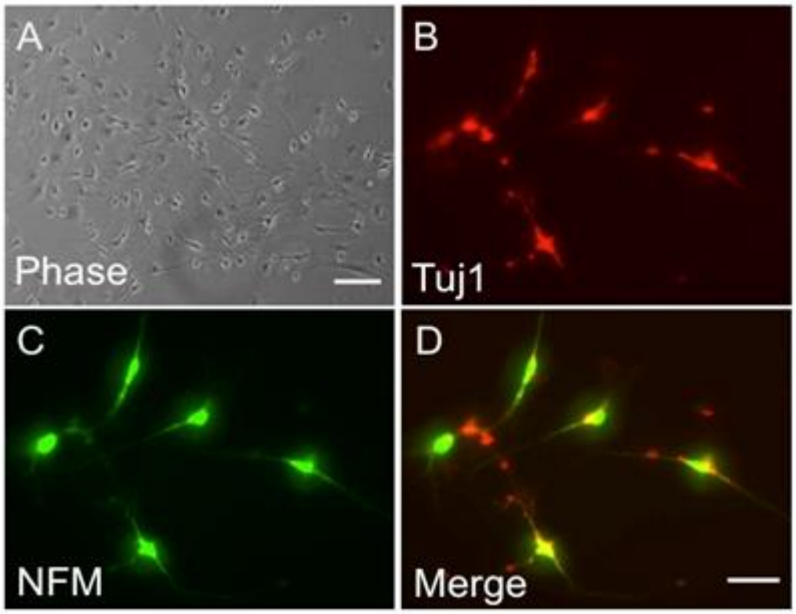

Figure 4.3. In vitro differentiation of human iPSC-NCSCs into neuronal cells in 3D hydrogel. a, Phase contrast images of neurons differentiated from ADAfE4-iPS38-2 cell line after one week differentiation in neuron cell induction medium in a 3D hydrogel. The expression of neuronal markers Tuj1 (b) and NFM (c) was positively characterized. A

merge of Tuj1 and NFM marker expression is shown in (d). Scale bar (a) = 100 µm. Scale bar (b, c, d) =10 µm.

All iPSC-NSCSs in primary explants were positive for the early NCSC markers nestin, AP2, and vimentin as previously described[76]. In vitro cell viability assays verified >95% viability of co-cultured cells at the time of surgical transplantation (Figure 4.2). In vitro neuronal differentiation studies demonstrated that iPSC-NCSCs maintained neuronal differentiation potential in the construct and that the differentiated neuronal cells possessed multiple neurites (Figure 4.3a) and expressed neuronal markers β-III tubulin (Tuj1) and NFM (Figure 4.3b-d).

4.3.2 In Vivo Transplantation and Gross Necropsy

Several repaired lamb had a small well-healed linear skin defect over the lumbar area and a flattened lumbar area and pelvic girdle that appeared small for the lamb's size. In one lamb, the umbilicus was twisted around the left hind limb just proximal to the tarsus causing malformation of lower left hindlimb.

Neuropathology revealed hindbrain and cerebellar herniation through foramen magnum consistent with a Chiari malformation in both lambs. The lateral ventricles were noticably larger than seen in the normal lamb, and gyri on the lateral frontal lobes were abnormally soft and collapsible. The skin over the lumbar area was adherent to the subcutaneous tissues consistent with scar formation. The lumbar vertebral spinous processes and laminae were absent. Grossly flattened spinal cord tissue was present from L4-L7. The outer scaffold was grossly visible, non-encapsulated and partially integrated but not yet completely incorporated with the underlying cord tissue.

Ewes were then carried through to the planned cesarean delivery at gestational day 135-136 without adverse event. At the time of surgical repair, scaffolds were tailored in size during the operation and placed both in their intra- and extradural position without difficulty (Figure 4.4). The operative time to create and repair the MMC defect was approximately 65 to 120 minutes per ewe. MMC lesions spanned spinal levels L1-L5 in repaired lamb 1 (RL1) and T13-L6 in repaired lamb 2 (RL2). At necropsy, RL1 had a well-healed 6 cm linear skin defect overlying the lumbosacral spine. The skin over the lumbar area was adherent to the subcutaneous tissues consistent with tethered scar formation. A partially integrated scaffold was grossly visible within this scar directly overlying the spinal cord. In RL2, there was a slighter larger 7 cm skin defect that had partially dehisced centrally to a maximum area of 2 cm. Again, an integrated scaffold was grossly visible directly overlying the spinal cord at the site of the skin defect.

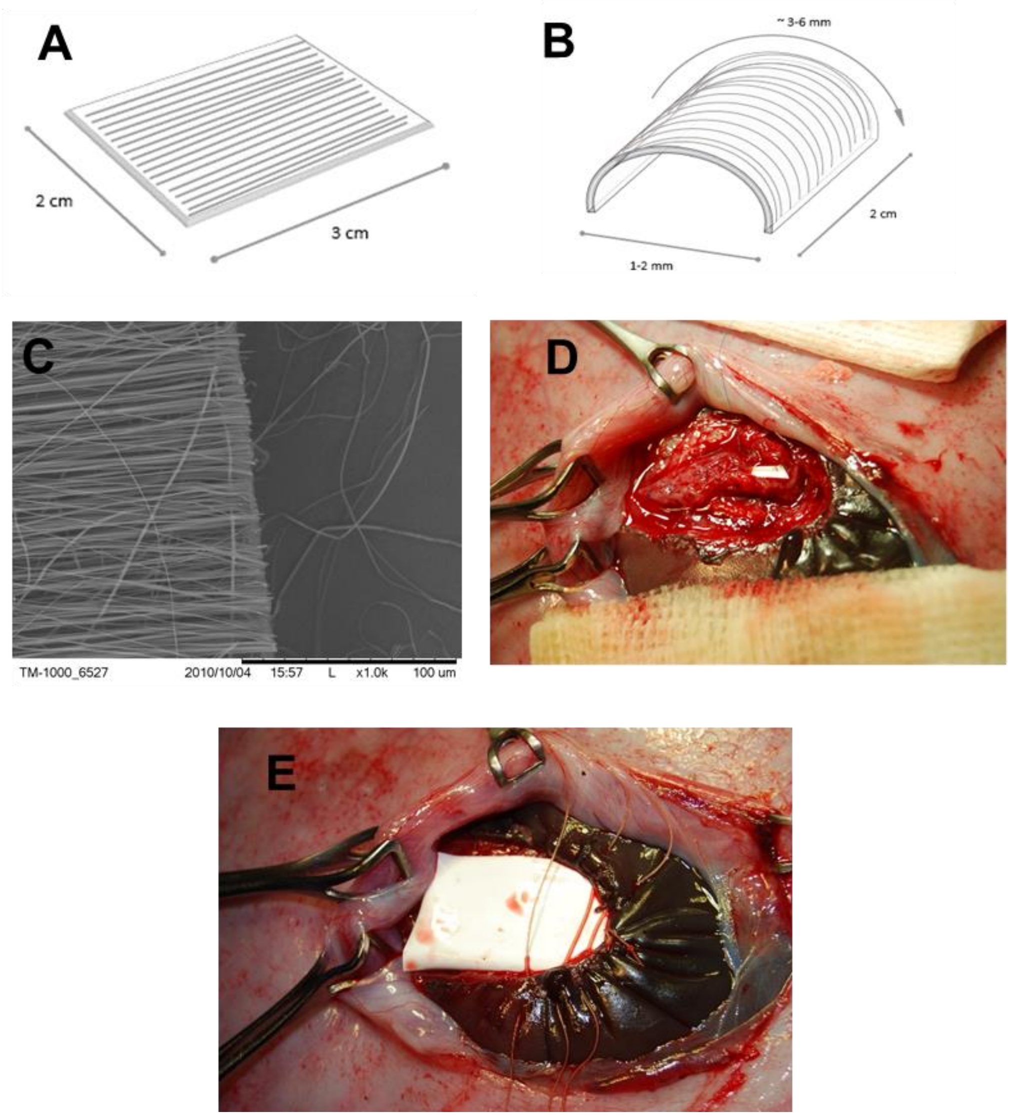

Figure 4.4. Schematic representation of nanofibrous (a) inner and (b) outer scaffold. c, High power electron micrograph of outer scaffold showing aligned poly L-lactic acid nanofibers. Operative repair of fetal lamb with (d) inner and (e) outer nanofibrous scaffolds.

4.3.3 Post-Transplantation Immunohistochemical Analysis

Lambs that underwent surgical MMC creation and repairshowed significant loss of dorsal white matter with sparing of the ventral horns on myelin staining (Figure 4.5a,b). Staining for neuronal cell bodies showed selective persistence of motor neurons in the ventral horns. The inner scaffold was visible dorsal to the central canal. Hematoxylin and eosin staining showed no evidence of lymphocytic infiltrate or abnormal connective tissue formation surrounding the scaffold (Figure4.6a,b). Astrocyte-like cells were found lining the scaffold adjacent to the cord tissue. There was no evidence of encapsulation.

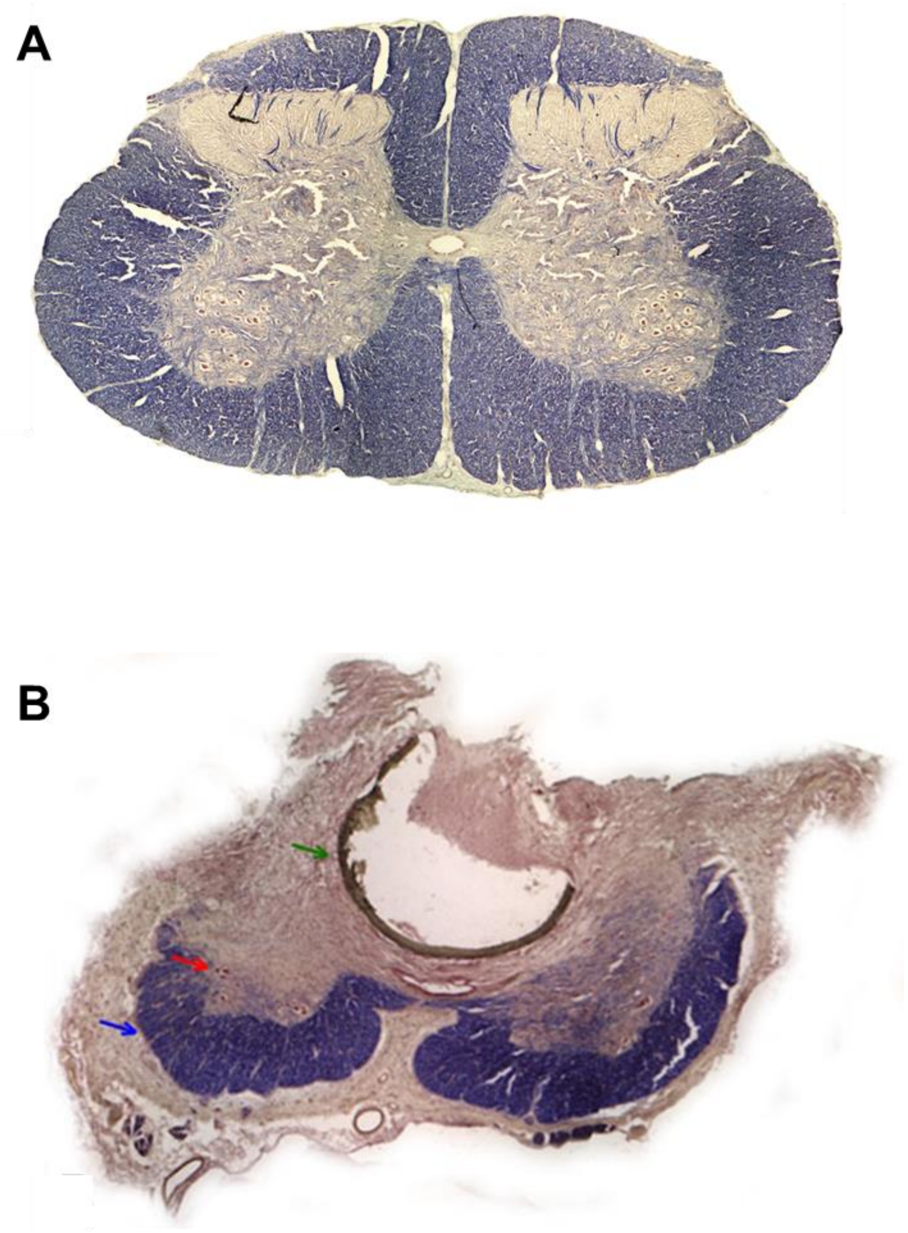

Figure 4.5. Cross-section of gestational age 133 lamb spinal cord at lumbar vertebral level stained with eriochrome cyanine (myelin) with neutral red counterstain (nissl substance) of (a) normal lamb and (b) lamb repaired with scaffold. In (b), note loss of dorsal white matter with relative sparing of ventral horn white matter (blue arrow) and a few visible ventral motor neurons (red arrow). This constellation of findings is comparable with myelomeningocele. The nanofibrous scaffold (green arrow) is visible just dorsal to the central canal.

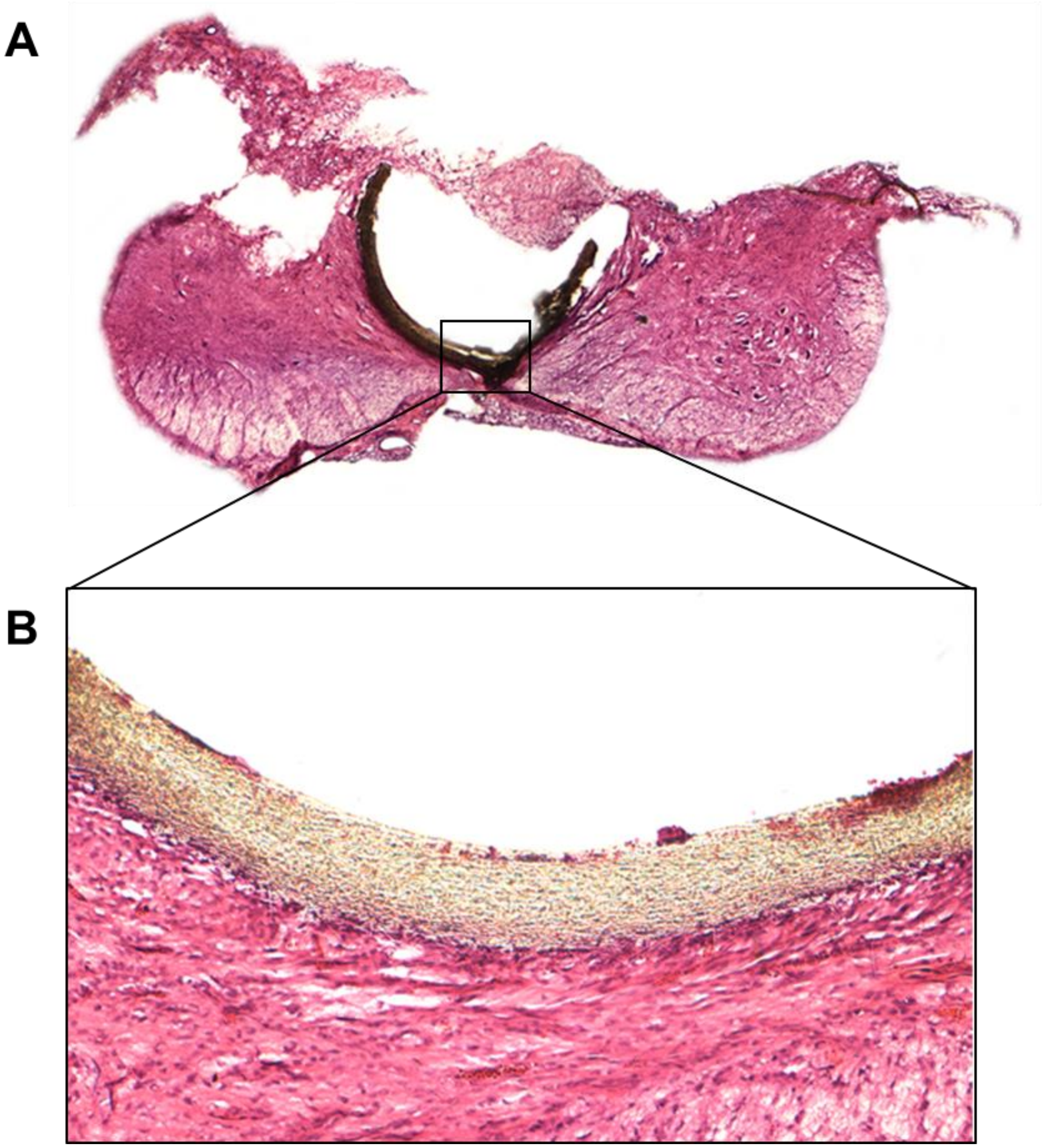

Figure 4.6. Cross-section of gestational age 133 lamb spinal cord at lumbar vertebral level stained with hematoxylin and eosin at (a) 25x magnification and (b) 100x magnification. Note scaffold appears well integrated with host tissues and lack of strong lymphocytic or fibrotic reaction.

Post-transplant immunohistochemistry demonstrated the survival and local retention of cells expressing human NuMA antigen in the spinal cord of repaired lambs at the level of the MMC lesion (Figure 4.7). Concurrent co-localization stains for NFM demonstrated the integration of the transplanted cells within the spinal cord axonal elements.

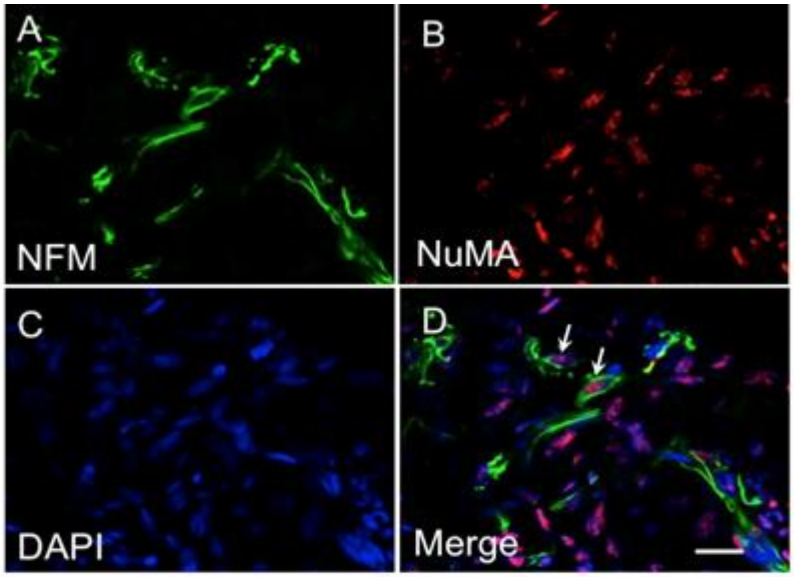

Figure 4.7. Survival and integration of human iPSC-NCSCs in the lesioned spinal cord thirty days after transplantation. The neurofilament marker NFM (a) and human nuclei antigen NuMA (b) were positively expressed. In (c), nuclei are stained by DAPI. In (d), white arrows indicate the co-localization of NFM and NuMA. Overall, approximately 35% of cells in representative sections expressed NuMa, with some local areas demonstrating up to 70% expression. Scale bar = 10 µm.

In this study, we introduce the concept of using aligned nanofibrous scaffolds in prenatal MMC repair and show that nanofibrous scaffolds are feasible for use in a large animal model of fetal MMC. The scaffolds are easy to position, and operative time is comparable to standard repair. Furthermore, they appear well-integrated to the surrounding tissues and nonencapsulated on necropsy. Histopathology reveals no evidence of significant leukocyte infiltration or excessive connective tissue formation as would expected by an inflammatory or fibrotic response. These results support the further investigation of nanofibrous scaffolds in prenatal MMC repair as a potential enhancement to the standard established by the MOMS trial. In addition, we describe the transplantation, survival, and integration of human iPSC-derived neural crest stem cells in the fetal lamb model of myelomeningocele. These stem cells were successfully seeded on a biocompatible scaffold that is readily adaptable to human fetal MMC repair. Moreover, the transplanted xenogeneic cells demonstrated continued survival thirty days after in utero transplantation despite the lack of host immunosuppression. Most significantly, iPSC-NCSCs anatomically differentiated into neuronal lineage when implanted into an injured spinal cord as demonstrated by the presence of mature axonal neurofilament markers.

This report also demonstrates the first human stem cell engraftment in a model of MMC and the first description of iPSC-NCSC integration in a model of spinal cord injury. We have previously reported the therapeutic potential for iPSC-NCSCs in peripheral nerve injury[76]. These cells preferentially differentiate into Schwann cells and become integrated into the myelin sheath around the peripheral axons of athymic rats. They thus enhance the myelination and the regeneration of injured peripheral nerves. Whether iPSC-NCSCs have similar therapeutic potential in the spinal cord has not been previously studied, although other groups have explored the potential of homologous skin-derived precursor (SKP-SC) and epidermal-derived neural crest stem cells (EPI-NCSCs) to recover neurological function in the injured spinal cord of mice[98,99]. These adult sources of NCSCs suffer from difficulties in cell isolation and expansion and low efficiency however. Another advantage of iPSC-derived cell replacement therapy over other skin-derived treatments is that patient-specific cell therapies can be created, thus potentially avoiding rejection. Finally, the unlimited expansion potential of iPSCs also makes them a valuable cell source for tissue engineering. These unique features make iPSC-derived NCSCs a particularly attractive candidate for cell therapy in MMC and spinal cord injury.

In the Management of Myelomeningocele Study, prenatal repair was associated with a significantly increased ability to ambulate independently at 30 months compared to the postnatal group (42% vs. 21%, RR 2.01 (1.16 – 3.48), p = .01)[80]. The fact that simple prenatal closure could provide some improvement in spinal cord function opens the door for pursuing additional strategies, such as cell replacement therapy, to further improve distal neurological function. By demonstrating the engraftment and differentiation of NCSC in the spinal cord, our results support the concept of using NCSCs to address the spinal cord damage in MMC. These findings encourage the further investigation of stem cells as a potential enhancement to the baseline results of fetal MMC repair, although further study, including functional neurological evaluation, will be needed to determine the ultimate therapeutic potential of this therapy.

The prenatal application of a stem cell-based therapy is especially promising because the in utero environment may provide a natural immunotolerance whereby the need for host immunosuppression could potentially be eliminated[103]. In addition, iPSCs provide the potential for using maternal or even autologous tissue sources for subsequent surgical implantation in MMC. Clinically, therapeutic cells could be harvested at the time of fetal diagnosis in the early second trimester, induced into neuronal lineage and culture-expanded, then surgically transplanted at the time of fetal surgery 6-8 weeks later. If prenatal in utero NCSC transplantation ultimately proves successful for patients with MMC, it would be reasonable to pursue a similar NCSC-based strategies for patients with other forms of spinal cord injury.

For over a century, the surgical management of the MMC lesion itself has been largely unchanged. Simple postnatal closure of the lesion has long been standard of care. The landmark results of the MOMS trial- the first randomized controlled trial to show efficacy of prenatal surgery for a nonlethal condition- have been the first major change in this standard. As open fetal surgery becomes more widespread for select cases of MMC, there are multiple potential directions in which prenatal MMC repair will need to be further refined, with perhaps the most important being improving distal neurological function.

Despite promising results for reversal of the Chiari malformation after prenatal surgery, improvements in the peripheral manifestations of MMC are frustratingly incomplete. With or without prenatal surgery, patients with MMC often have lifelong paralysis requiring prosthesis, bladder incontinence requiring operative intervention and bowel dysfunction. Due to improvements in the management of early infectious and cerebral complications of MMC, more patients are now surviving well into adulthood. Consequently, sexual dysfunction and psychological disturbances related to managing the peripheral manifestations of MMC are also becoming better recognized in patients. Clearly, improvements are needed to address the significant morbidities related to distal neurological dysfunction.

Normal spinal cord development is dependent upon appropriate neuronal communication and proper spatial relationships for differentiation and axonal pathfinding. In MMC, this communication and these relationships are disrupted by a defect in neural tube folding and by ongoing damage to the open spinal cord in utero. This is the basis of the “two-hit hypothesis” of MMC. Neural regeneration is then further limited by gliotic scar tissue formation. Modifications to prenatal MMC repair with the aim of improving distal neurological function should target this secondary damage by promoting neuronal pathfinding and bridging areas of gliosis and scar formation.

In the field of regenerative medicine, nanofibrous scaffolds have demonstrated the potential to bridge areas of scar tissue. Additionally, they can promote neuronal regeneration in both spinal cord and peripheral nerve injury models. They serve as a temporary ECM for regenerative cells by emulating the nanofibrous features of collagen and other ECM components such as fibronectin and proteoglycans. Because MMC is essentially a form of congenital spinal injury, the success of nanofibrous scaffolds in other nerve injury models can be theoretically translated to MMC repair. By combining early repair with the regenerative properties of nanofibrous scaffolds, neuronal pathfinding could be promoted and distal neurological function presumably improved.

Perhaps more significantly, simple modifications allow nanofibrous scaffolds to serve as a biodegradable delivery mechanism for immunomodulatory substances, growth factors and stem cells[38,104]. Studies with scaffolds loaded with the anti-inflammatory drug rolipram, which enhances cyclic adenosine monophosphate (cAMP) activity, have already shown significantly improved axon growth in a spinal cord injury model[81]. The addition of basic fibroblast growth factor in a rat model of prenatal MMC repair has been shown to improve epidermal ingrowth and neovascularization[105]. Neural stem cell delivery is being actively studied as an adjunct to current prenatal repair[106]. However, sustained and local delivery of these substances in utero is a barrier that would still need to be addressed. Whether immunomodulators, growth factors or stem cells, nanofibrous scaffolds can provide prolonged release of bioactive factors at the site of the MMC lesion and thus replace injections or other mechanical and invasive modes of sustained delivery.

Regenerative therapies may be particularly promising for use in prenatal repair due to the inherent plasticity and immunotolerance unique to the developing fetal environment. The fetus has long been recognized to have a remarkable ability to heal after injury. Additionally, longstanding work with in utero hematopoietic stem cell transplantation has shown that the fetal environment offers considerable advantages for the success of stem cell transplantation[107]. The immunological immaturity of the early gestational fetus provides a unique opportunity for induction of donor-specific tolerance to allogenic cells[103]. It has thus been suggested that fetal tolerance can potentially eliminate the requirement for immunosuppression after stem cell therapy. This work supports of the addition of a regenerative treatment strategy, with or without stem cell therapy, in future modifications of prenatal MMC repair.

In this report we use a sheep model of MMC to demonstrate that biodegradable nanofibrous scaffolds are surgically feasible for repair of open spina bifida. We show that nanofibrous scaffolds are non-inflammatory in an in vivo spinal injury model. Additional modifications to the nanofibrous polymer will determine the optimal structure and alignment of these scaffolds. Further study will determine the potential of these scaffolds for neural cell infiltration, delivery of growth factors, immunomodulators, and neurological recovery greater than current in utero repair. In addition, we report for the first time the successful engraftment of human stem cells in a fetal model of MMC. Additionally, we have described the derivation of NCSCs from iPSCs and propose a technique for their surgical transplantation in human prenatal MMC repair. If iPSC-NCSCs can ameliorate distal neurological function in MMC, they may have the added potential to be effective in other forms of acute spinal cord injury.

Chapter 5: Conclusion

5.1 Dissertation Conclusions and Broader Implications

The focus of my research lies at the intersection of biomaterial design and cell mechanobiology in the context of biomedical application. As a researcher, I am interested in better understanding ways in which the chemical and biophysical microenvironment influences adult cell behavior and phenotype determination. This information has proven to have profound implications in the broad scope of cell biology and is critical to the successful design of next-generation biomaterials.

This dissertation research investigates how biophysical factors can alter a cell's epigenetic state, and how this information can be used to optimize biomaterials for a diverse range of biomedical applications. Recognized as the 2012 Nobel Prize-winning research in medicine, cell reprogramming, for example, represents a major advancement in cell biology and has wide applications in regenerative medicine, disease modeling, and drug screening. Induced pluripotent stem cells (iPSCs) can be produced from somatic cells, typically adult fibroblasts, via the forced expression of four or less transcription factors. Although extensive studies have been performed investigating the roles of transcription factors and chemical compounds in cell reprogramming, the role of biophysical factors in cell reprogramming has yet to be revealed.

The topographical and mechanical properties of cell-adhesive materials have been shown to regulate a variety of cellular functions such as migration, proliferation and differentiation. Importantly, these functions have closely-related influences in a broad range of complex biological processes such as wound healing, tissue remodeling, and tumor growth. There is also evidence that biophysical signals can be transmitted through the cytoskeleton into the nucleus to affect chromatin properties. Until now, however, it has not been shown whether and/or how the biophysical properties of cell-adhesive materials influence adult cell reprogramming, a reverse process of cell differentiation. In addition, whether intracellular mechanotransduction can induce critical epigenetic modifications in somatic cells, which might facilitate the reprogramming process, remains unclear.

This work demonstrates, for the first time, that biophysical cues (e.g., topography and matrix stiffness) can significantly improve upon reprogramming efficiency and replace the effects of small molecule epigenetic modifiers in cell reprogramming. Further investigation shows that the mechanisms which govern this biophysical enhancement of cell reprogramming revolve around mechanomodulation of two histone modifying proteins, which produce concomitant modifications of the global epigenetic signatures in adult fibroblasts. Interestingly, these signatures include epigenetic marks that are highly present in embryonic stem cells and critical for cell reprogramming. Disruption of the actin cytoskeleton and actin-myosin contractility abolishes the microtopographical regulation of epigenetic modifications and cell reprogramming, suggesting that the actin cytoskeleton is required for this epigenetic mechanomodulation. Finally, this work demonstrates that microgroove topography promotes the upregulation of key epithelial-related genes, suggesting the initiation of a mesenchymal-to-epithelial transition (MET) – a required step in cell reprogramming – in adult fibroblasts. This work unravels how the biophysical properties of cell-adhesive materials can induce epigenetic modifications, which in turn lead to enhanced cell reprogramming. This novel biophysical regulation of epigenetics has important implications in cell reprogramming and in the optimization of materials for broad biological applications.

An adjacent focus of this dissertation expands the new and emerging field of tissue engineering by introducing creative combinatorial therapeutic platforms for regenerative medicine. Specifically, this work focuses on designing implantable therapeutic devices that allow for the combined delivery of therapeutic drugs, multipotent cells, and nano/microtopographical guidance cues for meaningful tissue formation. The direct application of this work is aimed towards spinal cord regeneration after both injury and neural tube defect (e.g., spina bifida). This work is of great importance to the field of biomedical engineering, as spinal cord repair remains one of the biggest challenges for regenerative medicine. In addition, recent studies have found that spinal cord injury (SCI), for example, is over five times more prevalent than previously estimated, bringing the total number of people living with SCI to over one million in the United States alone. This dissertation sheds light onto the current challenges within this field and present new and exciting potential solutions.

5.2 Future Directions

In any given physiological microenvironment, cells may experience a number of different chemical and/or biophysical inputs, which can induce drastic changes in epigenetic signature. Given the broad influence of epigenetics in cell behavior and phenotype determination, the results from this dissertation work provide a rational basis for the optimization of biomaterials and the cellular microenvironment for a number of biomedical applications.

Moving forward, I hope to expand upon these contributions to the fields of cell mechanobiology and regenerative medicine by 1) elucidating the upstream pathways and physical linkages that allow for biophysical regulation of cell epigenetic state and 2) helping to understand and demonstrate how these mechanomodulated epigenetic changes alter cell behavior in scar formation and wound healing, direct cell reprogramming into cardiomyocytes and neurons, tumor growth and metastasis, and adult stem/progenitor cell recruitment and differentiation in response to biomaterial implantation (Figure 5.1). This information will be of critical importance to the field of biomedical engineering as it will present new and exciting ways in which we can maximize the potential of stem cell technologies, mitigate pathophysiological response in injured and diseased states, and greatly improve the design of next-generation biomaterials. Importantly, this work has the potential to make unprecedented contributions to the advancement of human health.

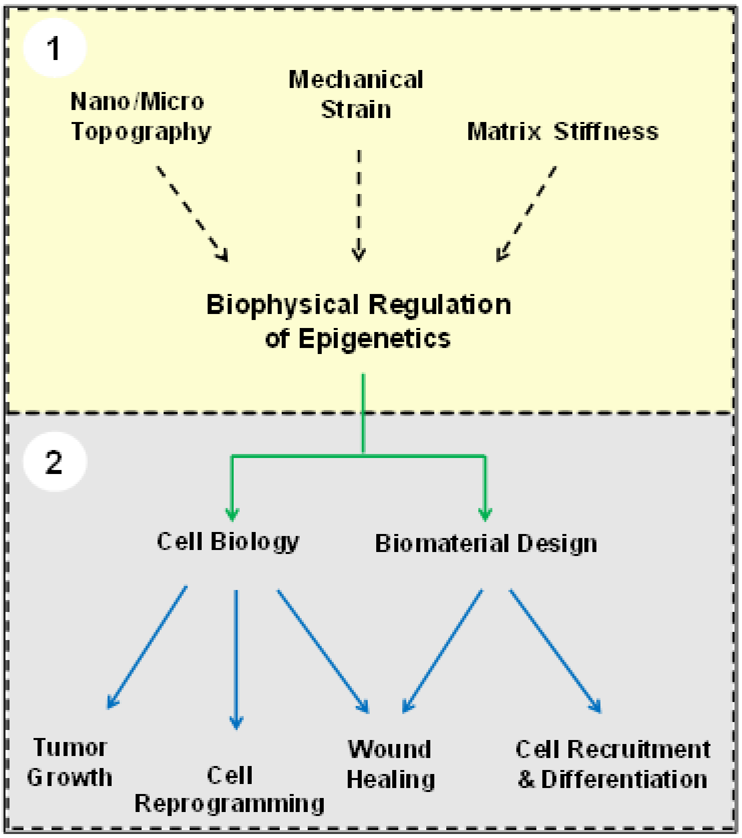

Figure 5.1. Overview of research goals and the role of biophysical regulation of epigenetics in the advancement of human health.

Future works might aim to investigate, for example, how the biophysical regulation of the epigenetic state can influence the process of direct cell reprogramming, a process that converts adult fibroblasts directly into functional somatic cell types (e.g., neurons and cardiomyocytes).

Following myocardial infarction, cardiac fibroblasts within the infracted heart contribute to the deposition of scar-like matrix components, which inhibit efficient cardiac output. Through direct reprogramming techniques, cardiac fibroblasts within the infarcted heart can be converted directly into functional cardiomyocytes, leading to decreased infarct size and attenuation of cardiac dysfunction[51]. Interestingly, this work also highlights the observation that cardiac fibroblasts directly reprogram into functional cardiomyocytes more effectively in vivo rather than in vitro. This observation suggests that factors within the native microenvironment – including the extracellular matrix, secreted proteins, tissue stiffness, topography, and mechanical stretch – may further enhance the direct reprogramming process. It would be interesting to investigate the role of substrate topography and mechanical stretch (two distinct characteristics of the heart microenvironment) on the direct reprogramming of cardiac fibroblasts into functional cardiomyocytes. One might hypothesize that biophysical factors in the microenvironment can modulate the epigenetic state and regulate the direct reprogramming of cardiac fibroblasts into cardiomyocytes.

The proposed investigation may result in groundbreaking discovery, and could have a broad impact in the area of mechanotransduction and direct cell reprogramming. This work would also provide a clearer understanding of how biophysical factors can promote the direct conversion of cardiac fibroblasts into functional cardiomyocytes in vivo and reveal key molecular targets within the signaling pathways involved. With this understanding, we can begin to develop better therapies that can effectively treat and prevent heart failure.

References

1. Takahashi, K. & Yamanaka, S. Induction of pluripotent stem cells from mouse embryonic and adult fibroblast cultures by defined factors. *Cell* **126,** 663–76 (2006).

2. Yu, J. *et al.* Induced pluripotent stem cell lines derived from human somatic cells. *Science (New York, N.Y.)* **318,** 1917–20 (2007).

3. Park, I.-H. *et al.* Reprogramming of human somatic cells to pluripotency with defined factors. *Nature* **451,** 141–6 (2008).

4. Wernig, M. *et al.* In vitro reprogramming of fibroblasts into a pluripotent ES-cell-like state. *Nature* **448,** 318–24 (2007).

5. Redmer, T. *et al.* E-cadherin is crucial for embryonic stem cell pluripotency and can replace OCT4 during somatic cell reprogramming. *EMBO reports* **12,** 720–6 (2011).

6. Li, D. *et al.* Integrated biochemical and mechanical signals regulate multifaceted human embryonic stem cell functions. *The Journal of cell biology* **191,** 631–44 (2010).

7. Li, R. *et al.* A mesenchymal-to-epithelial transition initiates and is required for the nuclear reprogramming of mouse fibroblasts. *Cell stem cell* **7,** 51–63 (2010).

8. Feng, B., Ng, J.-H., Heng, J.-C. D. & Ng, H.-H. Molecules that promote or enhance reprogramming of somatic cells to induced pluripotent stem cells. *Cell stem cell* **4,** 301–12 (2009).

9. Li, Y. *et al.* Generation of iPSCs from mouse fibroblasts with a single gene, Oct4, and small molecules. *Cell research* **21,** 196–204 (2011).

10. Huangfu, D. *et al.* Induction of pluripotent stem cells from primary human fibroblasts with only Oct4 and Sox2. *Nature biotechnology* **26,** 1269–75 (2008).

11. Huangfu, D. *et al.* Induction of pluripotent stem cells by defined factors is greatly improved by small-molecule compounds. *Nature biotechnology* **26,** 795–7 (2008).

12. Zhu, S. *et al.* Reprogramming of human primary somatic cells by OCT4 and chemical compounds. *Cell stem cell* **7,** 651–5 (2010).

13. Anokye-Danso, F. *et al.* Highly efficient miRNA-mediated reprogramming of mouse and human somatic cells to pluripotency. *Cell stem cell* **8,** 376–88 (2011).

14. Pasque, V., Jullien, J., Miyamoto, K., Halley-Stott, R. P. & Gurdon, J. B. Epigenetic factors influencing resistance to nuclear reprogramming. *Trends in genetics : TIG* **27,** 516–25 (2011).

15. Plath, K. & Lowry, W. E. Progress in understanding reprogramming to the induced pluripotent state. *Nature reviews. Genetics* **12,** 253–65 (2011).

16. Onder, T. T. *et al.* Chromatin-modifying enzymes as modulators of reprogramming. *Nature* **483,** 598–602 (2012).

17. Engler, A. J., Sen, S., Sweeney, H. L. & Discher, D. E. Matrix elasticity directs stem cell lineage specification. *Cell* **126,** 677–89 (2006).

18. Paszek, M. J. *et al.* Tensional homeostasis and the malignant phenotype. *Cancer cell* **8,** 241–54 (2005).

19. McBeath, R., Pirone, D. M., Nelson, C. M., Bhadriraju, K. & Chen, C. S. Cell shape, cytoskeletal tension, and RhoA regulate stem cell lineage commitment. *Developmental cell* **6,** 483–95 (2004).

20. Chowdhury, F. *et al.* Material properties of the cell dictate stress-induced spreading and differentiation in embryonic stem cells. *Nature materials* **9,** 82–8 (2010).

21. Engler, A. J., Humbert, P. O., Wehrle-haller, B. & Weaver, V. M. Multiscale Modeling of Form and Function. *Science (New York, N.Y.)* **324,** 208–212 (2009).

22. DuFort, C. C., Paszek, M. J. & Weaver, V. M. Balancing forces: architectural control of mechanotransduction. *Nature reviews. Molecular cell biology* **12,** 308–19 (2011).

23. Patel, S. *et al.* Bioactive nanofibers: synergistic effects of nanotopography and chemical signaling on cell guidance. *Nano letters* **7,** 2122–8 (2007).

24. Thakar, R. G., Ho, F., Huang, N. F., Liepmann, D. & Li, S. Regulation of vascular smooth muscle cells by micropatterning. *Biochemical and Biophysical Research Communications* **307,** 883–890 (2003).

25. Huang, N. F. *et al.* Myotube assembly on nanofibrous and micropatterned polymers. *Nano letters* **6,** 537–42 (2006).

26. Park, J. S. *et al.* The effect of matrix stiffness on the differentiation of mesenchymal stem cells in response to TGF-β. *Biomaterials* **32,** 3921–30 (2011).

27. Guilak, F. *et al.* Control of stem cell fate by physical interactions with the extracellular matrix. *Cell stem cell* **5,** 17–26 (2009).

28. Discher, D. E., Mooney, D. J. & Zandstra, P. W. Growth factors, matrices, and forces combine and control stem cells. *Science (New York, N.Y.)* **324,** 1673–7 (2009).

29. Wozniak, M. a & Chen, C. S. Mechanotransduction in development: a growing role for contractility. *Nature reviews. Molecular cell biology* **10,** 34–43 (2009).

30. Wang, N., Tytell, J. D. & Ingber, D. E. Mechanotransduction at a distance: mechanically coupling the extracellular matrix with the nucleus. *Nature reviews. Molecular cell biology* **10,** 75–82 (2009).

31. Poh, Y.-C. *et al.* Dynamic force-induced direct dissociation of protein complexes in a nuclear body in living cells. *Nature Communications* **3,** (2012).

32. McMurray, R. J. *et al.* Nanoscale surfaces for the long-term maintenance of mesenchymal stem cell phenotype and multipotency. *Nature materials* **10,** 637–44 (2011).

33. Gilbert, P. M. *et al.* Substrate elasticity regulates skeletal muscle stem cell self-renewal in culture. *Science (New York, N.Y.)* **329,** 1078–81 (2010).

34. Li, D. *et al.* Role of mechanical factors in fate decisions of stem cells. *Regen Med.* **6,** 229–240 (2011).

35. Chowdhury, F. *et al.* Soft substrates promote homogeneous self-renewal of embryonic stem cells via downregulating cell-matrix tractions. *PloS one* **5,** e15655 (2010).

36. Ji, L., LaPointe, V. L. S., Evans, N. D. & Stevens, M. M. Changes in embryonic stem cell colony morphology and early differentiation markers driven by colloidal crystal topographical cues. *European cells & materials* **23,** 135–46 (2012).

37. Li, Y. *et al.* Biophysical regulation of histone acetylation in mesenchymal stem cells. *Biophysical journal* **100,** 1902–9 (2011).

38. Downing, T. L. *et al.* Drug-eluting microfibrous patches for the local delivery of rolipram in spinal cord repair. *Journal of controlled release : official journal of the Controlled Release Society* **161,** 910–7 (2012).

39. Cheng, Q., Komvopoulos, K. & Li, S. Surface chemical patterning for long-term single-cell culture. *J Biomed Mater Res Part A* **96A,** 507–512 (2011).

40. Sommer, C. a *et al.* Excision of Reprogramming Transgenes Improves the Differentiation Potential of iPS Cells Generated with a Single Excisable Vector. *Stem Cells* **28,** 64–74 (2010).

41. Buganim, Y., Faddah, D. a & Jaenisch, R. Mechanisms and models of somatic cell reprogramming. *Nature reviews. Genetics* **14,** 427–39 (2013).

42. Tavernier, G., Mlody, B., Demeester, J., Adjaye, J. & De Smedt, S. C. Current methods for inducing pluripotency in somatic cells. *Advanced materials (Deerfield Beach, Fla.)* **25,** 2765–71 (2013).

43. Ang, Y.-S. *et al.* WDR5 mediates self-renewal and reprogramming via the embryonic stem cell core transcriptional network. *Cell* **145,** 183–97 (2011).

44. Peinado, H., Ballestar, E., Esteller, M. & Cano, A. Snail Mediates E-Cadherin Repression by the Recruitment of the Sin3A/Histone Deacetylase 1 (HDAC1)/HDAC2 Complex. *Molecular and Cellular Biology* **24,** 306–319 (2004).

45. Wu, M.-Z. *et al.* Interplay between HDAC3 and WDR5 is essential for hypoxia-induced epithelial-mesenchymal transition. *Molecular Cell* **43,** 811–822 (2011).

46. Zhou, Q., Brown, J., Kanarek, A., Rajagopal, J. & Melton, D. a. In vivo reprogramming of adult pancreatic exocrine cells to beta-cells. *Nature* **455,** 627–32 (2008).

47. Ieda, M. *et al.* Direct reprogramming of fibroblasts into functional cardiomyocytes by defined factors. *Cell* **142,** 375–86 (2010).

48. Pang, Z. P. *et al.* Induction of human neuronal cells by defined transcription factors. *Nature* **476,** 220–3 (2011).

49. Karow, M. *et al.* Reprogramming of pericyte-derived cells of the adult human brain into induced neuronal cells. *Cell stem cell* **11,** 471–6 (2012).

50. Thier, M. *et al.* Direct conversion of fibroblasts into stably expandable neural stem cells. *Cell stem cell* **10,** 473–9 (2012).

51. Qian, L. *et al.* In vivo reprogramming of murine cardiac fibroblasts into induced cardiomyocytes. *Nature* **485,** 593–8 (2012).

52. Reeve Foundation. *One Degree of Separation | Paralysis and Spinal Cord Injury in the United States*. 1–28 (2009).

53. Fitch, M. T. & Silver, J. CNS injury , glial scars , and inflammation : Inhibitory extracellular matrices and regeneration failure. *Experimental neurology* **209,** 294–301 (2008).

54. Nakamura, F. & Vartanian, T. Identification of the Nogo inhibitor of axon regeneration as a Reticulon protein. *NAture* **403,** 439–444 (2000).

55. Mukhopadhyay, G., Doherty, P., Walsh, F. S., Crocker, P. R. & Filbin, M. T. A novel role for myelin-associated glycoprotein as an inhibitor of axonal regeneration. *Neuron* **13,** 757–67 (1994).

56. Niederöst, B. P., Zimmermann, D. R., Schwab, M. E. & Bandtlow, C. E. Bovine CNS myelin contains neurite growth-inhibitory activity associated with chondroitin sulfate proteoglycans. *The Journal of neuroscience : the official journal of the Society for Neuroscience* **19,** 8979–89 (1999).

57. Smith-Thomas, L. C. *et al.* Increased axon regeneration in astrocytes grown in the presence of proteoglycan synthesis inhibitors. *Journal of cell science* **108 (Pt 3,** 1307–15 (1995).

58. Thuret, S., Moon, L. D. F. & Gage, F. H. Therapeutic interventions after spinal cord injury. *Nature reviews. Neuroscience* **7,** 628–43 (2006).

59. Yiu, G. & He, Z. Glial inhibition of CNS axon regeneration. *Nature reviews. Neuroscience* **7,** 617–27 (2006).

60. Schwab, M. E. Repairing the injured spinal cord. *Science (New York, N.Y.)* **295,** 1029–31 (2002).

61. Baptiste, D. C. & Fehlings, M. G. Emerging drugs for spinal cord injury. *Expert Opinion on Emerging Drugs* **13,** 63–80 (2008).

62. Zhu, J., Mix, E. & Winblad, B. The antidepressant and antiinflammatory effects of rolipram in the central nervous system. *CNS Drug Reviews* **7,** 387–98 (2001).

63. Griswold, D. E. *et al.* Effect of selective phosphodiesterase type IV inhibitor, rolipram, on fluid and cellular phases of inflammatory response. *Inflammation* **17,** 333–44 (1993).

64. Pearse, D. D. *et al.* cAMP and Schwann cells promote axonal growth and functional recovery after spinal cord injury. *Nature medicine* **10,** 610–6 (2004).

65. Nikulina, E., Tidwell, J. L., Dai, H. N., Bregman, B. S. & Filbin, M. T. The phosphodiesterase inhibitor rolipram delivered after a spinal cord lesion promotes axonal regeneration and functional recovery. *Proceedings of the National Academy of Sciences of the United States of America* **101,** 8786–90 (2004).

66. Iannotti, C. A. *et al.* A combination immunomodulatory treatment promotes neuroprotection and locomotor recovery after contusion SCI. *Experimental neurology* **230,** 3–15 (2011).

67. Whitaker, C. M. *et al.* Rolipram attenuates acute oligodendrocyte death in the adult rat ventrolateral funiculus following contusive cervical spinal cord injury. *Neuroscience letters* **438,** 200–4 (2008).

68. Beaumont, E., Whitaker, C. M., Burke, D. a, Hetman, M. & Onifer, S. M. Effects of rolipram on adult rat oligodendrocytes and functional recovery after contusive cervical spinal cord injury. *Neuroscience* **163,** 985–90 (2009).

69. Koopmans, G. C. *et al.* Acute rolipram/thalidomide treatment improves tissue sparing and locomotion after experimental spinal cord injury. *Experimental Neurology* **216,** 490–498 (2009).

70. Sharp, K. G., Flanagan, L. a, Yee, K. M. & Steward, O. A re-assessment of a combinatorial treatment involving Schwann cell transplants and elevation of cyclic AMP on recovery of motor function following thoracic spinal cord injury in rats. *Experimental neurology* **233,** 625–44 (2012).

71. Nout, Y. S. *et al.* Glial restricted precursor cell transplant with cyclic adenosine monophosphate improved some autonomic functions but resulted in a reduced graft size after spinal cord contusion injury in rats. *Experimental neurology* **227,** 159–71 (2011).

72. Teng, Y. D. *et al.* Functional recovery following traumatic spinal cord injury mediated by a unique polymer scaffold seeded with neural stem cells. *Proceedings of the National Academy of Sciences of the United States of America* **99,** 3024–9 (2002).

73. Tysseling-Mattiace, V. M. *et al.* Self-assembling nanofibers inhibit glial scar formation and promote axon elongation after spinal cord injury. *The Journal of neuroscience : the official journal of the Society for Neuroscience* **28,** 3814–23 (2008).

74. Oudega, M. *et al.* Axonal regeneration into Schwann cell grafts within resorbable poly(alpha-hydroxyacid) guidance channels in the adult rat spinal cord. *Biomaterials* **22,** 1125–36 (2001).

75. Friedman, J. A. *et al.* Biodegradable polymer grafts for surgical repair of the injured spinal cord. *Neurosurgery* **51,** 742–51; discussion 751–2 (2002).

76. Wang, A. *et al.* Induced pluripotent stem cells for neural tissue engineering. *Biomaterials* **32,** 5023–32 (2011).

77. Zhu, Y. *et al.* Engineering Bi-Layer Nanofibrous Conduits for Peripheral Nerve Regeneration. (2011). at <http://online.liebertpub.com/doi/abs/10.1089/ten.tec.2010.0565>

78. Wang, A. *et al.* Physical properties and biocompatibility of a porous chitosan-based fiber-reinforced conduit for nerve regeneration. *Biotechnology letters* **29,** 1697–702 (2007).

79. Wang, A. *et al.* Porous chitosan tubular scaffolds with knitted outer wall and controllable inner structure for nerve tissue engineering. *Journal of biomedical materials research. Part A* **79,** 36–46 (2006).

80. Adzick, N. S. *et al.* A Randomized Trial of Prenatal versus Postnatal Repair of Myelomeningocele. *The New England Journal of Medicine* **364,** 993–1004 (2011).

81. Zhu, Y. *et al.* Nanofibrous Patches for Spinal Cord Regeneration. *Advanced functional materials* **20,** 1433–1440 (2010).

82. Saadai, P. *et al.* Prenatal repair of myelomeningocele with aligned nanofibrous scaffolds-a pilot study in sheep. *Journal of pediatric surgery* **46,** 2279–83 (2011).

83. Hashi, C. K. *et al.* Antithrombogenic property of bone marrow mesenchymal stem cells in nanofibrous vascular grafts. *Proceedings of the National Academy of Sciences of the United States of America* **104,** 11915–20 (2007).

84. Tønnesen, H. H. & Karlsen, J. Alginate in drug delivery systems. *Drug development and industrial pharmacy* **28,** 621–30 (2002).

85. Martinez, M., Brezun, J.-M., Bonnier, L. & Xerri, C. A new rating scale for open-field evaluation of behavioral recovery after cervical spinal cord injury in rats. *Journal of neurotrauma* **26,** 1043–53 (2009).

86. BASSO, D. M., BEATTIE, M. S. & BRESNAHAN, J. C. A Sensitive and Reliable Locomotor Rating Scale for Open Field Testing in Rats. *Journal of Neurotrauma* **12,** 1–21 (1995).

87. Willerth, S. M. & Sakiyama-Elbert, S. E. Approaches to neural tissue engineering using scaffolds for drug delivery. *Advanced drug delivery reviews* **59,** 325–38 (2007).

88. Kajana, S. & Goshgarian, H. G. Administration of phosphodiesterase inhibitors and an adenosine A1 receptor antagonist induces phrenic nerve recovery in high cervical spinal cord injured rats. *Experimental neurology* **210,** 671–680 (2008).

89. Wachtel, H. POTENTIAL ANTIDEPRESSANT ACTIVITY OF ROLIPRAM AND OTHER SELECTIVE CYCLIC ADENOSINE 3’,5'-MONOPHOSPHATE PHOSPHODIESTERASE INHIBITORS. *Neuropharmacology* **22,** 267–272 (1983).

90. Wachtel, H. & Schneider, H. H. Rolipram, a novel antidepressant drug, reverses the hypothermia and hypokinesia of monoamine-depleted mice by an action beyond postsynaptic monoamine receptors. *Neuropharmacology* **25,** 1119–26 (1986).

91. Hebenstreit, G. F. *et al.* Rolipram in major depressive disorder: results of a double-blind comparative study with imipramine. *Pharmacopsychiatry* **22,** 156–60 (1989).

92. Fichter, M. A. *et al.* Fetal spina bifida repair--current trends and prospects of intrauterine neurosurgery. *Fetal diagnosis and therapy* **23,** 271–86 (2008).

93. Stiefel, D. & Meuli, M. Scanning electron microscopy of fetal murine myelomeningocele reveals growth and development of the spinal cord in early gestation and neural tissue destruction around birth. *Journal of pediatric surgery* **42,** 1561–5 (2007).

94. Kurpinski, K. T., Stephenson, J. T., Janairo, R. R. R., Lee, H. & Li, S. The effect of fiber alignment and heparin coating on cell infiltration into nanofibrous PLLA scaffolds. *Biomaterials* **31,** 3536–42 (2010).

95. Lam, H. J., Patel, S., Wang, A., Chu, J. & Li, S. In vitro regulation of neural differentiation and axon growth by growth factors and bioactive nanofibers. *Tissue engineering. Part A* **16,** 2641–8 (2010).

96. Sieber-Blum, M. Epidermal neural crest stem cells and their use in mouse models of spinal cord injury. *Brain research bulletin* **83,** 189–93 (2010).

97. Biernaskie, J. *et al.* Skin-derived precursors generate myelinating Schwann cells that promote remyelination and functional recovery after contusion spinal cord injury. *The Journal of neuroscience : the official journal of the Society for Neuroscience* **27,** 9545–59 (2007).

98. Hu, Y. F. *et al.* Epidermal neural crest stem cell (EPI-NCSC)--mediated recovery of sensory function in a mouse model of spinal cord injury. *Stem cell reviews* **6,** 186–98 (2010).

99. Sieber-Blum, M. *et al.* Characterization of epidermal neural crest stem cell (EPI-NCSC) grafts in the lesioned spinal cord. *Molecular and cellular neurosciences* **32,** 67–81 (2006).

100. Fernandes, K. J. L., Toma, J. G. & Miller, F. D. Multipotent skin-derived precursors: adult neural crest-related precursors with therapeutic potential. *Philosophical transactions of the Royal Society of London. Series B, Biological sciences* **363,** 185–98 (2008).

101. Institute for Laboratory Animal Resources. Guide for the Care and Use of Laboratory Animals. *National Academy Press, Washington, DC* (1996).

102. Von Koch, C. S. *et al.* Myelomeningocele: characterization of a surgically induced sheep model and its central nervous system similarities and differences to the human disease. *American journal of obstetrics and gynecology* **193,** 1456–62 (2005).

103. Merianos, D., Heaton, T. & Flake, A. W. In utero hematopoietic stem cell transplantation: progress toward clinical application. *Biology of blood and marrow transplantation : journal of the American Society for Blood and Marrow Transplantation* **14,** 729–40 (2008).

104. Cao, H., Liu, T. & Chew, S. Y. The application of nanofibrous scaffolds in neural tissue engineering. *Advanced drug delivery reviews* **61,** 1055–64 (2009).

105. Watanabe, M. *et al.* A tissue engineering approach for prenatal closure of myelomeningocele with gelatin sponges incorporating basic fibroblast growth factor. *Tissue engineering. Part A* **16,** 1645–55 (2010).

106. Fauza, D. O., Jennings, R. W., Teng, Y. D. & Snyder, E. Y. Neural stem cell delivery to the spinal cord in an ovine model of fetal surgery for spina bifida. *Surgery* **144,** 367–73 (2008).

107. Nijagal, A. *et al.* Maternal T cells limit engraftment after in utero hematopoietic cell transplantation in mice. *The Journal of clinical investigation* **121,** 582–92 (2011).